THE UNIVERSITY OF CHICAGO

MOLECULAR SIMULATIONS OF COMPLEX COACERVATES: INFLUENCE OF CHARGE FRACTION, SEQUENCE, CHAIN STIFFNESS, AND COMPOSITION ON PHASE BEHAVIORS

A DISSERTATION SUBMITTED TO
THE FACULTY OF THE PRITZKER SCHOOL OF MOLECULAR ENGINEERING
IN CANDIDACY FOR THE DEGREE OF
DOCTOR OF PHILOSOPHY

BY
BOYUAN YU

CHICAGO, ILLINOIS
MARCH 2023

To my parents and motherland

To know when you know something, and to know when you don't know, that's knowledge.

-Confucius, *The Analects (Lunyu)*

TABLE OF CONTENTS

LIST OF FIGURES

LIST OF TABLES

ACKNOWLEDGMENTS

Among all the people that have helped and supported me during my Ph.D., I must give my first and greatest thanks to my advisor Professor Juan J. de Pablo. I decided to apply and come to the University of Chicago for my graduate study mainly because I was interested in his research and wanted to join his group. Almost five years passed, and I have never regretted my decision. Juan supports my research, allows me to explore different topics I am interested in, and has taught me how to be a good researcher. He also encourages me always to ask more questions and dig deeper into the fundamentals of the problems. I cannot be what I am now without his advice.

It is also thanks to Juan for building a research group with so many talented people. I have had the privilege to work with some of them, which I appreciated. Among the current and former group members, I am particularly grateful to Prof. Artem M. Rumyantsev, Prof. Nicholas E. Jackson, and Prof. Abelardo Ramirez Hernandez, who are great mentors that guide me along the incredible journey of scientific discovery. I also want to thank Dr. Heyi Liang, Dr. Phillip M. Rauscher, Dr. Ludwig Schneider, and Prof. Elizabeth M.Y. Lee, whom I have been working closely with. I also appreciate the help and support from former group members: Dr. Weiwei Chu, Dr. Jiyuan Li, Dr. Cody Bezik, Dr. Ashley Guo, Dr. Alec Bowen, Dr. Emre Sevgen, Dr. Lucas Antony, and Dr. Daniel Reid, as well as current group members: Viviana Palacio-Betancur, Chuting (Betty) Deng, Chuqiao (Elise) Chen, Yiheng Wu, Ge Sun, Cheng Zhang, Juhae Park, and Yuxin (Sarah) Chen.

I wish to thank Professor Matthew V. Tirrell and Professor Andrew Ferguson for being on my dissertation and candidacy committee and offering me valuable feedback and suggestions. During my graduate study, I am fortunate to participate in several collaborations. I thank my excellent collaborators from other groups and universities: Dr. Siqi Meng, Dr. Jeffrey M. Ting, Prof. Angelika E. Neitzel, Yan Fang, Dr. Hao Wu, Hyun Park, and Ziyi Kou.

This dissertation can only be finished with the support of many excellent administrators

from the University of Chicago, including Heather Crews, Lisa Vonesh, LaKesha Lloyd, Melinda Wesonga, Rovana Popoff, and David Taylor.

I want to give my deep gratitude to my friends and family for their support and accompany during the entire journey. I especially appreciate the invaluable love and belief from my mom and dad, Yinhua Shen and Zhigen Yu. The previous three years have been challenging due to the pandemic and the increasing tension between the United States and China, and I would only go through it with their comfort and weekly video calls. Lastly, I want to give my special thank to Zifan Ye.

ABSTRACT

Complex coacervation occurs between oppositely charged species, resulting in the solute-rich phase (coacervate phase) and solute-lean phase (supernatant phase). Recently, scientists have turned their attention to this phenomenon due to its unique structural and rheological properties. For example, coacervates are promising candidates for many practical applications such as drug delivery and rheology modifiers as well as model systems to understand the liquid-liquid phase separation in biology, which is essential for the formation of membraneless organelles within living cells and prebiotic evolution. However, a deeper understanding of the phase behavior of coacervates, especially how different design parameters influence the properties of the resulting coacervate phase and the role of electrostatic interactions in coacervation, is crucial to use coacervate systems to explain the biological process and synthesize coacervate-based materials for various engineering applications.

This dissertation aims to contribute to the study of coacervation by exploring the effects of charge fraction (f), monomer sequence, chain stiffness, and coacervate composition on the phase behavior of coacervates using coarse-grained simulations. First, the dependence of coacervate phase density on the charge fraction of linear polyelectrolyte (PE) chains is determined by simulations and experiments. Although the scaling dependence obtained from experiments deviates from theory, simulation results indicate the conditions for experiments to reproduce theoretical predictions. Simulation also demonstrates that the salt partitioning between two phases is dependent on the PE chain chemistry, which is in line with experimental results and usually not discussed in theory. Then, we explore the phase behavior of coacervates formed by random statistical copolyelectrolytes whose sequence is determined by the first-order Markov process. Both simulation and theory show that the higher blockiness of PE chains leads to a denser coacervate phase. Beyond theoretical predictions, simulation also reveals a transition for the coacervate phase from a homogeneous state to an inhomogeneous state when the chain blockiness further increases. In addition,

the influence of chain stiffness on coacervation is investigated by modeling the coacervates containing semiflexible chains. Coarse-grained simulations demonstrate the first-order phase transition for the coacervate phase from the isotropic state to the nematic state as the chain stiffness increases. By comparing with the semidilute solution of neutral semiflexible polymers, the role of electrostatics in facilitating the isotropic-to-nematic transition in the coacervate phase is qualitatively discussed. We also show that the chains at the interface between the coacervate and supernatant phases prefer parallel orientation to the interface. Finally, the structural and dynamic properties of hybrid coacervates between linear PEs and oppositely charged spherical particles are obtained by simulations. Simulation results verify the theoretical scaling relationships. Diffusion coefficients of the charged particles are measured for different chain lengths to show the distinct dynamic properties of this hybrid system. For small particles with weak charges, the particle dynamics remain Rouse-like as the PE chains crossover from Rouse to entanglement dynamics. However, as the charges per particle increase, particle dynamics become complicated and exhibit non-Rouse dynamics. To conclude, the implications of this work to the broader community and the future research directions are proposed.

CHAPTER 1

INTRODUCTION

Mixtures of oppositely charged species, such as polyelectrolytes (PEs) and colloids in solution, can undergo phase separation (complex coacervation) into two phases. One is the coacervate phase which is rich in the oppositely charged components, while the other is the supernatant phase which mainly consists of solvent. Recent interest in this phenomenon has been fueled by its close relationship to liquid-liquid phase separation in biology, which is critical to membranless organ formation in living cells. It also has various practical applications in the personal care and food industry. [2] Despite the extensive studies on this topic, questions remain on how the equilibrium and dynamical properties of complex coacervates are determined by a variety of design parameters, for example, charge fraction, monomer sequence, stiffness of PE chains, and compositions of coacervates. Coarse-grained molecular simulations of complex coacervation provide a unique way to understand the phase behavior at the molecular level, help explain experimental observations and theoretical predictions and assist in designing coacervate-based materials with specific properties. In this dissertation, we explore problems related to the design parameters mentioned above and highlight how our findings can be used to tune the properties of complex coacervates. In particular, we emphasize the role of electrostatics in determining phase behavior, which is the key difference between coacervates and semidilute solutions of neutral polymers. We also closely compare the simulation observations and the results from theory to validate the applicability of theoretical predictions to the experimental conditions or even extend it with new findings from simulations.

In Chapter 2, we investigate the phase behavior of complex coacervates formed by oppositely charged PEs across a wide range of charge fraction $f (0.3 \leq f \leq 1.0)$. To quantitatively understand the polymer concentration (C_p) dependence on the charge fraction, homologous (co)polyelectrolytes (coPEs) with a near-ideally random distribution of a charged and neutral

ethylene oxide comonomer were synthesized, and the phase diagrams of resulting coacervates were measured by the thermogravimetric analysis of complex and supernatant phases. The phase diagrams obtained in simulations demonstrate a similar trend as the experiments when tuning the charge fraction. At the intermediate to high f, both simulation and experiment show the same scaling relationship between f and C_p with an exponent deviating from theoretical prediction. For $f < 0.25$, simulation reveals the scaling behavior of f approaches to the theoretical limit, which is evident by the more drastic decrease of C_p at lower f in experiments. In addition, simulation results predict that to recover the theoretical scaling behavior in experiments, PEs with $f < 0.25$ are needed. In this chapter, we also demonstrate the importance of PE chain backbone chemistry on the preferential salt partitioning to either the coacervate or supernatant phase. By changing the polymer-salt interactions in simulation or the polarity and solvation ability of PEs in the experiment, we can alter the salt partitioning between two macrophases in simulation or experiment, respectively. This work is reproduced from my co-authored paper [3] with an emphasis on the Figures as my original work of particular novelty.

In Chapter 3, we study the role of sequence in the complex coacervation of oppositely charged random coPEs, i.e., copolymers comprising cationic/anionic and neutral monomers by combining the coarse-grained simulations and random phase approximation (RPA) theory. Here, the random coPEs represent copolymers synthesized via statistical copolymerization, whose sequence follows a first-order Markov chain process governed by the underlying reactivity ratios. This system can be used as a model to help understand sequence effects in more complex biomacromolecules and provide a simpler way to tune material properties via sequence compared with synthesizing sequence-specific copolymers. It is found that charged monomers enhance the proclivity towards complex coacervation and the coacervates' stability upon adding salt. This result is general and holds for both good and poor solvents, despite the different ("closed" and "open") shapes of the respective coacervation binodal. For high

charge blockiness, simulations reveal the formation of microphase-separated coacervates consisting of domains rich in ionic or neutral monomers. The transition from homogeneous to locally segregated coacervates leads to a non-monotonic dependence of the density on charge blockiness. Our results provide a comprehensive framework to understand and interpret the effects of sequence on complex coacervation and for the rational design of coacervate-based materials. This chapter is reproduced from my paper. [4]

In Chapter 4, we explore the effects of chain stiffness on the phase behavior of complex coacervation involving semiflexible PEs. Compared with charge fraction and charge sequence, the uniqueness of chain stiffness is that it can trigger a secondary phase transition for the coacervate phase from the isotropic state to the nematic state. Theoretical treatments and recent experiments have reported the liquid crystalline order (LCO) emergence for PEs with limited flexibility (such as double-stranded DNA). Understanding this isotropic-to-nematic transition is important to study many biological processes, such as membraneless organelle formation within living cells and prebiotic evolution. In particular, we study the underlying physics of this phenomenon using coarse-grained molecular dynamics simulations of symmetric semiflexible–semiflexible and asymmetric semiflexible–flexible coacervates. By comparing coacervates with the corresponding semidilute solutions of neutral polymers, we demonstrate that Coulomb interactions in coacervates facilitate orientational ordering in agreement with theoretical predictions. Quantitative comparisons between our simulation and theory indicate that, for asymmetric nematic coacervates, the strong orientational ordering of stiff polyanions induces a weak ordering of the flexible polycations — an effect that was not anticipated by available theoretical studies. Simulations reveal that, for nematic coacervates, the preferred orientation of the PE chains at the liquid–liquid coacervate-supernatant interface is parallel, and the alignment of semiflexible PEs is homogeneous. The results presented here provide new molecular-level insights into the intra-coacervate LCO and will help motivate further experimental and theoretical activities in this area. This chapter is reproduced

from my work. [5]

In Chapter 5, we extend the concept of conventional coacervates of oppositely charged PEs to the phase separation between oppositely charged PE and other spherical objects such as colloid particles and globular proteins we call *hybrid* coacervates.[6] Due to the similar driven mechanism, there are many similarities between conventional and hybrid coacervates. However, the compositional changes (introducing different components to the coacervate phase) are shown to greatly alter some physical properties of hybrid coacervates or give them new functionalities compared with conventional coacervates. These hybrid coacervates can also be viewed as models to understand bio-related systems like membraneless organelles, which involves the complexation between globular proteins and other long-chain molecules. Following our initial theoretical efforts, [6], we use coarse-grained simulations to understand further the phase behavior of hybrid coacervates between PE and spherical particles and provide molecular-level information to explain theoretical predictions. Specifically, to study their structural properties, we obtain the scaling dependence of PE layer density on the particle size and number of charges per particle, which agrees with the theory. In addition, we also study how the particle size and number of charges per particle influence the thickness of PE absorption layers. We further analyze the bulk modulus of the coacervate phase as the size and charge per particle change. To explore the dynamic properties, we investigate the diffusion of charged particles complex with different chain lengths of PEs. We demonstrate that when the electrostatic interactions are not too strong, the diffusive behavior of intermediate size particles (diameter smaller than entanglement chain length) remains Rouse-like as the dynamics of PE chains crossover from Rouse dynamics to entanglement dynamics as the chain length increases. [7] The resulting particle diffusion coefficient is independent of polymer chain length at the long-chain limit, which is in line with theoretical assumptions. However, for strong Coulomb interactions, the dynamics of particles become more complicated and cannot be easily explained by current scaling theory. This chapter is reproduced

from my work in preparation. [8]

In Chapter 6, I briefly summarize the significant findings in the previous chapters and how my dissertation work contributes to the development of complex coacervates community. In addition, I also point out several directions worth further exploring based on my current studies, as well as some ideas for future work to inspire newcomers to this area.

CHAPTER 2

INFLUENCE OF CHARGE FRACTION ON THE PHASE BEHAVIOR OF COMPLEX COACERVATES

2.1 Introduction

Mixing of oppositely charged polyelectrolytes (PEs) in solution generally elicits an associative phase separation into a polymer-lean supernatant phase and a polymer-rich polyelectrolyte complex (PEC) phase. [9, 10, 11, 12] This complexation of oppositely charged PEs produces either opaque solids—kinetically trapped glasses—or transparent, viscous liquids—usually closer to or at thermodynamic equilibrium—called polyelectrolyte complex coacervates. [13, 14] In nature, PECs form the constituents of complex multicomponent membraneless organelles in cells, [15, 16] play key roles in post-transcriptional processes,[17] and give rise to functional and responsive materials. [18, 19] PECs are also thought by some to have a role in the origins of life. [20] From a materials' engineering perspective, they are useful candidates for therapeutic protein and nucleotide delivery. [21, 22] Academic interest further encompasses their study in the context of stimuli-responsive hydrogels, [23, 24] enzyme encapsulants, [25, 26] membranes, [27, 28, 29] electrospun fibers, [30, 31] and salt processable materials (saloplastics). [32] Each of these applications is enabled by the specific phase behavior and viscoelastic properties of a PEC under a given set of conditions. Therefore, understanding and controlling PEC phase behavior are key to enabling bottom-up, rational material design.

Properties of PECs are dictated by many factors, including molecular characteristics of the component PEs such as their degree of polymerization (N), [33, 34, 35] charge density or charge fraction (f), [36, 37, 38] blockiness of charges along the chain, [39, 40, 41] polymer hydrophilicity or polarity, [42, 43, 44] tacticity or chirality, [45] and architecture. [46] Effective chemical interaction parameters describing the interplay between all species in the

system (solutes and solvents) have to be considered. This can be achieved by introducing the corresponding Flory–Huggins interaction parameters (χ_{ij}) for PE–PE, PE–solvent, and PE–salt. [42, 43] For the latter case, specific ion effects, which are qualitatively predicted by the Hoffmeister series and ion valency, have to be taken into account. [47] Lastly, environmental conditions such as the solution ionic strength (I), [48] dielectric constant (ϵ), [49] pH, [50] and temperature (T) [51] can enhance or diminish the strength of pertinent non-covalent interactions. In view of this vast parameter space, it is unsurprising that the development of theoretical models capable of capturing all such effects to produce broadly applicable predictions has been challenging.

Although the process of complex coacervation was first described in 1929 by Bungenberg-de Jong and Kruyt, [52] rigorous quantifications of complex and supernatant phase compositions in the construction of binodal phase diagrams have only been reported over the past decade. Given the breadth of works examining PECs, we confine ourselves here to the discussion of a few relevant examples that have probed how PE molecular characteristics impact PEC phase behavior and that have quantified macrophase compositions. In 2010, Spruijt et al. published binodal phase diagrams for PECs of poly(acrylic acid) [PAA] and poly(N,N-dimethylaminoethyl methacrylate) [PDMAEMA] with $N = 20, 50, 150, and 510$. [34] Fluorescein-labeled PAA concentration in the supernatant was measured via fluorescence spectroscopy and subsequently used together with macrophase volume and coacervate dry mass measurements to quantify the amount of water and PAA in each phase. Salt concentrations (C_s) were not directly measured; the authors assumed them to be equal in both phases and additive to yield the concentration of salt at which each sample was prepared ($C_{P,i}$), illustrated by phase diagrams with horizontal tie lines. Li et al. constructed binodal phase diagrams for complexes of poly(L-lysine hydrochloride) (PLK) and poly(sodium D,L-glutamate) (PRE), systematically varying N, initial PE concentration ($C_{P,i}$), and $C_{s,i}$. [35] The authors used a combination of thermogravimetric analysis (TGA), turbidity, and conductivity measure-

ments to measure C_s and PE concentration (C_P) in supernatant and coacervate phases. Salt resistance, a measure of the highest $C_{s,i}$ at a given $C_{P,i}$ where macroscopic phase separation still takes place, was determined by a combination of optical microscopy and turbidity measurements. Collectively, these works demonstrated that (1) longer chains (i.e., higher N) afford denser complexes (i.e., higher C_P) with higher critical salt concentrations ($C_{s,cr}$), (2) coacervates prepared at a higher $C_{P,i}$ exhibit a lower resistance to dissolution with salt ("self-suppression"), and (3) the experimental phase diagrams departed from the Voorn–Overbeek theory [53] in that complexes had higher polymer density than predicted and that salt was observed to partition preferentially into the supernatant phase.

Synthetic PECs studied thus far have predominantly dealt with fully or strongly charged PEs, i.e., those where all or a majority of monomer units are ionized, respectively. [54] For this reason, the role of PE linear charge density or the fraction of ionic monomers f in PE complex coacervation remains almost experimentally unexplored. At the same time, theoretical studies suggest that f can be used to tune the binodals of the associative phase separation as well as the internal structure and density of the PEC phase. [55, 56, 57, 58] A notable exception is a recent experimental investigation of PE charge fraction and polarity effects on PEC phase behavior by the Laaser group. By use of optical turbidity, it was shown that salt resistance decreased with diminishing f (down to $f = 0.67$) but was surprisingly insensitive to comonomer hydrophobicity in that range of charge densities. [59] In addition, the authors reported coacervate compositions measured by TGA for homologous hydrophobic and hydrophilic series ($f = 0.67 - 1.0$) prepared at $0.2M$ potassium chloride (KCl). From these data, the authors concluded that phase behavior was dominated by charge density with the caveat that the hydrophobicity of the chains may have a greater impact at lower f.

The present study is aimed at the systematic comparison of complex coacervation across a broad range of PE linear charge densities combining results from experiments, simulations, and theory. We present binodal phase diagrams for PECs with $f = 0.30 - 1.0$ where amounts

of water, copolyelectrolyte [coPE], and salt in coacervate and supernatant phases were quantified by TGA, as pioneered by Li et al. [35] Similar phase diagrams are also generated from coarse-grained simulations where the simulation results provide molecular level information about the coacervate phase behavior and connect the scaling relationships ($C_P \sim f$) found in experiments with theory. Specifically, simulation results are in good agreement with experiments at intermediate f ranges and approach to the theoretical predictions at lower f values. Simulations also indicate to recover theoretical scaling relationships in experiments, linear PEs with lower f ($0.1 \leq f \leq 0.25$) need to be used. To separate the role of PE charge density from other effects such as hydrophobicity [37, 59] and stiffness, [38] a series of well-defined, homologous coPEs with precisely controlled f values and near ideally random monomer distributions were synthesized. The coPEs are water-soluble across all charge densities, which is in stark contrast to frequently studied hydrophobic PEs that are water-soluble only when a significant fraction of their monomers is ionized. Furthermore, polycation oxidation facilitated a critical analysis of how PE polarity and solvation ability, in addition to f, impacts salt partitioning between macrophases. In addition to the experiments, simulations with different polymer-salt interactions are also conducted to demonstrate that the salt partitioning is influenced by PE chemistry. This provides, to the best of our knowledge, the first quantitative understanding of C_P dependence on f for PECs across a broad range of charge densities.

2.2 Method

2.2.1 Simulation Systems

A Kremer–Grest model [60] including Coulomb interactions between monomers was used to simulate complex coacervation. Specifically, PEs are represented as chains of spherical interaction sites or beads connected by springs, and salt ions are modeled by single

spheres. To reduce computational power, solvent was implicitly included as a continuum medium. All sites were of the same size, $r = \sigma$ (reduced units were used for simulation). A finitely extensible nonlinear elastic (FENE) potential was used for bonded interactions, and excluded volume (non-Coulomb) interactions were modeled by shifted and truncated Lennard-Jones (LJ) potentials. Two scenarios were considered: one in which all sites experience the same LJ interaction potential and another in which salt–monomer interactions differ from (are more attractive than) salt–salt and monomer–monomer interactions. Coulomb interactions between charged sites were calculated by a particle–particle particle-mesh method in LAMMPS. [61] The details of the interaction formulas and parameters can be found in the Section 2.5.1. In this work we use a Θ solvent with $T_\Theta = 3.18$ (i.e., $\epsilon_{LJ} = 0.314 k_B T$) [62] maintained by a Langevin thermostat.

In our simulations, we use a minimal coarse-grain model with an implicit solvent that can capture the main trends in the system's behaviors. A quantitative level of description of the experimental data may be achieved by resorting to more sophisticated simulation approaches. The different polarizabilities of the PEs, the solvent, and the salt ions can all be taken into account via appropriate model parametrization, [63, 64] introducing an additional ion-dipole $\sim 1/r^4$ interaction potential between the beads, [65] and by using polarizable beads comprising Drude oscillators or beads with permanent dipoles. [65, 66] To fully address the microscopic specificity of all species responsible for solvation, hydrogen bonding, chirality effects, and so on, atomistic simulations should be performed. [45, 67]

The charge fraction f is given by the ratio of charged over total number of monomers in the PE chain. For chains of the same f value, previous studies [39, 40, 41] have shown that the sequence of charged and neutral monomers significantly impacts phase behavior in PECs. To take this effect into account and to mimic the statistics of random coPEs, we used two methods of sequence generation that maintain the same f values. Within the first method, we generated ideally random sequences of length $N = 200$ by using a first-

order Markov process, with the eigenvalue of the Markov transition matrix (the measure of charge blockiness) set to $\lambda = 0$.[41, 68] These systems were only used to calculate the dependence of salt-free coacervate density on f and compare it with scaling predictions. [55, 56, 57, 58] The second method was used to properly model poly(AGE-stat-EO)-derived coPEs synthesized by the statistical copolymerization of AGE and EO monomers with 100% conversion. The actual sequences of these coPEs deviate from the ideally random case because of a nonzero correlation parameter, $\lambda \neq 0$, and copolymer compositional drift. [69] To mimic the experimental chains, we generated sequences using the "Compositional Drift" software [70] provided with the known reactivity ratios for AGE and EO monomer and the initial feed ratios (i.e., f values) used in the corresponding experiments. [69] This program uses a Monte Carlo method to generate different realizations of sequences corresponding to the Mayo–Lewis model of copolymerization kinetics. The resulting sequences exhibited minor compositional drift for chains with $N_n = 200$ and Đ= 1.01. These were used for the calculation of binodal curves and for comparison with experiments. As shown below, the results corresponding to these two different ways of generating sequences differ only marginally.

2.2.2 Isothermal–Isobaric (NpT) Ensemble for Salt-Free Coacervates

To simulate the salt-free coacervate phase in the equilibrium state, the simulation box was maintained in an NpT ensemble with $p = 0$ since the osmotic pressure of the polymers in highly diluted supernatant coexisting with the coacervate is close to 0. [57, 7] This NpT ensemble was achieved by coupling a Berendsen barostat and a Langevin thermostat with damping parameter $\Gamma = 1.0m/\tau_{LJ}$, where τ_{LJ} is the reduced time unit and $m = 1$ is the reduced particle mass. The bead velocities and positions were updated by a velocity-Verlet algorithm. The time step was set to be $0.002\tau_{LJ}$. Equilibration was ensured by considering the decay of the end-to-end vector correlation function [57, 7] and the convergence of the

density as a function of time. The average density was obtained after equilibration with a block average.

2.2.3 Gibbs Ensemble Simulation of Phase Coexistence

With the addition of salt ions, binodal curves must be calculated by equilibrating supernatant and coacervate phases. To this end, we used a hybrid MC/MD Gibbs ensemble simulation. [71] A further simplification can be made by assuming there is no polymer in the supernatant phase, which is appropriate unless the critical salt concentration is approached. [72] Experimental binodals obtained in this and earlier studies (26,27) serve to justify this assumption and demonstrate that the density of the supernatant substantially deviates from zero and becomes comparable with that of the coacervate only in a very narrow range of salt concentrations, close to the critical point. Because our simulations are not aimed at describing the solution's critical behavior, the assumption adopted in this work, which strongly simplifies the simulation procedure, is reasonable. For the range of parameters considered here, it leads only to a minor overestimation of the coacervate density, but it does not affect the main findings about the phase behavior such as the shift of the binodals for decreasing f, salt partitioning, scaling for the salt-free coacervate density, and so on.

The coexisting phases are represented by two boxes. One contains salt beads to mimic the supernatant phase, whereas the other corresponds to the coacervate and contains salt and polymers. Phase equilibrium was achieved by randomly choosing one of three events: (i) NVT MD runs within each box for relaxing the system, (ii) particle transfer moves where a pair of oppositely charged salt beads were moved from one box to another, or (iii) volume exchange moves between two boxes. The acceptance criteria for moves ii and iii can be readily derived from the classical NVT Gibbs ensemble method. [73] We implemented this method as Python scripts to drive the simulation in LAMMPS. [74] In this work, the combined volume of the two phases is up to $80000\sigma^3$ to ensure adequate volumes for each

phase and avoid finite-size effects. The total number of coPE chains in the coacervate phase is fixed to 60. The initial configuration of the coacervate phase was generated through a self-avoiding random walk. For the same initial average concentration of polymer and salt, we conducted two independent runs, where the initially assigned volumes for supernatant and coacervate phases were different. Namely, one run had a dense coacervate phase at the beginning while the other started with the polymer-containing phase of large volume and hence low density. These two systems were shown to converge to similar points along the binodal curves, serving to underscore the validity of our procedures.

2.3 Results and Discussion

2.3.1 Experimental Results

Effect of f on Phase Behavior

Phase morphology and salt resistance of PECs prepared from homologous poly(Sulf-stat-EO) and poly(Amox-stat-EO) were first qualitatively examined by bright field optical microscopy (Figure 2.1). The scheme of coPE preparation is shown in Section 2.5.2. More details about experiments including coPE synthesis, PEC preparation, and TGA measurements can be found in our paper [75]. No macroscopic phase separation was observed for complexes of $f = 0.10$. Colloidal coacervate suspensions obtained for $f = 0.30 - 1.0$ were transferred to well plates immediately after preparation and imaged. Formation of liquid complexes was evidenced by spherical droplets observed under the microscope. As expected, complexes of higher charge densities exhibited increased resistance to dissolution with NaCl.

Coacervate Density at $0M$ Exogenous Salt Varies Only Marginally for $f \geq 0.5$

Supernatant and coacervate phases were harvested to determine their water, coPE, and salt weight fractions for samples doped with a range of [NaCl]. As expected, $C_{P,i}$ determined

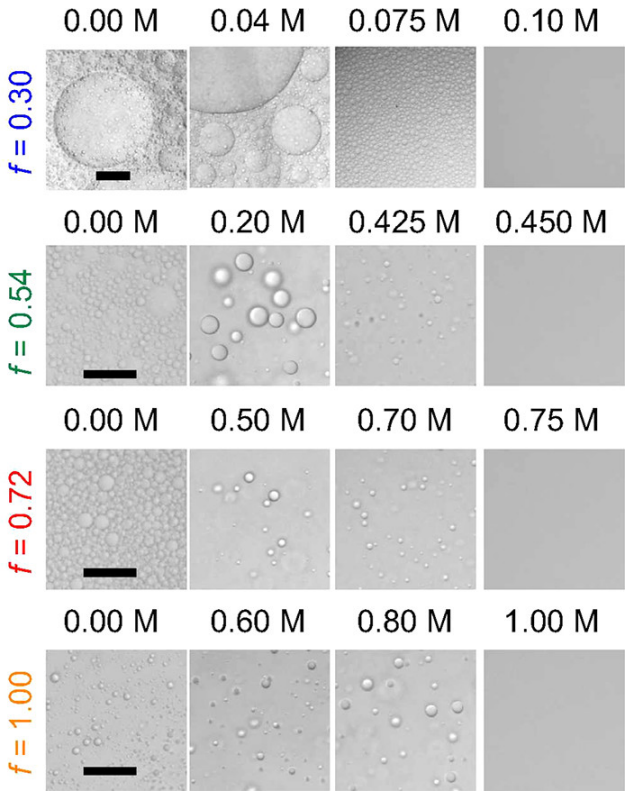

Figure 2.1: Bright field optical microscopy images obtained across indicated charge fractions and sodium chloride salt concentrations. Polymer concentrations were $10mg/mL$ for all f values, and samples were analyzed immediately after complexation. Top row scale bar: $250\mu m$; second to fourth row scale bars: $50\mu m$.

PEC salt resistance but did not impact the ultimate shape of the binodal phase diagram and the PEC critical salt concentration ($C_{s,cr}$). A C_P of $1\,wt\%(= 10mg/mL)$ was chosen as this broadened the range of accessible [NaCl] compared with complexes prepared at higher $C_{P,i}$, thereby simplifying the experimental procedure and reducing error in the analysis. Binodal phase diagrams for PECs with $f = 0.30 - 1.0$ (Figure 2.2) are qualitatively in line with expectations: the two-phase envelope narrows, and $C_{s,cr}$ diminishes with decreasing f. Across the f values presented here, the majority of the coPEs are localized in the complex phase with coPE content in the supernatant phases increasing up to $0.5\,wt\%$ at the highest [NaCl]. Coacervate density in the absence of exogenous salt (not to be confused with coacervates obtained after salt-washing experiments removing endogenous coPE counterions) decreased

only marginally when cutting the PE charge density into half, from $C_P = 38\ wt\ \%$ for $f = 1.0$ to $C_P = 29\ wt\ \%$ for $f = 0.54$. These results indicate a weak dependence of coacervate density on f within a regime of high charge density ($f = 0.54-1.0$). A pronounced decrease in coacervate density is, however, observed for the analogous case of $f = 0.30$, with $C_P = 16\ wt\ \%$, down from $C_P = 29\ wt\ \%$ at $f = 0.54$.

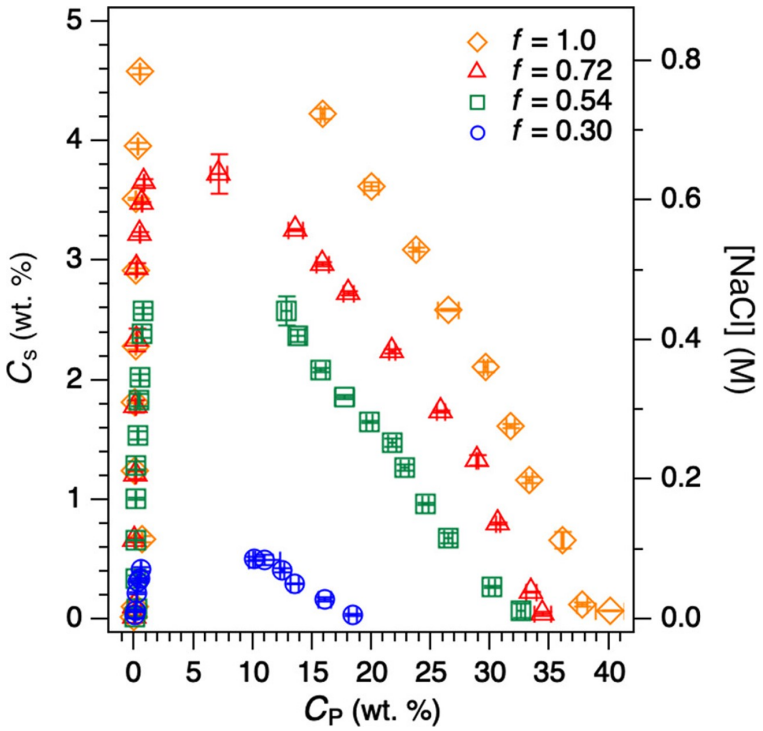

Figure 2.2: Experimental binodal phase diagrams for PECs with $f = 0.30 - 1.0$ and $C_{P,i} = 10mg/mL$ obtained from TGA. The highest C_P values correspond to samples prepared at 0 M exogenous [NaCl] and washed twice with acidified water to reduce coacervate salt content. All measurements were performed in triplicate, and error bars represent the standard deviation between samples.

Effect of f and PE Chemistry on Salt Partitioning

An interesting feature of the PECs described here is the observed salt partitioning between the complex and supernatant phases. Tie lines have been added to the binodal phase diagram for $f = 0.54$ (Figure 2.3A). It can be seen that the tie lines have a positive slope at

low to intermediate exogenous [NaCl] and level off at high [NaCl]. Positive tie line slopes indicate preferential partitioning of NaCl into the coacervate over the supernatant phase. The salt partitioning can be alternatively visualized by plotting a salt partitioning coefficient, the ratio of salt concentration in the coacervate phase (C_s^{coac}) to that in the supernatant phase (C_s^{sup}), against exogenous [NaCl] (Figure 2.3B). Values of $C_s^{coac}/C_s^{sup} > 1$ indicate a preference of NaCl for the coacervate phase whereas $C_s^{coac}/C_s^{sup} < 1$ specifies a preference of NaCl for the supernatant phase. As can be seen in Figure 2.3B, with increasing exogenous [NaCl], C_s^{coac}/C_s^{sup} approaches unity as the coacervate and supernatant phase become less distinguishable.

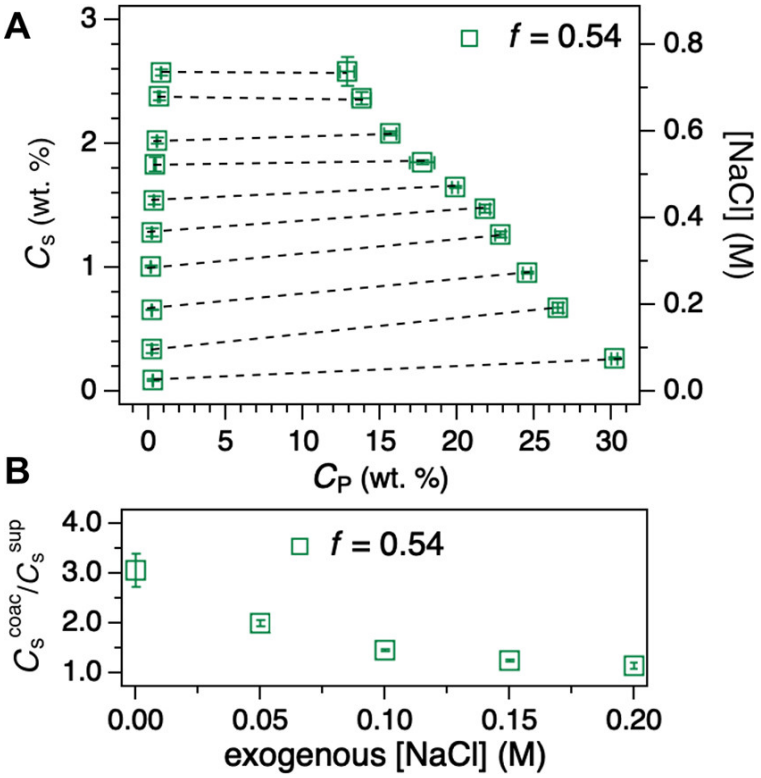

Figure 2.3: Salt partitioning between coacervate and supernatant phases for poly(Amox-stat-EO)/poly(Sulf-stat-EO) with $f = 0.54$. (A) Binodal phase diagram with tie lines. (B) Salt partitioning coefficient (C_s^{coac}/C_s^{sup}) vs exogenous [NaCl]. Error bars indicate the standard deviation between three separate measurements.

Similarly plotting C_s^{coac}/C_s^{sup} vs exogenous [NaCl] for all charge fractions reveals that salt partitions preferentially into the complex phase in all cases at low exogenous [NaCl]

(Figure 2.4A). It appears that the salt partitioning coefficient C_s^{coac}/C_s^{sup} increases with decreasing f, although this trend reverses for $f = 0.30$. Interestingly, we found that polycation oxidation significantly impacts C_s^{coac}/C_s^{sup} (Figure 2.4B). Upon comparison of salt partitioning for poly(Amox)/poly(Sulf) and poly(Am)/poly(Sulf), it can be seen that the relatively more hydrophobic coacervate formed from poly(Am)/poly(Sulf) partitions less salt than its corresponding supernatant phase, whereas the opposite is observed for the more polar poly(Amox)/poly(Sulf).

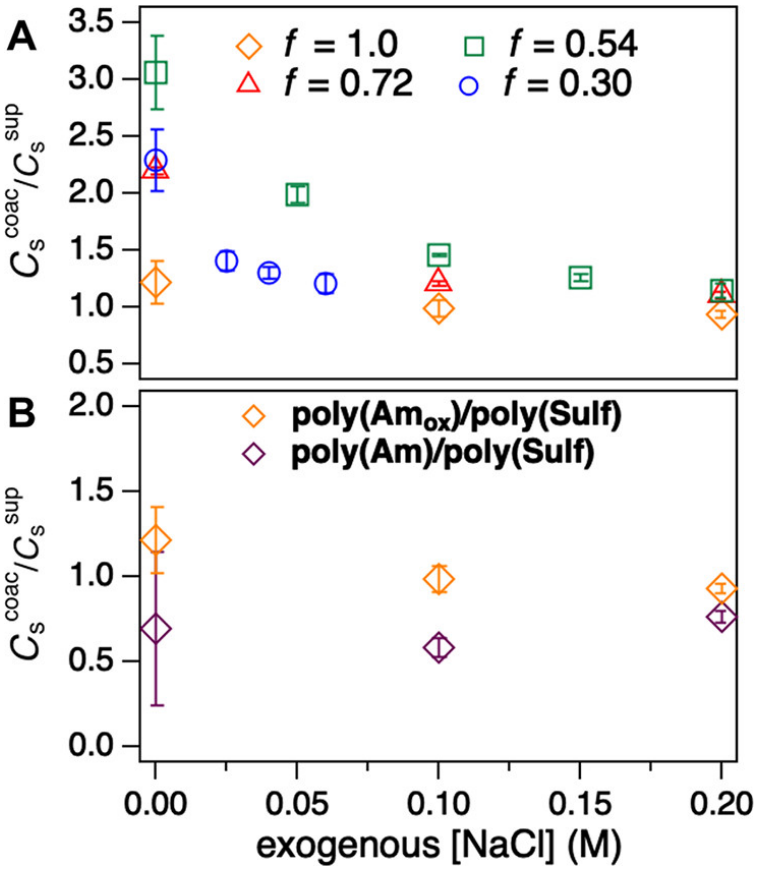

Figure 2.4: Salt partitioning coefficient vs exogenous [NaCl] as a function of (A) charge fraction for the oxidized series and (B) polarity of the polycation. Error bars indicate the standard deviation between three separate measurements.

2.3.2 Simulation Results

Effect of f on Binodal Phase Behavior

As shown by the experimental binodals in Figure 2.2, a majority of coPEs are accumulated in the coacervate phase, serving to validate the assumption of a coPE-free supernatant adopted in simulations. Simulation binodals shown in Figure 2.5 have the same shapes and exhibit the same trends as those measured experimentally. Despite the difference in the interactions between salt ions and monomers, for both cases, the two-phase envelope narrows with increasing salt concentration. The two sets of binodal curves show a reduction of the two-phase region and a decrease of $C_{s,cr}$ with decreasing f, which agrees with experiments and is consistent with physical expectations. For salt-free coacervates, the simulation results also reveal that with decreasing f the density decrease is larger in the range of low f than in the range of high f values: The density drop from $f = 0.54$ to $f = 0.30$ is larger than that from $f = 1.0$ to $f = 0.54$. A detailed analysis of coacervate density dependence on f can be found in the Section 2.3.3 and Figure 2.7B.

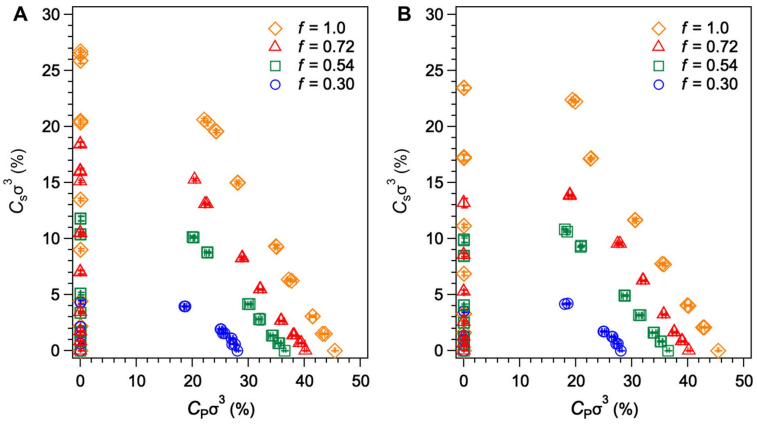

Figure 2.5: Binodal phase diagrams for PECs with $f = 0.30 - 1.0$ obtained from Gibbs ensemble simulation. (A) All beads have same LJ interactions, $\epsilon_{LJ} = 0.314 k_B T$. (B) Salt–salt and monomer–monomer interactions are unchanged, $\epsilon_{LJ} = 0.314 k_B T$, while for salt–monomer interactions $\epsilon_{LJ} = 0.471 k_B T$ to provide stronger attractions between salt and polymer. Error bars indicate the standard deviation from the block average.

Salt Partitioning

Figures 2.5A and 2.5B show simulation binodals for indifferent and more attractive interactions between salt and polymer, respectively. The corresponding salt partitioning coefficients are plotted against the average salt concentration in Figure 2.6. The average salt concentration in simulations was obtained as the ratio between the total number of salt ions in the two phases and the combined volume of the two phases. In Figure 2.6A, all beads experience the same excluded volume interactions, $\epsilon_{LJ} = 0.314 k_B T$, and the salt partitioning coefficients C_s^{coac}/C_s^{sup} are below unity for all f values, indicating that salt ions prefer the supernatant phase. This result is in line with our experimental data for coacervates of poly(Am)/poly(Sulf) where polycations were not oxidized as well as earlier experimental findings for polypeptide PLK/PLE coacervates, [35] simulations, [35, 72] and PRISM theory predictions. [76]

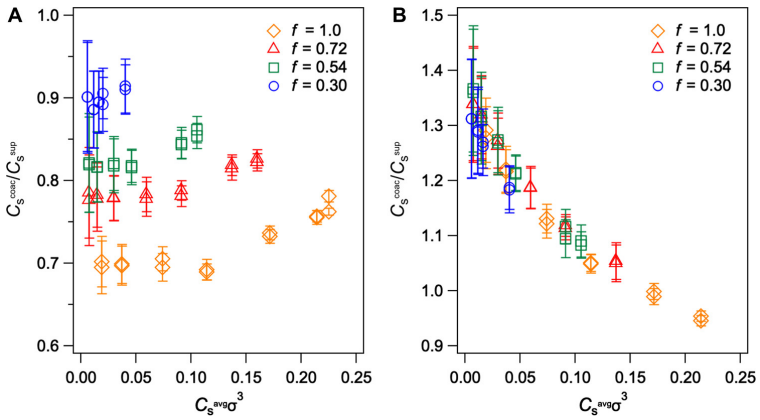

Figure 2.6: Salt partitioning coefficient vs average salt concentration. (A) All beads have the same LJ interactions. (B) Salt–monomer interactions are stronger than salt–salt and monomer–monomer interactions. Error bars indicate the standard deviation.

In addition, the salt partitioning difference between the two phases disappears; that is, C_s^{coac}/C_s^{sup} approaches unity with decreasing f and/or increasing salt concentration as the difference between the two phases diminishes. However, just by modifying the excluded volume interactions between salt ions and polymers to make salt ions more attractive to

polymer beads and setting the corresponding $\epsilon_{LJ} = 0.471 k_B T$, the salt partitioning can be completely changed. As shown in Figure 2.6B, in this case, the salt partition coefficients are above unity for all f values at low salt concentration and monotonically decrease to unity as salt concentration increases. This salt partitioning behavior agrees well with our experimental observations for poly(Amox)/poly(Sulf) solutions (see Figure 2.4A), where salt ions preferentially partition into the coacervate phase. Similar to the former case, the salt partition difference diminishes as salt concentration increases. We note that irrespective of the preferential salt partitioning to the coacervate or the supernatant at low salt concentrations, the salt partitioning coefficient C_s^{coac}/C_s^{sup} always approaches unity (decreasing or increasing, respectively) as salt is added (cf. Figures 2.6A and 2.6B). For increasing concentration of exogenous salt, the coacervate density drops, and the effect of (both Coulomb and non-Coulomb) polymer–salt interactions, which are the driving force for the uneven salt distribution between the coexisting phases, gradually weakens. A similar $C_s^{coac}/C_s^{sup} \leftarrow 1$ behavior in the high-salt regime has been also reported in ref 35.

Our simulations help rationalize the experimental results of Figure 2.5B and reveal that the salt partitioning between coacervate and supernatant phase is nonuniversal but instead depends strongly on the details of polymer chemistry. One can attribute the higher C_s^{coac}/C_s^{sup} for poly(Amox)/poly(Sulf) coacervates as compared to poly(Am)/poly(Sulf) analogues to the better solvation of salt ions, which is itself due to the higher content of polar oxygen atoms (namely, sulfoxide and sulfonium oxygens; see Figure 2.8) in the structure of the oxidized polycations. In simulations, tuning ϵ_{LJ} for polymer–salt interactions takes into account these chemistry-specific effects that are usually neglected in theoretical treatments [76, 77] aimed at describing coacervate/supernatant salt partitioning.

We finally note that the nonmonotonous dependence of C_s^{coac}/C_s^{sup} on f observed in the experiments (see Figure 2.4A) is not reproduced in simulations where the salt partitioning coefficient is found to be almost independent of f, as seen in Figure 2.6B. One of the possible

reasons for this discrepancy is the different solvation of Na+ salt ions by ionic and neutral monomers, which is neglected in simulations where, for simplicity, an identical potential for interactions between salt ions and any monomer units is adopted.

2.3.3 Discussion

Comparison of Theoretical Scaling Laws, MD Simulations, and Experiments

One of the motivations for this work was to access weakly charged PECs and provide a quantitative assessment of analytical scaling laws by comparing to experiments and simulations. [55, 56, 57, 58] Within the weakly charged regime, $f \ll 1$, the density of the salt-free coacervate in a theta solvent is predicted to scale with the charge fraction as

$$\phi = (uf^2)^{1/3} \tag{2.1}$$

where u is the dimensionless Bjerrum length $u = l_B/a = e^2/\epsilon a k_B T$ with a representing the statistical segment length and ϵ representing the dielectric constant of the solvent. For athermal solvent, this law reads $\phi \simeq (uf^2)^{(3\upsilon-1)/(2-\upsilon)} \simeq (uf^2)^{0.54}$, where $\upsilon = 0.588$ has been used. [56, 57, 7, 78] The solvent quality for our chains is not currently known, but small-angle neutron studies are underway which provide insights into the structure of PECs and the chain statistics within electrostatic blobs (i.e., solvent quality). TGA of coacervates prepared at $0M$ exogenous NaCl reveals a weak dependence of coacervate density, or, more accurately, PE weight fraction ($w_{P,c}$) on charge fraction given by $w_{P,c} \sim f^{0.37\pm0.01}$ (Figure 2.7A). Complementary MD simulations for theta solvent conditions yield $\phi \sim f^{0.65\pm0.08}$ for $0.1 \leq f \leq 0.25$ and $\phi \sim f^{0.40\pm0.03}$ for $f \geq 0.25$ (Figure 2.7B). The former result is in good agreement with the scaling prediction of $\phi \sim f^{0.67}$. As anticipated, the latter deviates from scaling analysis due to lower coacervate compressibility at high densities: For theta solvent, scaling takes into account only three-body interactions, [55, 56, 57, 58] whereas higher terms

in the virial expansion become non-negligible at high ϕ. Similar deviations from the scaling predictions to the lower slopes for the $\phi(f^2)$ dependence, 0.41 ± 0.02 vs theoretical 0.54, have been recently reported for athermal solvent. [7]

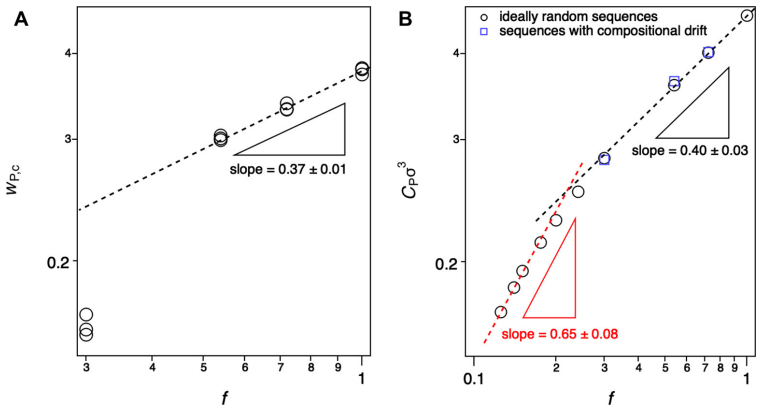

Figure 2.7: (A) Experimental relationship between weight fraction of coPE in the coacervate phase ($w_{P,c}$) at $0M$ exogenous NaCl and f. (B) Coacervate density as a function of f as determined by MD simulations using chains with ideally random sequences or sequences adjusted for compositional drift and Đ(experimental sequences). The slopes reported were obtained by fitting the ideally random sequences in the ranges of $0.125 \leq f \leq 0.20$ and both ideally random and experimental sequences for $0.54 \leq f \leq 1.0$.

The apparent slope of the experimental dependence of coacervate density on f between $0.54 < f < 1.0$ is within error of that calculated in MD simulations. A dramatic decrease in coacervate density is observed between $0.30 < f < 0.54$, but more experimental points corresponding to lower f values are required to facilitate a rigorous comparison with scaling laws. We note that decreasing f would require synthesizing longer copolyelectrolytes. For $N \approx 200$, the lowest content of ionic monomers providing phase separation is $f = 0.30$, whereas at $f = 0.10$ the solution is homogeneous even in the absence of salt. One can estimate which f values become available for longer coPEs using a simple scaling argument: an equal number of electrostatic blobs per polyion should result in similar phase behavior across different f and N values. In theta solvent, each blob consists of $g \simeq (uf^2)^{-2/3}$ monomers [55, 56, 57, 58] and each polyelectrolyte contains $N/g \sim Nf^{4/3}$ electrostatic blobs. Assuming $N_2 = 1000$ and solving $N_1 f_1^{4/3} = N_2 f_2^{4/3}$ with $N_1 = 200$ and $f_1 = 0.30$, one can

conclude that complex coacervation of longer chains is expected for $f \geq f_2 = 0.09$. Similarly, by using $f_1 = 0.10$, one obtains $f_2 = 0.03$. This suggests that for $N_2 = 1000$ coacervation will not take place for $f \leq f_2 = 0.03$. We are currently in the process of preparing chains with $N_2 = 1000$ and $0.10 \leq f \leq 0.25$ to access the range of parameters where scaling laws for coacervate densities can be rigorously and systematically corroborated.

Microscopic Specificity of Interactions

Our data facilitate an evaluation of salt partitioning as a function of f as well as of PE polarity and solvation ability. Experimentally, a preference for salt partitioning into the coacervate phase was observed at lower f values (Figure 2.4A) although that trend appears to reverse for $f = 0.30$. The trend observed between $f = 0.54$ and 1.0 was reproduced in simulation results (Figure 2.6A) and is in line with theory, which reasons that at low PEC density the finite size effect of salt ions is weak and is therefore negligible in the regime of low C_s. [56] The impact of polyelectrolyte polarity and solvation ability on salt partitioning is revealed in Figure 2.4B. Complexes formed from fully charged polyanions and polycations, the latter pre- and postoxidation, demonstrate the importance of the chemistry of the constituent PEs, indicating that salt partitioning is not universal. Simulation results shown in Figure 2.6 corroborate that this effect is attributed to the chemistry-specific interactions between salt ions and polymer. The complexes reported here feature electron-rich ether and sulfoxide/sulfonium oxygens in the polymer structures which are well-hydrated and capable of chelating Lewis acids, such as sodium ions. Hence, we attribute our observations to the combined effects of enhanced PE polarity and solvation ability. Interestingly, the same observation can be made from the data reported by Laaser and co-workers; the coacervates of the hydrophilic (L) series consistently contained a higher concentration of salt than their hydrophobic (B) analogues prepared at a similar charge fraction and identical exogenous [KCl], although this was not directly discussed in the main text (see the authors' Supporting

Information, Table S1). [59] These findings are furthermore in line with previous reports by Schlenoff, [79] Larson, [80] and co-workers.

2.4 Conclusions

The work presented herein aimed to elucidate polyelectrolyte complex coacervate phase behavior across a broad range of charge densities. This was accomplished by employing polyether-based copolyelectrolytes, which remain water-soluble even at low charge fractions, due to the hydrophilic ethylene oxide comonomer. Charged moieties were carefully chosen to obtain equilibrium complexes for salt-free and salted complexes. Hydrophobic interactions were minimized by oxidation of the copolycation side chain thioethers to a mixture of polar sulfoxide and sulfonium species.

The charge density of polyelectrolytes f has been experimentally shown to govern their complex coacervation. The higher the f, the wider the two-phase envelope on the solution phase diagrams. For salt-free solutions, we found only a weak dependence of coacervate density on charge fraction for strongly charged complexes with $f \geq 0.5$ but noted a steep decline in coacervate density below this regime. A quantitative comparison of salt partitioning coefficients as a function of polycation polarity furthermore indicated that polar complexes partitioned salt ions more readily than their hydrophobic analogues. In contrast to most previous studies reporting higher salt concentration in the supernatant than in the coacervate, we observe that the opposite salt partitioning is also possible. This suggests that salt partitioning does not obey a universal rule but crucially depends on the polyelectrolyte chemistry defining their polarity and solvation ability. Our conclusions are supported by coarse-grained computer simulations demonstrating that salt distribution between coacervate and supernatant depends on short-range (non-Coulomb) polymer–salt interactions. In addition, salt partitioning coefficients were found to increase with decreasing charge fraction, albeit this trend appeared to reverse for the lowest charge fraction of $f = 0.30$.

Our findings provide deep insight into the role of polyelectrolyte charge density in complex coacervation, thereby providing valuable guidelines for rational design of coacervate-based materials for practical applications. Further investigations into the phase behavior, structure, and dynamics of very weakly charged chains ($f \leq 0.25$), which will facilitate a quantitative comparison with theoretical scaling laws, [55, 56, 57, 58] are currently underway.

2.5 Supporting Information

2.5.1 Simulation Parameters

The connectivity of copolymer chains is represented by FENE potential between boned beads:

$$U_{FENE} = -0.5KR_0^2 \ln\left[1 - \left(\frac{r}{R_0}\right)^2\right] \tag{2.2}$$

with $K = 30k_BT/\sigma^2$ and $R_0/\sigma = 1.5$ (ϵ and σ are units for energy and length). [60] All beads are interacting though shift and truncated LJ potential:

$$U_{LJ} = \begin{cases} 4\varepsilon\left[\left(\frac{\sigma}{r}\right)^{12} - \left(\frac{\sigma}{r}\right)^{6} - \left(\frac{\sigma}{r_c}\right)^{12} + \left(\frac{\sigma}{r_c}\right)^{6}\right] & \text{for} \quad r \leq r_c \\ 0 & \text{for} \quad r > r_c \end{cases} \tag{2.3}$$

For bonded beads, we use $\epsilon_{LJ} = \epsilon$ and $r_c = 2^{1/6}\sigma$ to balance the FENE potential. For non-bonded beads, we consider two cases. For one case, all beads have the same interactions: $\epsilon_{LJ} = \epsilon$ and $r_c = 2.5\sigma$. For the other case, $r_c = 2.5\sigma, \epsilon_{p-p} = \epsilon_{s-s} = \epsilon$ and $\epsilon_{s-p} = 1.5\epsilon$. Namely, salt ions are more attractive to polymers. For both cases, all beads have the same size σ. The temperature is maintained at Θ solvent condition $T = \epsilon/k_B = T_\Theta = 3.18$. The electrostatic interactions in the system is given by:

$$\frac{U_{coul}}{k_B T} = \frac{z_i z_j l_B}{r} \tag{2.4}$$

where z_i is the valence of charge for i species and $z_i = 1$ or -1. l_B is the Bjerrum length and $l_B = \sigma$ for this work. The Coulomb interaction is solved by Particle-Particle Particle-Meshm method with the error for the long-range force is set to be within 10^{-4}.

2.5.2 coPE synthesis

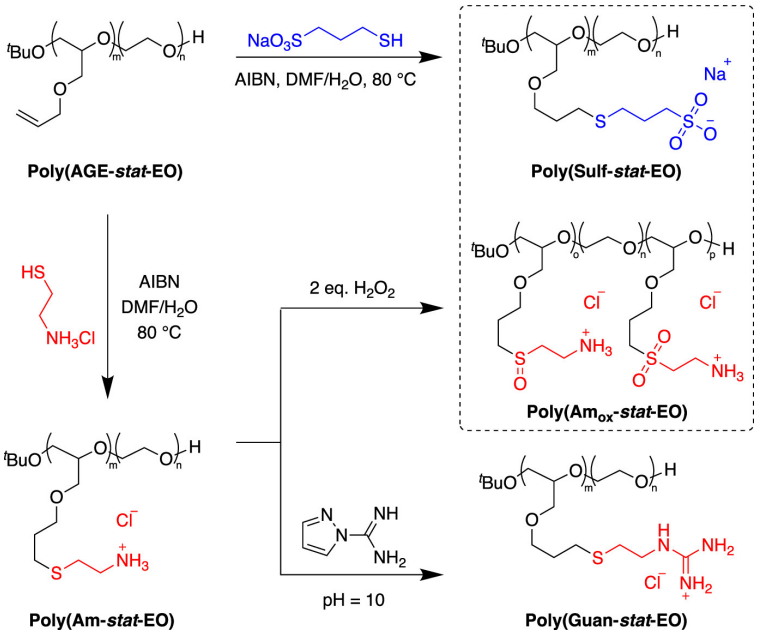

Figure 2.8: Synthesis of Homologous, Statistical Copolyanions and Copolycations with $f = m/(m+n)$ [$m = o + p$ for Oxidized Copolycations and $n = 0$ for Fully Charged Polyelectrolytes]

CHAPTER 3

INFLUENCE OF CHARGE SEQUENCE ON THE PHASE BEHAVIOR OF COMPLEX COACERVATES

3.1 Introduction

Sequence plays a key role in determining the physical properties of synthetic or biological macromolecular materials. [81, 82] In folded proteins, the amino acid residue types (one out of 20) and their linear sequence serve to determine the conformation and functionality of a molecule. In intrinsically disordered proteins (IDPs), a subclass of proteins that lack the ability to form secondary and higher-ordered structures, it is also the sequence of charged monomers that determines the phase behavior in solution [83], and the formation and structure of membraneless organelles. [84, 85] Recent studies with synthetic materials have established that sequence can be utilized to tune the behavior of polymer systems, including single-chain heteropolymers and their microphase-separated melts, or solutions of oppositely charged polyelectrolytes or polyampholytes. [86, 87, 88, 82, 89, 90, 91] The physical principles that encode a particular type of behavior into the sequence of a polyelectrolyte are not fully understood and, when fully unveiled, there should be opportunities to generalize their application for design of broader classes of materials.

In this chapter, we rely on theory and simulations to develop a general framework for design of sequence in oppositely charged polyelectrolytes (PEs). The sequence of charged and neutral monomers in PEs affects the magnitude of charge correlations and the resulting electrostatic attraction between polyanions and polycations. Therefore, the macroscopic phase separation into a polymer-poor supernatant and a polymer-rich PE complex coacervate depends on sequence. This system is analogous to solutions of IDPs (which are biopolyampholytes), where the driving force for the liquid-liquid separation are Coulombic interactions between oppositely charged monomers. For IDPs, phase separation is also referred to as

self-coacervation, because oppositely charged monomers belong to the same chains that constitute the polymer-rich phase. In contrast, PE complex coacervates comprise two types of chains, polyanions and polycations. As discussed here and in the literature, given the similarity in the formation mechanism of complex and self-coacervates, the sequence specificity that is observed in the phase behavior of IDP solutions [85] also arises in PE complex coacervation. [87, 92]

Recent theoretical and simulation studies have considered the similarities between sequence-dependent coacervation in PEs [87, 92] and IDPs. [93, 94, 95, 90, 96] It is worth pointing out that even simple models of IDPs, which represent polyampholytes as chains of identical positively and negatively charged monomers, [93, 94, 95, 90, 96] have been very successful in revealing the role of primary sequence on coacervation. [97, 98] One of the key findings of past work has been that, for a fixed total length and composition of a polyampholyte, increasing the length of the charged blocks of positively and negatively charged monomers leads to a greater propensity for coacervation - an effect that is universal for different types of sequences. [93, 94, 95, 90, 96] Similar conclusions have been drawn in Refs. 87 and 92 for complex coacervation between oppositely charged polypeptides consisting of alternating blocks of neutral and charged monomers. The longer the block length τ, the denser the resulting polyelectrolyte complex coacervate, and the higher its salt resistance. [87] References 87 and 92 are devoted to complex coacervation between sequence-monodisperse polyanions and polycations, and it is of interest to point out the extent to which their conclusions hold for ensembles of PEs having different sequence realizations governed by statistical laws, i.e. for sequence-polydisperse complex coacervation.

In this chapter, we examine sequence-dependent complex coacervation in statistical PEs. We build on a theoretical framework proposed in our earlier work 99, and we use simulations to validate the general predictions of that framework. Statistical PEs, which are also referred to as random correlated copolyelectrolytes (coPEs), can be synthesized via chain copolymer-

izaiton of (i) neutral and charged monomers [100, 101] or (ii) two neutral monomers followed by post-polymerization functionalization to provide ionization of one of them, e.g., using "click" chemistry approaches. [102, 97, 3] Charged and neutral monomers are denoted by $+/-$ and 0, respectively. For low conversion, when compositional drift is negligible, [103, 69] the statistics of these PEs (e.g. polycations) follows a first-order Markov process with a transition matrix given by

$$P_+ = \begin{bmatrix} p_{++} & p_{+0} \\ p_{0+} & p_{00} \end{bmatrix} \tag{3.1}$$

The matrix elements $p_{ij} = p\,(i|j)$ are the conditional probabilities that a monomer of type j is followed by that of type i. The conservation of probability requires that $p_{++} + p_{0+} = 1$ and $p_{+0} + p_{00} = 1$. Owing to the stationary type of the Markov process, the average fraction of ionic monomers in PEs can be expressed as

$$f = p_{++} f + (1 - f) p_{+0} \tag{3.2}$$

The correlation parameter [104, 105, 106]

$$\lambda = p_{++} + p_{00} - 1 \tag{3.3}$$

describes the blockiness of charges and is the eigenvalue of the P_+ matrix. It is convenient to adopt the following representation: [107, 108]

$$P_+ = \begin{bmatrix} 1 - (1 - \lambda)(1 - f) & f(1 - \lambda) \\ (1 - \lambda)(1 - f) & 1 - f(1 - \lambda) \end{bmatrix} \tag{3.4}$$

The values of f and λ are defined by chemistry and by the conditions of the copolymeriza-

tion: [104, 105]

$$f = \frac{r_+ \widetilde{f}^2 + \widetilde{f}(1-\widetilde{f})}{r_+ \widetilde{f}^2 + 2\widetilde{f}(1-\widetilde{f}) + r_0(1-\widetilde{f})^2} \tag{3.5}$$

$$\lambda = \frac{r_+ \widetilde{f}}{r_+ \widetilde{f} + (1-\widetilde{f})} + \frac{r_0(1-\widetilde{f})}{r_0(1-\widetilde{f}) + \widetilde{f}} - 1 \tag{3.6}$$

Here $\widetilde{f}$ is the monomer feed ratio, i.e., the fraction of monomers of the first type in the feed mixture. The reactivity ratios of the monomers, $r_+ = k_{++}/k_{0+}$ and $r_0 = k_{00}/k_{+0}$, are the functions of the reaction rate constants k_{ij} corresponding to the binary chain growth reaction of monomer i joining a polymer with a j end monomer, $...j + i \rightarrow ...ji$.

Equations 3.5 and 3.6 are a reminder that the primary structure of random PEs can be controlled through the synthesis conditions. In what follows, we show how the sequence of monomers translates into the structure and physical properties of the resulting coacervates, thereby establishing a connection between the synthesis and the resulting material properties. As noted earlier, the theoretical framework developed in our earlier work [99] is generalized to sequence- and charge-asymmetric (but homogeneous) coacervates, $f_+ \neq f_-$ and $\lambda_+ \neq \lambda_-$, and validated through coarse-grained Gibbs ensemble simulations. In simulations, special attention is paid to the complexation of PEs with a high degree of charge blockiness, $\lambda_\pm \approx 1$, which may lead to the formation of inhomogeneous coacervates. This effect is also anticipated on the basis of past work that has reported microphase separated structures within the coacervates formed from sequence-monodisperse multiblock PEs with sufficiently long blocks. [109, 110, 111, 112, 113, 114, 115, 116]

This chapter is organized as follows. The theoretical framework and details of our coarse-grained simulations are described in Sections 3.2.1 and 3.2.2. Section 3.3 discusses our results. The first part is focused on the sequence-dependent behavior of homogeneous coacervates, including the effect of the sequence asymmetry between polyanions and polycations ($\lambda_+ \neq \lambda_-$) and the role of the solvent quality. We also outline how experiments could be designed to study the predicted effects. The second part, Section 3.3.2, is devoted to the formation of in-

homogeneous coacervates, and the analysis of their internal microphase separated structure. Section 3.4 provides a summary of our main findings.

3.2 Method

3.2.1 Theoretical Framework

We consider a solution of long flexible oppositely charged PEs containing $N_+ = N_- = N \gg 1$ statistical segments, each of length a. The fraction of charged monomers in the polyanions and polycations is denoted by f_+ and f_-, and their primary sequences are Markov processes with the nontrivial eigenvalues of the transition matrices $P_\pm$ equal to $\lambda_\pm$.

We start with a salt-free solution, and use a random phase approximation formalism (RPA) [117, 118, 119, 120] to find the free energy density of Coulomb correlation attractions between the PEs, $\mathcal{F}_{corr} = F_{corr}a^3/Vk_BT$:

$$\mathcal{F}_{corr} = \frac{1}{2}\int \frac{d^3q}{(2\pi)^3} \ln\left(\frac{\det\left(G^{-1}(q)+U(q)\right)}{\det\left(G^{-1}(q)\right)}\right) - \frac{1}{2}\int \frac{d^3q}{(2\pi)^3} \operatorname{Tr}\left(G(q)U(q)\right) \tag{3.7}$$

Here the components of the $U(q)$ matrix are the Fourier-transforms of the Coulomb interaction potential between the z_i and z_j charges, $U_{ij}(q) = 4\pi u z_i z_j/q^2$, with $u = e^2/\epsilon a k_B T$ being the dimensionless Bjerrum length; $i, j = \pm$ and $z_\pm = \pm 1$ because ionic monomers in PEs carry single charges (if expressed in e units). $G(q)$ is the structure factor matrix of positively and negatively charged monomers, given by

$$G(q) = \begin{pmatrix} \phi_+ g_q^{++} & 0 \\ 0 & \phi_- g_q^{--} \end{pmatrix} \tag{3.8}$$

The volume fractions of polycations and polyanions, ϕ_+ and ϕ_-, can be written as functions of the total polymer volume fraction ϕ, owing to the solution stoichiometry: $\phi_\pm = f_\mp\phi/(f_+ +$

f_-). The structure factors of positively and negatively charged monomers in polycations and polyanions, g_q^{++} and g_q^{--}, can be found in Refs.99, 104, 105, and 121. In the limit of infinitely long chains, $N \to \infty$, they are given by

$$g_q^{++} = \frac{12 f_+^2}{q^2} + f_+ \left(1 - f_+\right) \Lambda_+, \tag{3.9}$$

$$g_q^{--} = \frac{12 f_-^2}{q^2} + f_- \left(1 - f_-\right) \Lambda_-, \tag{3.10}$$

with

$$\Lambda_\pm = \frac{1 + \lambda_\pm}{1 - \lambda_\pm}. \tag{3.11}$$

Omitting the self-energy terms linear in ϕ, which don't contribute to the osmotic pressure [122, 123, 99], one can arrive at a closed-form result for the Coulomb correlation free energy (eq. 3.7) in the salt-free solution

$$\mathcal{F}_{corr} = \frac{1}{12\pi r_{sm}^3} \left(1 - \beta\right) \sqrt{2 + \beta}, \tag{3.12}$$

with a dimensionless parameter $\beta = r_{sm}^2 / r_\lambda^2$. Here the screening radius by the PEs with the homogeneously smeared charge reads

$$r_{sm} = \left(48\pi u f_+ f_- \phi\right)^{-1/4}, \tag{3.13}$$

and that due to charge inhomogeneities along the chain is equal to

$$r_\lambda = \left(4\pi u \frac{f_+ f_-}{f_+ + f_-} \left[\left(1 - f_+\right) \Lambda_+ + \left(1 - f_-\right) \Lambda_-\right] \phi\right)^{-1/2} \tag{3.14}$$

The RPA calculations can be generalized to the salt-added case. If salt ions are considered as point-like charges with zero excluded volume, the free energy density of Coulomb

interactions in the system reads

$$\mathcal{F}_{corr} = \frac{1}{12\pi r_{sm}^3} (1 - \beta - s) \sqrt{2 + \beta + s}, \tag{3.15}$$

with the dimensionless ratio $s = r_{sm}^2 / r_D^2$. The Debye screening radius is given by

$$r_D = (4\pi u c_s)^{-1/2}, \tag{3.16}$$

and $c_s = c_s^+ + c_s^-$ is the total concentration of small anions and cations.

For $\lambda_+ = \lambda_- = -1$ we have PEs with a homogeneous charge distribution, when each monomer carries a charge equal to ef. [99] In this case, Eq. 3.12 reproduces the classic results of Borue and Erukhimovich for the charge-symmetric case, $f_+ = f_-$ [117], as well as those derived by Caltelnovo and Joanny for charge-asymmetric systems, $f_+ \neq f_-$ [118].

For charge-symmetric and sequence-symmetric systems, $f_+ = f_- = f$ and $\lambda_- = \lambda_+ = \lambda$, we obtain Eq. 3.12 with

$$\beta = (1 - f)\Lambda \sqrt{\frac{\pi u \phi}{3}}, \tag{3.17}$$

and $\Lambda = (1 + \lambda)/(1 - \lambda)$, in accordance with Ref. 99. At $f_+ = f_-$ and $\lambda_- \neq \lambda_+$, this result can be still used if Λ is defined by

$$\Lambda = \frac{\Lambda_+ + \Lambda_-}{2} = \frac{1 - \lambda_+ \lambda_-}{(1 - \lambda_+)(1 - \lambda_-)} \tag{3.18}$$

Equation 3.18 shows that the phase behavior of sequence-asymmetric solutions with different λ_+ and λ_- are equivalent provided that value of $\Lambda(\lambda_+, \lambda_-)$ is the same.

Finally, for arbitrary cases of $f_+ \neq f_-$ and $\lambda_+ \neq \lambda_-$, general results given by eqs. 3.13-3.15 should be utilized. We note that our RPA considerations assume ideal-coil statistics of polyanions and polycation within the coacervate that takes place at f_+/f_- ratio being the order of unity. [124] They are also limited to homogeneous coacervates formed from weakly

charged PEs, $f_{\pm} \ll 1$.

To calculate complex coacervation binodals, we write the free energy density of the solution as:

$$\mathcal{F}_{tot} = \mathcal{F}_{corr} + \mathcal{F}_{neut} + \mathcal{F}_{salt} \tag{3.19}$$

The first term, $\mathcal{F}_{corr}$, is the energy of Coulomb interactions between all charged species. It was described above within the RPA. The second term, $\mathcal{F}_{neut}$, is the free energy of the corresponding salt-free solution of neutral polymers, which can be written in the Flory-Huggins form

$$\mathcal{F}_{neut} = \frac{\phi}{N} \ln\left(\frac{\phi}{2}\right) + (1-\phi)\ln(1-\phi) - \chi\phi^2 \tag{3.20}$$

with a χ parameter defining the effective solvent quality for polymers. [125, 126] The last term, $\mathcal{F}_{salt}$, takes into account the ideal-gas translational entropy of point-like salt ions:

$$\mathcal{F}_{salt} = c_s \ln\left(\frac{c_s}{2e}\right) \tag{3.21}$$

The composition of the coexisting coacervate and supernatant phases is defined by the equality of their osmotic pressures and the chemical potentials of the salt ions and polymers; they are given by $\Pi = \mu_s c_s + \mu_p \phi - \mathcal{F}_{tot}$, $\mu_s = d\mathcal{F}_{tot}/dc_s$, and $\mu_p = d\mathcal{F}_{tot}/d\phi$, respectively.

We limit out theoretical calculations to $u = 1$ and low f values, $f = 0.05$ and $f = 0.1$, in order to remain within the rigorous limits of applicability of the RPA framework, $uf^{1/2} \ll 1$. [127, 128] Considering higher f values, $f \approx 1$, does not change the main theoretical findings. [99]

3.2.2 Computer Simulations

The traditional Kremer-Grest model [60] is used to represent random coPEs in implicit solvent. Specifically, PE chains are represented by spherical interaction sites or beads connected by springs. Salt is modeled by individual charged beads. The solvent is included implic-

itly for computational efficiency. As a result, the solvent conditions are controlled by the non-bonded interactions between monomers. In our simulation, we examine two solvent conditions: good (athermal) solvent and poor solvent. The system contains an equal number of polyanions and polycations with chain length $N = 100$. Both polyanions and polycations consist of charged and neutral monomers, and the monomer sequence is assigned by a Markov process based on the Markov transition matrix $P_{\pm}$ for given $\lambda_{\pm}$ and $f_{\pm}$ values. To ensure the electroneutrality of the system, we generate the chains according to the Markov process and retain only those whose fraction of charged monomers is exactly equal to the predetermined $f_{\pm}$. (This restriction does not strongly bias the chain statistics. [106]) The resulting ensemble-average values of the charged block length $\langle N_{charged} \rangle$ and the squared charged block length $\langle {N_{charged}}^2 \rangle$ agree with our theoretical predictions (see Figure 3.10 in Section 3.5).

The connectivity of copolymer chains is maintained by a finitely extensible nonlinear elastic (FENE) potential and Weeks-Chandler-Anderson (WCA) potential between neighboring beads:

$$U_{FENE}+U_{WCA} = \begin{cases} -0.5KR_0^2 \ln\left[1-\left(\frac{r}{R_0}\right)^2\right] + 4\varepsilon\left[\left(\frac{\sigma}{r}\right)^{12} - \left(\frac{\sigma}{r}\right)^{6}\right] + \varepsilon & \text{for} \quad r \le 2^{1/6}\sigma \\ -0.5KR_0^2 \ln\left[1-\left(\frac{r}{R_0}\right)^2\right] & \text{for} \quad r > 2^{1/6}\sigma \end{cases} \tag{3.22}$$

where $K = 30k_BT/\sigma^2$, $R_0 = 1.5\sigma$, and $\varepsilon = k_BT$. [60]

All non-bonded beads interact through a shifted and truncated Lennard-Jones (LJ) potential:

$$U_{LJ} = \begin{cases} 4\varepsilon\left[\left(\frac{\sigma_i}{r}\right)^{12} - \left(\frac{\sigma_i}{r}\right)^{6} - \left(\frac{\sigma_i}{r_c}\right)^{12} + \left(\frac{\sigma_i}{r_c}\right)^{6}\right] & \text{for} \quad r \le r_c \\ 0 & \text{for} \quad r > r_c \end{cases} \tag{3.23}$$

where ε describes the strength of interaction, r_c is the cutoff radius, and σ_i is the bead diameter. Here $i = +$ is positively charged, $-$ is negatively charged, and n is neutral.

To take into account that neutral beads lack hydration shells, the neutral beads in our simulation have a smaller radius than the charged beads. [87] Specifically, $\sigma_+ = \sigma_- = 4\sigma_n = \sigma$, where the mixing rule for LJ potentials between neutral and charged beads is of the Lorentz-Berthelot form. [87] For good solvent conditions, the LJ potential for non-bonded beads is truncated at the minimum $r_c = 2^{1/6}\sigma_i$ $(i = +, -, n)$ with $\varepsilon = k_BT$. Namely, all beads repel each other. For poor solvent conditions, monomer-salt and salt-salt interactions are also truncated at the minimum $r_c = 2^{1/6}\sigma_i$ $(i = +, -)$ with $\varepsilon = k_BT$, while non-bonded monomer-monomer interactions are given by a full LJ potential with $r_c = 2.5\sigma_i$ $(i = +, -, n)$ and $\varepsilon = 0.2k_BT$. Thus, polymer chains can collapse in the absence of Coulomb interactions.

Coulomb interactions between charged beads are given by:

$$\frac{U_{coul}}{k_BT} = \frac{z_i z_j l_B}{r} \tag{3.24}$$

where z_i is the valence of charge for species i $(z_i = \pm 1)$, and $l_B/\sigma = 1.68$ approximately corresponds to a water solvent at room temperature. [87] The long-range Coulomb interaction is calculated via the Particle-Particle Particle-Mesh (PPPM) method in LAMMPS. [61, 129] The targeted error in the long-range forces for the PPPM method is set to 10^{-4}. The velocities and positions of particles are updated using the velocity-Verlet algorithm with a timestep of $0.01\tau_{LJ}$, where $\tau_{LJ} = (m\sigma/k_BT)^{1/2}$ and m is the particle mass.

The number density of polymer beads within the coacervate is denoted by ρ, and that of the salt ions (both anions and cations) is denoted by c_s. To construct the binodal curves, we first simulate the salt-free coacervates where the system is maintained at osmotic pressure $p = 0$ through a Berendsen barostat [124, 7] and constant temperature is maintained by coupling the system to a Langevin heat bath with damping parameter $\Gamma = 1.0m/\tau_{LJ}$. Small and large systems containing 50 and 1900 chains, respectively, are considered. The resulting coacervate densities for small and large systems are very close. Simulations of large systems are performed to calculate the structure factor of the coacervates, $S(q)$, and extend the range

of the available wave vectors to lower q values. Equilibrium is ascertained by monitoring the convergence of coacervate density and the decay of end-to-end vector autocorrelation function as a function of simulation time. [124, 7] The results and uncertainties are measured after equilibrium by a block average analysis. Visualization of simulations is carried out with the OVITO visualisation package. [1]

As salt ions are added, the equilibrium between supernatant and coacervate phases is established by using a hybrid MC/MD Gibbs ensemble simulation [71]. To further simplify the simulation, we assume there is a negligible amount of polymer in the supernatant phase, which is strictly valid when the salt concentration is not too close to the critical salt concentration [72, 34]. To simulate two phases, we use two boxes where one box contains salt beads to represent the supernatant phase and another box that contains polymer and salt beads to represent the coacervate phase. The simulation of the two phases consists of randomly choosing one of three events : (i) an MD run with Langevin thermostat to relax the system; (ii) a volume exchange move between two boxes; (iii) a particle transfer move, where a pair of oppositely charged salt beads is transferred from one box to another. The acceptance criteria for (ii) and (iii) correspond to the traditional NVT Gibbs ensemble simulation method [73]. A more detailed description of this method can be found in Ref 71. The combined volume of the two boxes in the simulation ranges from $54000\sigma^3$ to $120000\sigma^3$, thereby ensuring that each phase has enough volume. The total number of copolymer chains in the coacervate phase is set to 50. The initial polymer configuration is generated by a self-avoiding random walk. For the same initial average polymer and salt concentrations, two independent simulations are conducted with the same combined volume, total number of particles, and same monomer sequence, but different initial box volumes for the supernatant and coacervate phases. One run starts with an initial coacervate density larger than the equilibrium density, while another run starts with initial coacervate density smaller than the equilibrium density. The agreement between the results from these two runs serves to establish the self-consistency of

our Gibbs ensemble simulations.

3.3 Results and Discussion

3.3.1 Homogeneous Coacervate

We first consider the role of primary sequences of charged and neutral monomers on the solution phase behavior. We start with the simplest case, namely that of fully symmetric coacervates. Figure 3.1 shows binodals for a solution of polyanions and polycations with equal average content of ionic monomers, $f_+ = f_-$, and identical charge statistics, $\lambda_+ = \lambda_-$. Theory and simulations demonstrate that the higher the λ value, the wider the region of complex coacervation. Increasing the patchiness of charges results in stronger Coulomb attractions, as seen from our theory, Eqs. 3.12 and 3.15. We attribute this to the stronger charge correlations, i.e., to the higher cooperativity of interactions between opposite charges. The latter causes higher densities of salt-free coacervates and higher salt resistance for increasing λ.

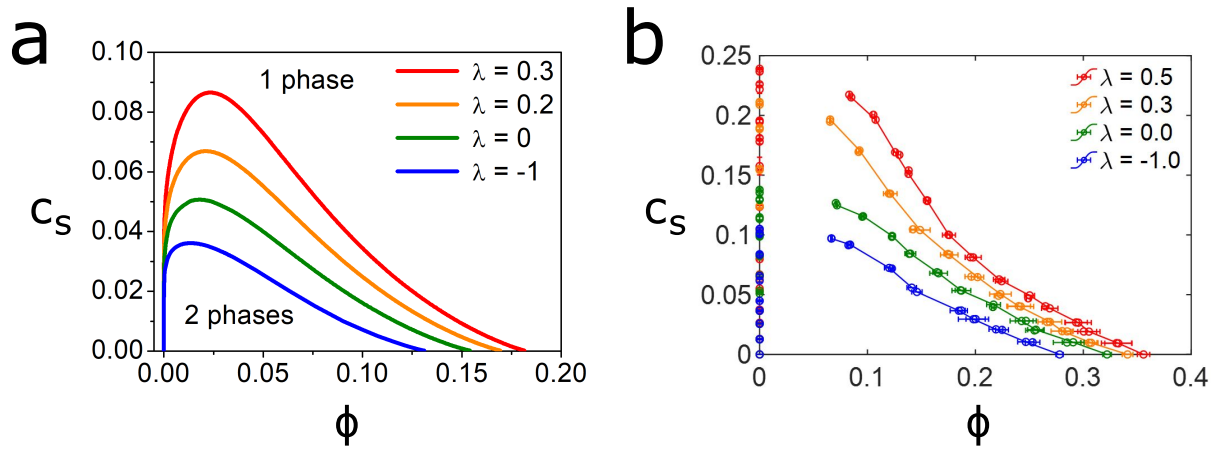

Figure 3.1: Binodal curves for sequence- and charge-density-symmetric PE complex coacervation coacervation, $\lambda_+ = \lambda_- = \lambda$ and $f_+ = f_- = f$. a) Theoretical results for $f_+ = f_- = 0.05$, $N = 10^3$, $u = 1$, and $\chi = 0.5$ (Θ solvent); b) Results from Gibbs ensemble simulations for good solvent and $f_+ = f_- = 0.5$, $N = 10^2$, and $l_B/\sigma = 1.68$.

In contrast to Figure 3.1, which shows the characteristic solution phase behavior of op-

positely charged hydrophilic PEs (i.e., under Θ and good solvent conditions), Figure 3.2 represents coacervation binodals for their hydrophobic counterparts. In poor solvents, complex coacervation cannot be suppressed by the addition of salt because of the short-range of non-electrostatic (hydrophobic) attractions. This "open" shape of the coacervation binodals is anticipated by theory [125], and has been observed experimentally in solutions of synthetic polyelectrolytes with aliphatic backbones, namely poly(acrylic acid) and poly(allylamine hydrochloride). [126] The addition of salt leads to decreasing coacervate density, but not to complete dissolution. At high salt concentrations, when Coulomb interactions are strongly screened by salt, coacervate density ϕ approaches the density ϕ_n of the polymer-rich phase in the corresponding solution of neutral polymers. The values of ϕ_n found theoretically and in simulations are shown in Figure 3.2 with dashed lines.

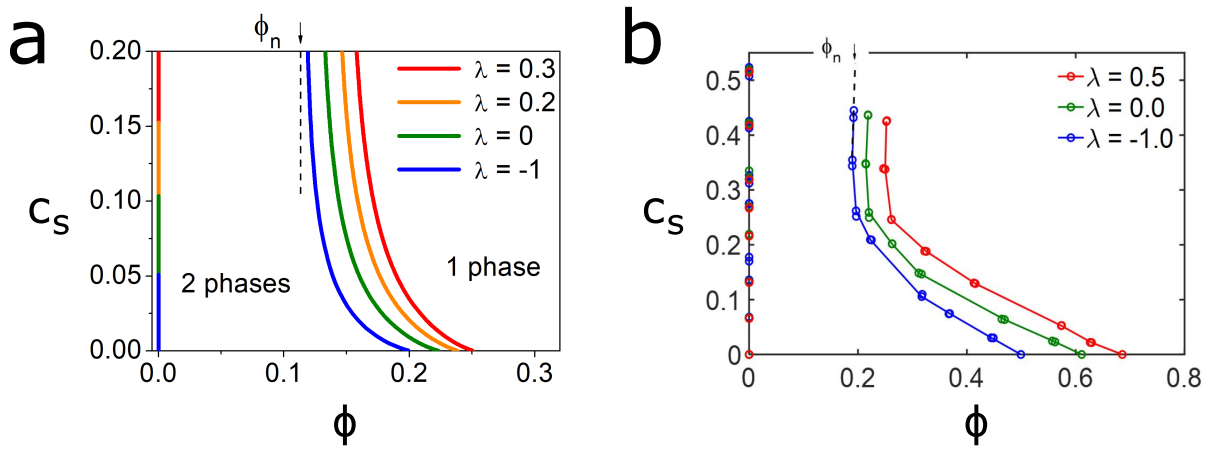

Figure 3.2: Binodal curves for sequence- and charge-density-symmetric PE complex coacervation, $\lambda_+ = \lambda_- = \lambda$ and $f_+ = f_- = f$, in poor solvent. The density of the polymer-rich phase in the solution of neutral polymers under the same solvent quality is denoted by ϕ_n and is shown with black dotted lines. a) Theoretical results for $f = 0.05$, $u = 1$, $N = 10^3$, and $\chi = 0.55$ (poor solvent); b) Results from Gibbs ensemble simulations for $f_+ = f_- = 0.5$, $N = 10^2$, and $l_B/\sigma = 1.68$ (poor solvent).

In the context of the role of sequence, the coacervate branch of the binodals shifts to the right as λ increases. Note that the charge blockiness has a noticeable effect on the coacervate density even at high salt concentrations, despite $\phi \to \phi_n$ for any charge statistics

as c_s increases. This is another manifestation of the stronger charge correlations within the coacervate at high λ. Higher salt concentrations are required to fully screen Coulomb attractions between clusters of opposite charge, which exist at high λ and can be effectively viewed as multivalent ions, as compared to attractions between single charges (univalent ions) that are distributed in an almost equidistant manner along the polyelectrolytes at $\lambda \approx -1$. For high λ values, ϕ approached ϕ_n very slowly because the charge clusters are sufficiently large and their concentration is high as compared to the Θ solvent case due to hydrophobic interactions.

The effects of the charge statistics observed for sequence symmetric coacervates, $\lambda_+ = \lambda_- = \lambda$, is evident because the charge clustering increases simultaneously in polyanions and polycations as λ increases. The more interesting case of sequence-asymmetric coacervates is shown in Figure 3.3. Here the sum $\lambda_+ + \lambda_- = p_{++} + p_{00} + p_{--} + p_{00} - 2$ is fixed (to 0.6), and an increase in λ_+ is accompanied by a concomitant decrease in λ_-. Both theoretical and simulation binodals demonstrate that a high sequence asymmetry facilitates associative phase separation. This result is rationalized by Eq. 3.18, which defines the effective measure of the charge blockiness Λ in sequence asymmetric (and charge symmetric, $f_+ = f_-$) coacervates with unequal λ_+ and λ_-. Equation 3.18 suggests that the sequence-asymmetric coacervate remains stable in the same region as its sequence-symmetric counterpart with the effective λ_{eff} given by

$$\lambda_{eff} = \frac{\lambda_+ + \lambda_- - 2\lambda_+\lambda_-}{2 - \lambda_+ - \lambda_-} \tag{3.25}$$

At a fixed sum $\lambda_+ + \lambda_-$, the value of $\lambda_+\lambda_-$ is the highest, and hence λ_{eff} is the lowest for the sequence-symmetric system with $\lambda_+ = \lambda_-$; these binodals are shown with purple curves in Figure 3.3. As the sequence asymmetry given by $\lambda_+ - \lambda_-$ increases, the two-phase envelope shifts to higher c_s values, and the coacervation region broadens.

In experimental studies of complex coacervation for statistical PEs, the simultaneous change of λ_+ and λ_- can be challenging because it requires precise control of the poly-

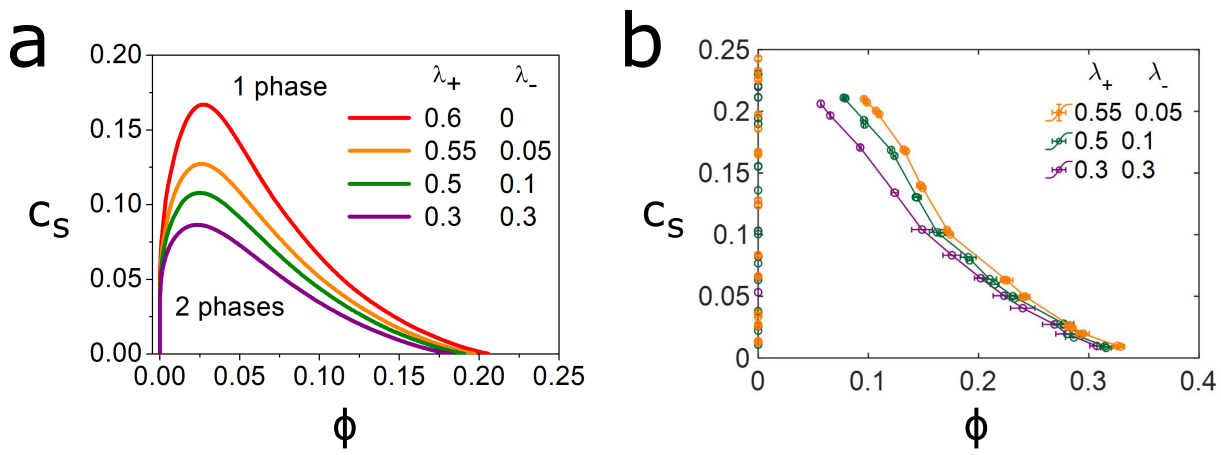

Figure 3.3: Effect of the sequence asymmetry, $\lambda_+ \neq \lambda_-$, on the complex coacervation of charge-density-symmetric PEs, $f_+ = f_- = f$. Coacervation binodals correspond to different $\lambda_\pm$ but the fixed sum $\lambda_+ + \lambda_- = 0.6$. a) Theoretical results for $f = 0.05$, $u = 1$, $N = 10^3$ and $\chi = 0.5$ (Θ solvent); b) Results from Gibbs ensemble simulations for good solvent and $f_+ = f_- = 0.5$, $N = 10^2$, and $l_B/\sigma = 1.68$.

merization process for both polyanions and polycations. From a practical standpoint, the simplest way could be to tune charge statistics in one of the PEs (e.g. polyanion) while keeping the other PE (polycation) unchanged. For instance, the latter can be a homopolycation, while the former can be obtained via statistical copolymerization of neutral and anionic monomers. It is known that the relative reactivity of comonomers can be slightly modified by adjusting the temperature [130] or dielectric constant of the solvent. [131] If copolymerization is conducted in an aqueous medium, the primary sequences of heteropolyanion can be controlled through changing the ionic strength (i.e., the salt concentration) during synthesis. [131] In a salt-free solution, p_{--} can be expected to be low owing to the repulsion of negatively charged end units of the growing chain and the negatively charged monomer. If f_- is close to 1/2, one can expect λ_- values close to -1, and corresponding to almost alternating statistics of charges for copolymerization in salt-free conditions. However, statistical copolymerization in the presence of salt screening Coulomb repulsions between negatively charged monomers should yield statistics of charges that are much closer to ideally random, $\lambda \approx 0$ (assuming neutral and charged monomers have similar chemistry except for the

presence of ionic groups). To achieve even blockier systems, $\lambda > 0$, we hypothesize that further adjustments in solvent quality can be made by adding miscible, monomer-selective cosolvents. Recent experimental works [132] have demonstrated the non-trivial effects that solvent mixtures and salt combinations can have on modulating salt resistance on oppositely charged PE assemblies, so it is reasonable to anticipate that analogous effects can be induced to affect the pairwise reactivity ratios of charged and neutral monomers. This, however, remains an open-ended question that needs to be explored with experimental kinetics and characterization of statistical PEs under different salinity and dielectric constant conditions.

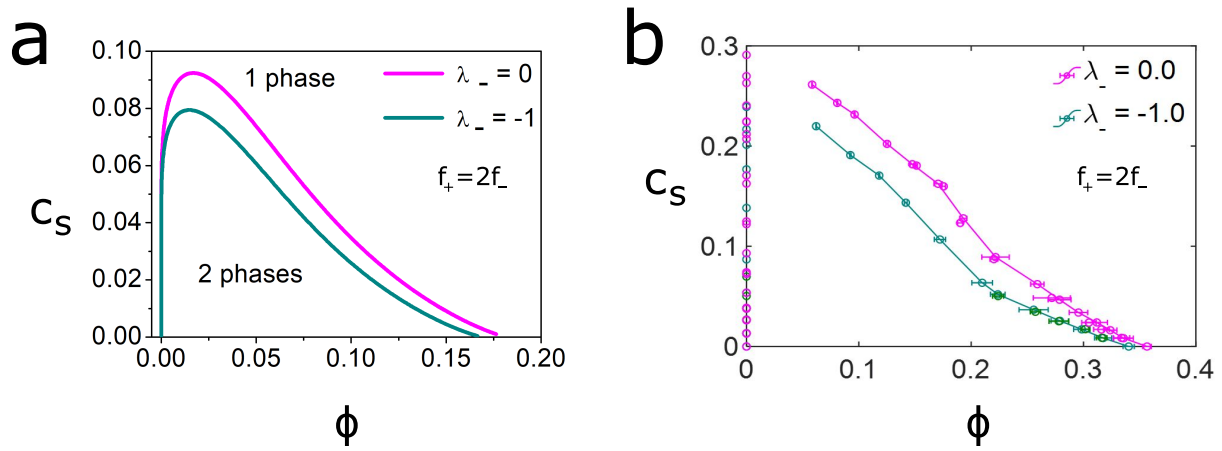

Figure 3.4: Effect of the charge blockiness of polyanions on the complex coacervation of charge-density-asymmertic PEs. a) Theoretical binodals for polyanions of the different charge blockiness, $\lambda_- = -1$ and $\lambda_- = 0$. The values of $u = 1$, $N = 10^3$, $\chi = 0.5$ (Θ solvent), $f_- = 0.05$, $f_+ = 0.1$, and $\lambda_+ = -1$ are fixed; b) Results from Gibbs ensemble simulations for polyanions of different charge blockiness, $\lambda_- = -1$ and $\lambda_- = 0$, under good solvent conditions. The values of $f_+ = 1.0$, $f_- = 0.5$, $N = 10^2$, and $l_B/\sigma = 1.68$ are fixed.

Figure 3.4 shows the shift of the complex coacervation binodals for charge-asymmetric coacervation, $f_+ = 2f_-$, due to the increasing blockiness of the polyanion from $\lambda_- = -1$ to $\lambda_- = 0$ for fixed statistics of the polycations. These results correspond to the experimental system containing homopolycations with $f_+ = 1$ and copolyanions with $f_- = 1/2$ and controlled charge statistics. A noticeable shift of the coacervation binodals makes one consider the possibility of the experimental realization of this system, although the difference between

the binodals in Figure 3.4 is lower than that in Figure 3.1 (blue and green curve, $\lambda = -1$ and $\lambda = 0$), when the blockiness of polyanions and polycations changes simultaneously.

Our preliminary experimental studies indicate that an important challenge is to synthesize heteropolyanions that would not only differ in λ_- values but also have very close compositions f_- and lengths N_-. Since the latter factors strongly affect the position of the binodals, [34, 133, 134, 135, 126, 3] precise control of f_- and N_- values is required to isolate and reveal the role of charge blockiness.

3.3.2 Inhomogeneous Coacervate

The theoretical analysis of Section 3.2.1 suggests that, for sequence- and charge-density-symmetric coacervates, their salt-free densities should increase monotonically with charge patchiness λ. However, the RPA based considerations *a priori* assume a homogeneous coacervate structure that can be violated at very high λ values, when blocks of charged and neutral monomers are sufficiently long. To overcome this theoretical limitation, we use simulations and consider the coacervate properties in the entire range of λ values, including λ very close to 1. The charge fractions are fixed at $f_+ = f_- = 0.5$.

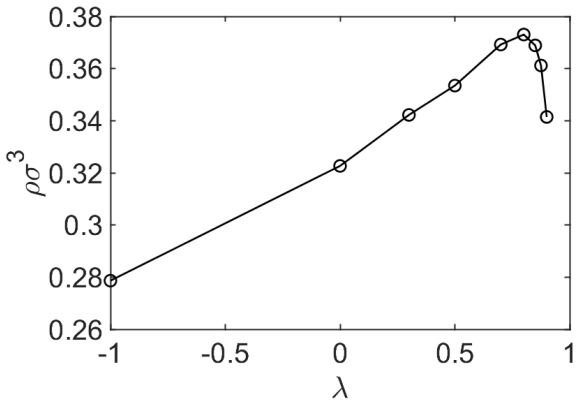

Figure 3.5: Dependence of the salt-free coacervate number density on λ from computer simulations. The parameters are equal to $f_+ = f_- = 0.5$, $N = 10^2$, and $l_B/\sigma = 1.68$; the solvent quality is good for polymer chains.

Figure 3.5 shows that the coacervate density increases with increasing charge blockiness

until $\lambda^* \approx 0.7$ and goes down above this threshold. (Dependencies of the coacervate density on λ for other sizes of the neutral monomer can be found in Section 3.5, Figure 3.12.) Combining this simulation result with the theoretical prediction for the density of homogeneous coacervates, one can conclude that the formation of intra-coacervate inhomogeneities is the reason for the non-monotonous behavior of $\phi(\lambda)$. It can be seen in Figure 3.6 that, as λ increases, local compositional fluctuations within the coacervate become stronger. Above a certain threshold, domains enriched with charged (blue and red) and neutral (white) monomers appear. The longer the neutral/charged blocks in the PEs, the larger the domains.

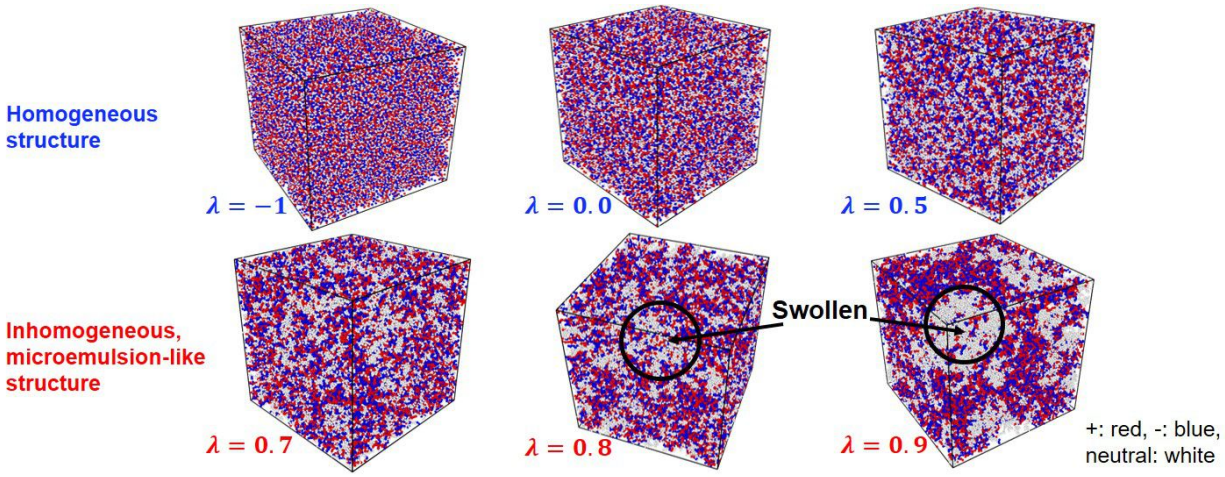

Figure 3.6: Simulation configurations of the coacervate phase for different λ values. Microphase separated, disordered microemulsion-like internal structures appear for large λ when ionic and neutral blocks are sufficiently long to segregate into different domains. The snapshots are generated using the OVITO visualisation package. [1] Red, blue, and white beads represent positively and negatively charged and neutral monomers. Simulation parameters are equal to $f_+ = f_- = 0.5$, $N = 10^2$, $l_B/\sigma = 1.68$, and solvent is good for polymer chains.

Segregation of the coacervate interior into domains enriched with neutral monomers (index "n") and ionic monomers (index "i") is driven by their effective incompatibility. Interactions between neutral and neutral/ionic monomers are purely repulsive, while those between ionic monomers have an additional attractive part due to charge correlations. Each positively charged monomer has more (not belonging to the same chain) neighbors of the opposite charge rather than even charge. Segregation between neutral and ionic monomers

can be considered using the corresponding Flory-Huggins parameter

$$\chi_{ni} \propto E_{ni} - \frac{E_{nn} + E_{ii}}{2} \tag{3.26}$$

with E being the energy of the corresponding pairwise interactions. In dense systems of opposite charges, Coulomb interactions are screened at distances comparable to the monomer size and become effectively short-range. The above qualitative explanation in terms of χ_{ni} therefore becomes applicable. Owing to the negative, correlation-induced attractive contribution to E_{ii}, neutral and ionic monomers are effectively immiscible, $\chi_{ni} > 0$. As high Bjerrum lengths l_B lead to stronger Coulomb attractions, χ_{ni} is an increasing function of l_B. We note that ionic domains are charge-balanced and electroneutral because there is no driving force for local segregation between anionic and cations monomers (in contrast to the microphase separation induced by the incompatibility of polyanions and polycations where neighboring domains carry opposite charge [125, 136, 137, 138, 139]). The growth of the domains is limited by the lengths of the neutral and charged blocks and their connectivity with each other.

The effective FH parameter χ_{ni} introduced above facilitates comparison of our system to a melt of random correlated AB copolymers where both A and B monomers are neutral. In the absence of solvent, our coacervate is similar to a melt of statistical copolymers composed of incompatible A and B monomers with $f_A = f_B = 1/2$. Mean-field theory predicts that, in the limit of long chains $N \to \infty$, the spinodal of the homogeneous state of the melt is given by [104, 105, 140]

$$4 f_A f_B \chi_{AB} \frac{1+\lambda}{1-\lambda} = \chi_{AB}\Lambda = 2 \tag{3.27}$$

and microphase separation is expected above the spinodal. [104, 105] Equation 3.27 demonstrates that the instability of the homogeneous phase can be triggered by either the increasing incompatibility between A and B monomers or the increasing blockiness of like monomers.

The latter is consistent with our observations of intra-coacervate (micro)segregation that happens as λ exceeds the threshold value $\lambda^* \approx 0.7$. However, the presence of a solvent that is non-uniformly distributed within the microstructured coacervate makes the behavior of our system more complicated as compared to that of a random AB-copolymer melt.

One can also see that, for symmetric ideally random copolymers with $\lambda = 0$ and $\Lambda = 1$, the resulting critical value $\chi_{AB} = 2$ coincides with that for the mixture of simple *low-molecular weight* A and B liquids and is N-independent. In other words, much higher incompatibilities are required to induce microphase separation in random copolymers as compared to regular copolymers (e.g. diblock copolymers where $\chi_{AB}^{cr} \propto 1/N$) because any sequence disorder hinders spatial ordering. [141, 142]

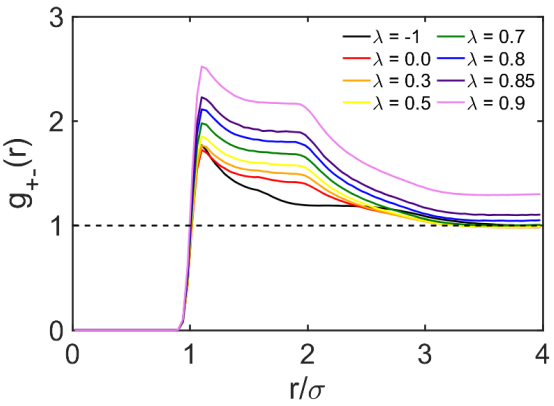

Figure 3.7: Partial radial distribution functions $g_{+-}(r)$ of oppositely charged monomers in salt-free coacervates for different λ values from computer simulations. The simulation parameters are given by $f_+ = f_- = 0.5$, $N = 10^2$, $l_B/\sigma = 1.68$, and solvent is good for polymer chains. The dashed line indicates $g_{+-}(r) = 1$.

The partial radial distribution function (RDF) for oppositely charged monomers $g_{+-}(r)$ shown in Figure 3.7 provides a better understanding of the internal structure of the inhomogeneous coacervate. One can see that $g_{+-}(r)$ increases with increasing sequence correlations, both at $\lambda < \lambda^*$ when the coacervate is homogeneous and at $\lambda > \lambda^*$ when it becomes microphase separated. In the latter case, at $\lambda = 0.85$ and $\lambda = 0.9$, the long tail of the RDF, i.e., $g_{+-}(r)$ values substantially exceeding unity even at $r/\sigma \geq 3$, is indicative of the in-

creasing size of the ionic domains. This effect is also seen in the simulation configuration of Figure 3.6. The values of $g_{+-}(r)$ and hence the density of the ionic domains keep growing even at $\lambda > \lambda^*$, when the average coacervate density decreases. Therefore, microphase separation within the coacervate is accompanied by the simultaneous uptake of solvent from the supernatant and its nonuniform distribution between ionic and neutral domains with a preference for the latter.

To reveal the internal structure of the inhomogeneous coacervate, we calculate the structure factors $S_{tot}(q)$ and $S_m(q)$ corresponding to the total density of all monomers

$$\phi_{tot}(r) = \phi_n(r) + \phi_i(r) \tag{3.28}$$

and to the difference between the densities of neutral and ionic monomers

$$m(r) = \phi_n(r) - \phi_i(r) \tag{3.29}$$

Note that $m(r)$ is used to describe the segregation between the ionic and neutral monomers within the coacervate. It is analogous to the order parameter $m(r) = \phi_A(r) - \phi_B(r)$ defining the local composition and associated with the microphase separation transition (MST) in the melt of random AB copolymers: [105, 108] $m(r)$ is zero in the homogeneous melt and nonzero in the spatially structured state.

Figure 3.8a shows the dependence of the structure factor $S_{tot}(q)$ of all monomers on λ. At $\lambda < \lambda^*$ the structure factor is almost independent of the charge blockiness. Above the threshold λ^* the values of the structure factor in the low q range increase, signalling the strengthening of the large-scale density fluctuations, i.e., the development of the density inhomogeneities as the result of the MST. This upturn suggests an increase in the osmotic compressibility of the coacervate proportional to $S_{tot}(q \to 0)$, and is consistent with the formation of the swollen neutral and dense ionic domains seen in Figure 3.6.

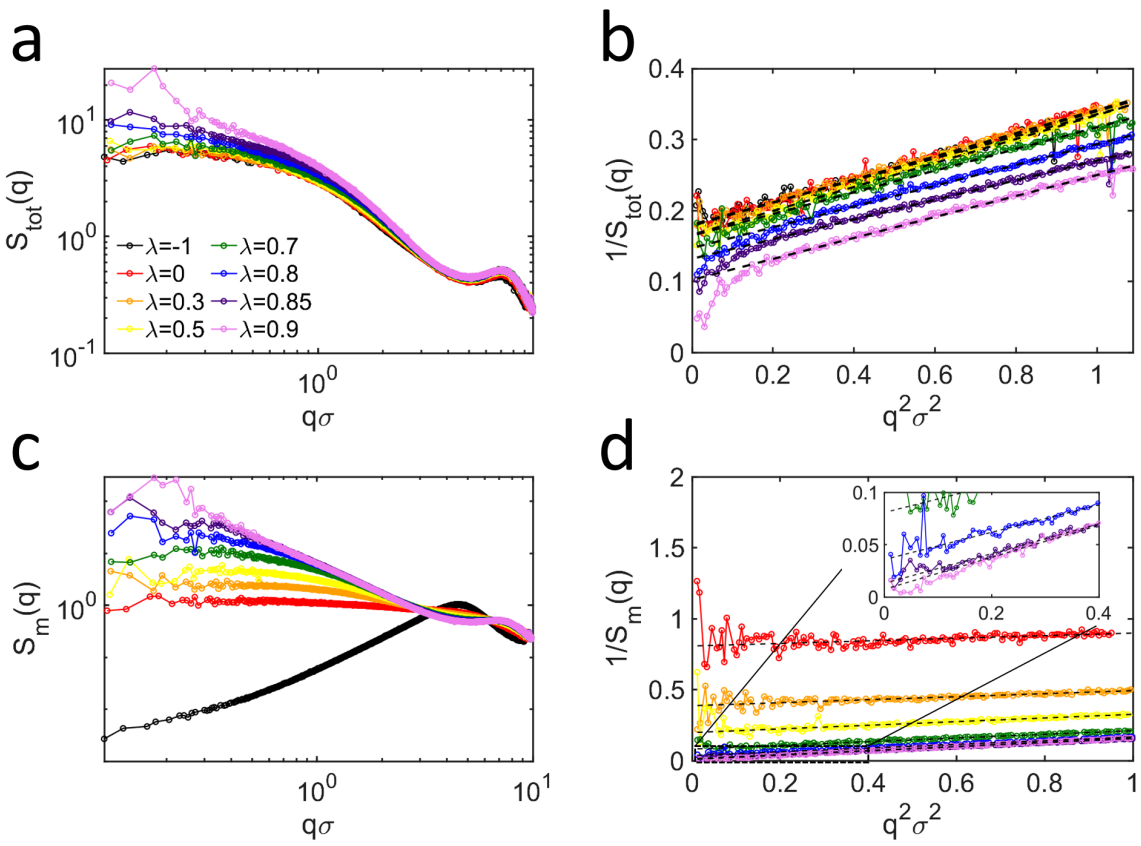

Figure 3.8: Simulation structure factors and their inverse for salt-free coacervates with different λ values. Parameters equal $f_+ = f_- = 0.5$, $N = 10^2$, and $l_B/\sigma = 1.68$; the solvent quality is good. a) Structure factor of all monomers, $S_{tot}(q)$ as a function of q in log-log scale; b) Inverse of the structure factor, $1/S_{tot}(q)$ in a as a function of q^2; c) Structure factor of the density difference between neutral and charged monomers, $S_m(q)$ as a function of q in log-log scale; d) Inverse of the structure factor, $1/S_m(q)$ as a function of q^2. The insert shows a partially enlarged plot of d for the region inside the dash square ($0 < 1/S_m(q) \leq 0.1$ and $0 < q^2\sigma^2 \leq 0.4$). The dashed lines in b and d are fitted by $1/S(q) = c_1 q^2 + c_2$, where c_1, c_2 are fitting parameters.

All structure factors $S_{tot}(q)$ exhibit a peak at $q \approx 2\pi/\sigma$ due to the covalent connectivity of the monomers, while in the range of lower q, their monotonically decreasing behavior can be approximated by the Ornstein-Zernike (OZ) dependence

$$S_{tot}(q) \approx \frac{S_{tot}(q=0)}{1 + (q\xi_{tot})^2} \tag{3.30}$$

This approximation is physically based to the structural similarity between homogeneous coacervates and semidilute solutions of neutral polymers [143, 144, 128, 124] that are well-known to exhibit OZ-type structure factors. [145, 146, 147] Thus, the fit $S(q)_{tot}^{-1} \approx c_1 q^2 + c_2$ is used in order to estimate the correlation length $\xi_{tot} = \sqrt{c_1/c_2}$. One can see in Figure 3.8a that this fit is reasonable not only below but also above the threshold λ^*. At $\lambda > \lambda^*$ the deviation of $S_{tot}(q)$ from the OZ functional form given by Eq. 3.30 is seen in the range of small q only, $q^2 < 0.2$. This mismatch is caused by the MST accompanied by the emergence of the microdomain structure, i.e., large-scale density inhomogeneities. In this case, the resulting value of ξ_{tot} can be considered as the correlation length averaged over all the domains. One can expect that the local correlation length (mesh size) is slightly lower in dense ionic domains and slightly higher in swollen neutral domains.

The red curve in Figure 3.9 demonstrates that the resulting ξ_{tot} obtained from the OZ fit of $S_{tot}(q)$ is almost independent of λ. In the range of $-1 < \lambda < \lambda^*$, this may be attributed to the compensation of the two simultaneous but opposite effects. The increasing coacervate density shown in Figure 3.5 should lead to the decrease in its average mesh size, while the increasing fluctuations in $\phi_{tot}(r)$ seen in Figure 3.6 result in the growth of ξ. At $\lambda > \lambda^*$, when the average density decreases and density fluctuations continue growing, ξ_{tot} slightly increases. We emphasize that both the changes in the coacervate density and ξ_{tot} are moderate in the entire range of blockiness. In this respect, a comparison between the almost unchanged ξ_{tot} and the compositional correlation length ξ_m that strongly increases with λ is insightful, and it is performed in what follows.

The structure factor $S_m(q)$ shown in Figure 3.8c characterizes *compositional* fluctuations and *compositional* inhomogeneities within the coacervate. As compared to $S_{tot}(q)$, $S_m(q)$ grows much stronger in the range of low q at increasing λ, thereby confirming that the segregation between ionic and neutral monomers is the driving force for the MST while moderate undulations of the total polymer density $\phi_{tot}(r)$ is the secondary effect caused

by the preferential partitioning of the solvent to the neutral domains. The compositional difference between neutral and ionic domains is much higher than their density difference.

For coPEs with $\lambda = -1$, the $S_m(q)$ behavior in the high-q range is special. The peak due to monomer connectivity is shifted to approximately $\sqrt{2}$ lower values in comparison with that for more blocky counterparts because the even (ionic or neutral) monomers in alternating chains are separated from each other by two, rather than one covalent bond, and the factor $\sqrt{2}$ (rather than 2) is due to the chain flexibility. Since alternating sequences entirely prohibit the segregation between ionic and neutral monomers at large lengths, $r \gg 2\sigma$, $S_m(q)$ tends to zero at low q more rapidly for $\lambda = -1$.

Figure 3.8c shows that the low-q values of $S_m(q)$ increase at increasing λ, in accordance with the coacervate snapshots shown in Figure 3.6 and demonstrating the increasing heterogeneity above the threshold value λ^* that can be tentatively identified with the MST. One can speculate that, at $\lambda = 0.9$, $S_m(q)$ exhibits a peak, albeit low and wide. The broad shape of the peak and the absence of higher-order reflections (other peaks) imply a lack of long-range order in the domain spacing within the inhomogeneous coacervate (cf. microphase separated, lamellar coacervates for regular copolymers with $S_m(q)$ that demonstrate high and narrow main and satellite peaks, Figure 3.14 in Section 3.5). Thus, on the basis of the $S_m(q)$ shape, one can suggest that the coacervate has a microphase-separated disordered, microemulsion structure. [148, 149, 150, 151, 152] Unfortunately, our simulation data for $\lambda > \lambda^*$ are noisy is the range of low q due to the limited size of the simulation box, and we are unable to see the peaks for other curves, $\lambda = 0.8$ and $\lambda = 0.85$, although they are expected for microemulsions.

These results are also consistent with those observed in simulations [107, 108] of microemulsion-like structures for melts of random AB copolymers. Using the Ginzburg criterion, it has been shown that the fluctuation-dominated region near the MST in these systems is wide [107, 108] and, in contrast to the case of regular copolymers, does not diminish at increasing chain

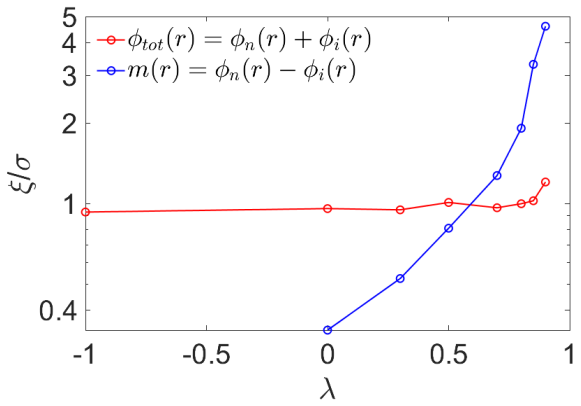

Figure 3.9: Correlation lengths ξ_{tot} (red curve) and ξ_m (blue curve) associated with the fluctuations of the total polymer density $\phi_{tot}(r)$ and the local composition $m(r)$ of the salt-free coacervate, respectively. These results are obtained via fitting the structure factors $S_{tot}(q)$ and $S_m(q)$ found in simulations and shown in Figure 3.8 with the Ornstein-Zernike function: $S^{-1}(q) = c_1 q^2 + c_2$ and $\xi = \sqrt{c_1/c_2}$. ξ_{tot} and ξ_m are plotted in logarithmic scale for better visualization.

length N. In this respect, random copolymers again resemble more low-molecular weight liquids rather than diblock copolymers, see Eq. 3.27. We emphasize that the lack of the domain long-range order in coacervates is due to random, non-regular statistics of n and i monomers in PEs. For regular multiblock PEs composed of alternating charged and neutral blocks of (sufficiently high) average length comparable with Λ, both our simulations (Figures 3.12 and 3.13 in Section 3.5) and SCFT calculations by Sing indicate the lamellar ordering of the domains. [116] This resembles the formation of super-crystalline lattices in melts of regular multiblock copolymers, [153] with AB diblock copolymer melts being the simplest example, and the lack of the translational order in melts of statistical copolymers, [108] at least for equal incompatibilities χ_{AB} and the average block lengths. [142]

An important difference between the coacervates considered here and AB random copolymer melts, however, is that coacervates contain some solvent that redistributes between the domains through the course of microphase separation. The solvent is preferentially absorbed by the domains rich in neutral monomers and can be considered as selective. [154, 155, 156] We believe that the strong swelling of the neutral domains due to the good solvent quality

for polymer chains is the main reason for the decreasing coacervate density at high λ.

To quantitatively confirm the increase in the domain size of the inhomogeneous coacervate at increasing λ, $S_m(q)$ structure factors were also fitted with the OZ function. Another option could have been to fit them with the microemulsion structure factor, $S(q)_m^{-1} \approx c_0 q^4 + c_1 q^2 + c_2$ (see Figure 3.17 and Table 3.1 in Section 3.5), [149] but we neither observe the compositional structure factor decaying according to Porod's law $S_m(q) \propto q^{-4}$ at high q (see Figure 3.18 in Section 3.5) nor do we have accurate data in the vicinity of the peak and for low q values (see Figure 3.8c). The latter should be attributed to the finite size of the box and limited time scales accessible in our simulations.

However, even the ξ_m obtained via a simple OZ fit, shown in Figure 3.9 (blue line), is a monotonically increasing function that rapidly grows in the vicinity of λ^*. $S_m(q)$ for $\lambda = -1$, does not follow the OZ expression because of the reasons discussed above (see also Figure 3.16 in Section 3.5), and the corresponding ξ_m value is not included. At $\lambda > \lambda^*$ the characteristic domain size ξ_m describing the segregation between neutral and ionic monomers is much larger than the coacervate mesh size ξ_{tot}. These results support the idea that the coacervate phase evolves from a homogeneous to inhomogeneous microemulsion state as the charge blockiness λ increases.

Although the considerations presented here were devoted to the case of good solvent, the formation of inhomogeneous coacervates under Θ and poor solvent conditions is also anticipated. The decreasing solvent quality and resulting increasing density of the homogeneous coacervates is expected to lead to a lower threshold blockiness λ^* provoking the MST. However, the density inhomogeneities within the coacervate should be lower because the domains rich in neutral monomers will swell less as than in a good solvent.

3.4 Conclusions

By integrating computer simulations and a theoretical framework based on the random phase approximation (RPA), it has been possible to rationalize the effects of monomer sequence on the phase behavior of complex coacervates formed from random copolyelectrolytes. The monomer sequence of these chains is controlled by a first-order Markov process, and can be experimentally achieved by means of statistical copolymerization. Using molecular dynamics and Gibbs ensemble simulations, we have confirmed our theoretical predictions for the role of charge blockiness in polyelectrolyte complex coacervation. High charge clustering is shown to facilitate coacervation, i.e., to extend the two-phase region of the phase diagram and to improve coacervate salt resistance. The radial distribution functions of oppositely charged monomers within the coacervate are obtained in simulations to demonstrate at the microscopic level that the increasing coacervate density at increasing λ should be attributed to the stronger charge correlations.

While the theoretical framework is (rigorously) applicable to polyelectrolytes carrying small fraction of charged groups only, $f \ll 1$, simulations demonstrate that the principal theoretical findings also hold for the highly charged systems with $f \simeq 1$ that are often studied in experiments. The role of the charge blockiness is shown to be similar for good and poor solvent conditions. The main difference between these cases is that, in a good solvent, coacervate binodals have a “closed" shape, while binodals in poor solvent conditions are “open". These results are consistent with earlier experimental findings.

We also considered the complex coacervation of PEs with equal linear charge densities, $f_+ = f_-$, but unequal charge clustering, $\lambda_+ \neq \lambda_-$. For a fixed sum of the correlation parameters, $\lambda_+ + \lambda_- = const$, the increasing sequence asymmetry, i.e., the increasing difference between λ_- and λ_+, leads to a higher propensity for coacervation. Theory and simulations have been further generalized to charge-density-asymmetric coacervates, $f_+ \neq f_-$, in order

to demonstrate that varying λ for only one of the polyelectrolytes is sufficient to tune the coacervation envelope. This result suggests that the most straightforward experimental way to test our predictions would be to consider coacervation in fully charged homopolycations ($f_+ = 1$) and partially charged copolyanions (e.g., $f_- = 1/2$), with the charge blockiness λ_- controlled through the conditions of the respective statistical copolymerization.

Computer simulations were also aimed at characterizing the complex coacervation of highly blocky copolyelectrolytes with λ close to unity. The theoretical framework proposed here, which predicts a monotonous growth of the coacervate density at increasing λ, can not be applied in this range of parameters because it assumes a homogeneous internal structure of the coacervate. Indeed, simulations reveal that, above a threshold value λ^*, the density of the polymer-rich phase goes down with increasing blockiness. This is due to the formation of inhomogeneous, microphase-separated coacervates that consist of dense domains rich in ionic monomers and more swollen domains rich in neutral monomers. Analysis of the structure factors demonstrates the absence of long-range order within the locally segregated coacervate. Its disordered microemulsion-like structure resembles that of a melt of neutral random AB copolymers.

The results presented here provide a comprehensive computational and theoretical framework to guide molecular design efforts and experiments aimed at tuning the structure and properties of coacervate-based materials through control of monomer sequences. A prospective way to test the effects of charge blockiness in statistical copolyelectrolytes and their complex coacervation has been proposed, along with suggestions to address the expected challenges associated with maintaining the precise lengths N and the average charge density f for a series of polyions with different sequence statistics λ. Given the vast experimental state space of multicomponent statistical copolyelectrolytes, the proposed theory- and simulation-driven predictive capabilities should be of use.

3.5 Supporting Information

3.5.1 Comparison of statistical properties of monomer sequence generated from simulation with theoretical prediction

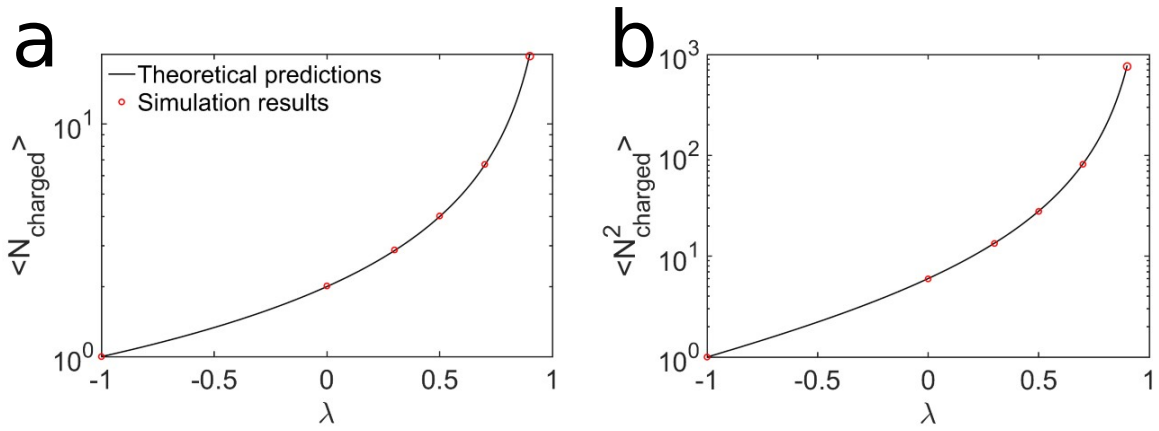

Figure 3.10: Semi-log plot of average charged block length $\langle N_{charged} \rangle$ and average squared charged block length $\left\langle N^2_{charged} \right\rangle$ as a function of λ for charge density $f = 0.5$. Black solid lines are theoretical prediction: $N_{charged} = \frac{1}{(1-\lambda)(1-f)}$ and $N^2_{charged} = \frac{1+f+\lambda(1-f)}{(1-\lambda)^2(1-f)^2}$. Red dots are simulation results. The $\langle ... \rangle$ denotes ensemble average over all chains.

3.5.2 Importance for Experimental Study to Maintain Same Charge Density f for Polyanions with Different λ Values in Order to Verify Computational and Theoretical Results

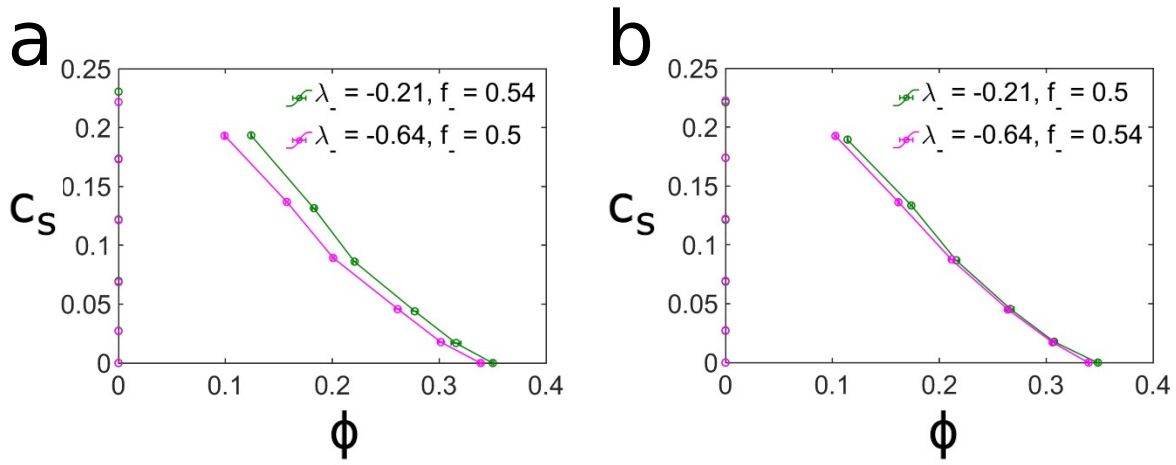

Figure 3.11: Simulation binodal curves for coacervates formed by fully charged polycations ($f_+ = 1$) and polyanions with charge density f_- and sequence λ_-. a: Simulation results for the conditions of our initial experimental attempt. b: Simulation results for the conditions similar to a, but reversing the f_- of the two systems. Comparing a and b shows that besides λ_-, f_- also affects coacervation behavior which needs to be controlled more preciously.

3.5.3 Dependence of Coacervate Density on λ for Different Neutral Monomer Sizes

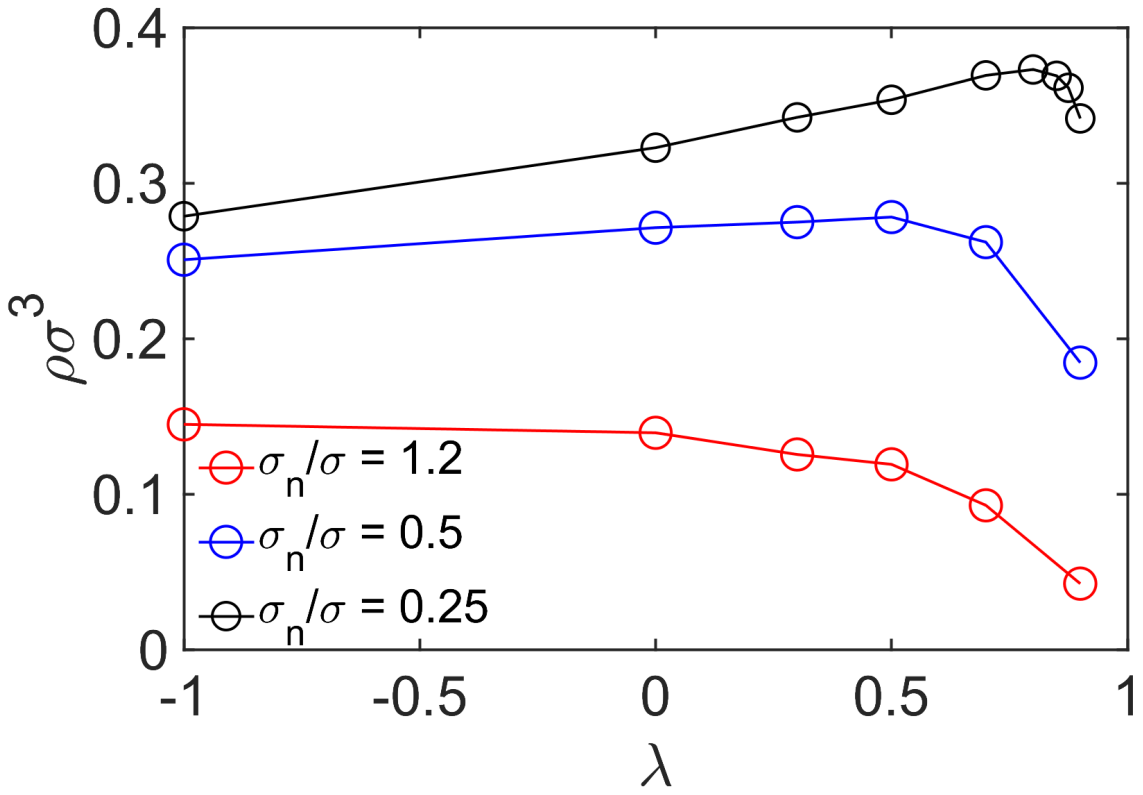

Figure 3.12: Dependence of the coacervate density on λ for different sizes of the neutral monomer, $\sigma_n/\sigma = 1.2$, 0.5, and 0.25. The errors are smaller than the circle symbols. Simulation parameters are equal to $f_+ = f_- = 0.5$, $N = 10^2$, and $l_B/\sigma = 1.68$; the solvent quality is good. Increasing the size of the neutral monomer facilitates microphase separation, and λ^* shifts to lower values.

3.5.4 Simulation Snapshots of Salt-Free Coacervate Phases Formed by Charged Block Copolymers

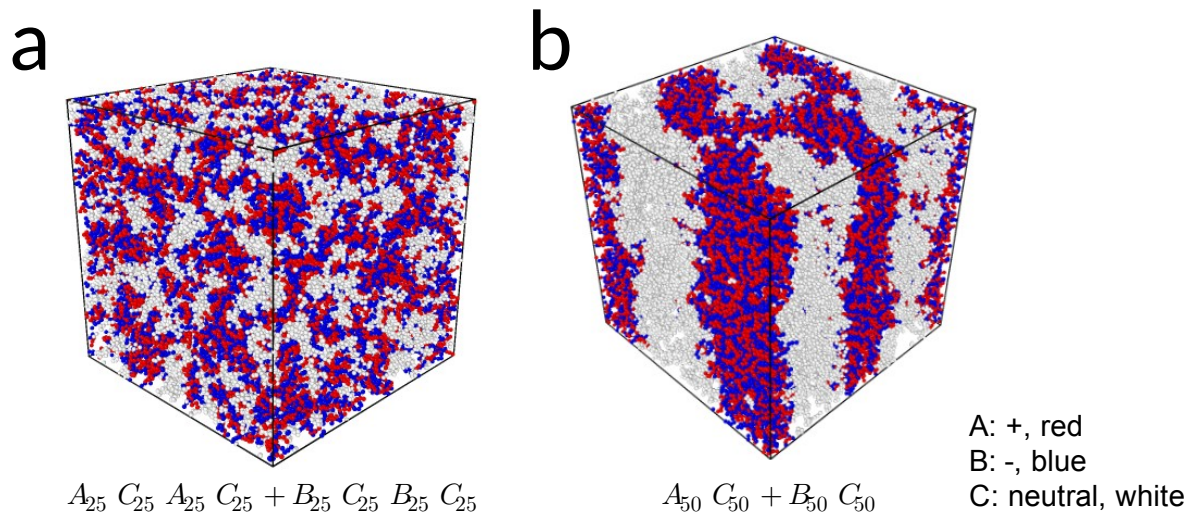

Figure 3.13: Simulation snapshots of salt-free coacervate phases formed by charged block copolymers using the same simulation parameters as statistical polyelectrolytes. Simulation parameters: $f_+ = f_- = 0.5$, $N = 10^2$, and $l_B/\sigma = 1.68$ (good solvent). a: For tetrablock copolymers, the coacervate phase is still microemulsion-like structure with high fluctuation but no obvious long range order. b: For diblock copolymers, there is a lamellar-like structure forming within coacervate phase.

3.5.5 Structure Factors for Lamellar Phase of Salt-Free Complex Coacervate Formed by Charged Diblock Copolyelectrolytes

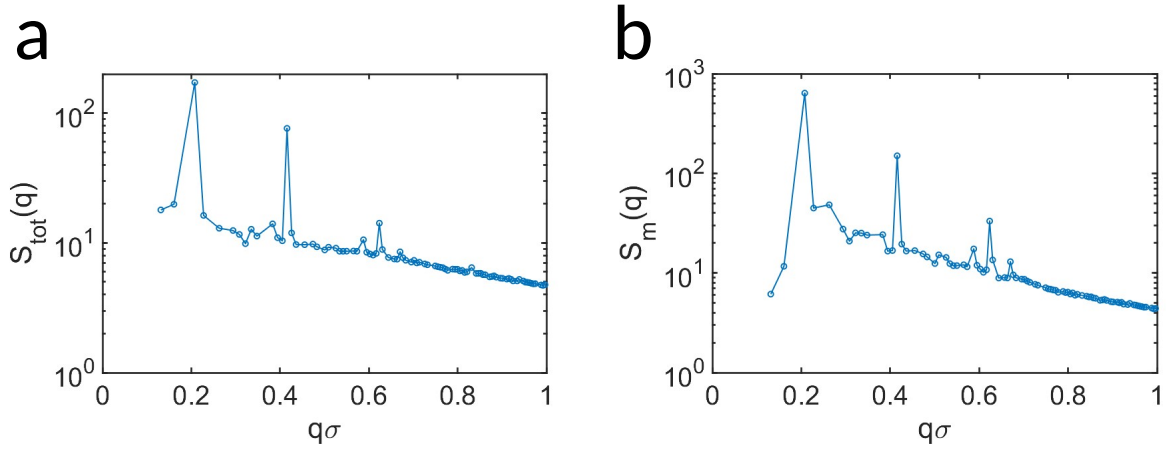

Figure 3.14: Structure factors for salt-free coacervates formed by oppositely charged diblock copolyelectrolytes (shown in Figure 3.6b). a: structure factor for all monomers, $S_{tot}(q)$ as a function of q in log-log scale. b: Structure factor of the density difference between neutral and charged monomers, $S_m(q)$ as a function of q in log-log scale. The peaks in structure factor plots are clear indications of lamellar-like structure within coacervate phase.

3.5.6 Structure Factors for Neutral and Charged Monomers of Salt-Free Coacervate Phases Formed by Polyelectrolytes with Different λ Values

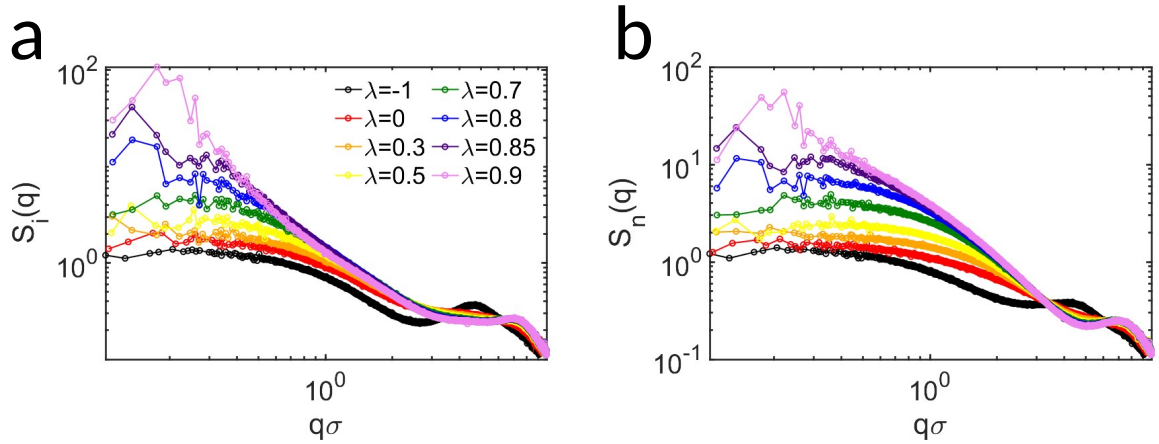

Figure 3.15: Structure factors for neutral and charged monomers within coacervate phases in log-log scale. Simulation parameters: $f_+ = f_- = 0.5$, $N = 10^2$, and $l_B/\sigma = 1.68$ (good solvent). a: Structure factor calculated for only ionic monomers, $S_i(q)$. b: Structure factors calculated for only neutral monomers, $S_n(q)$.

3.5.7 Inverse Structure Factor Calculated Based on Density Difference between Neutral and Charged Monomers for λ Deviates Severely from Ornstein-Zernike Expression

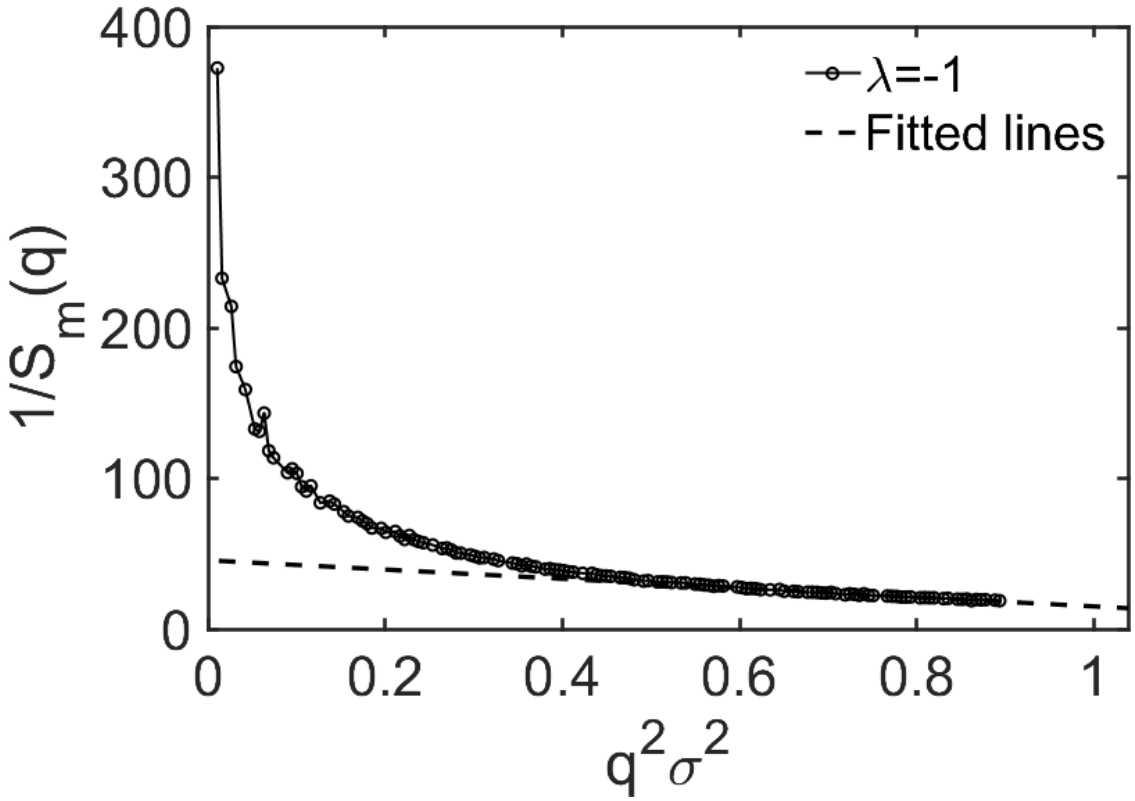

Figure 3.16: Inverse structure factors for $\lambda = -1$ as a function of q^2 fitted by Ornstein-Zernike expression. Simulation parameters: $f_+ = f_- = 0.5$, $N = 10^2$, and $l_B/\sigma = 1.68$ (good solvent).

3.5.8 Inverse Structure Factors Calculated Based on Density Difference between Neutral and Charged Monomers for Different λ Values are Fitted by Microemulsion Structure Factor

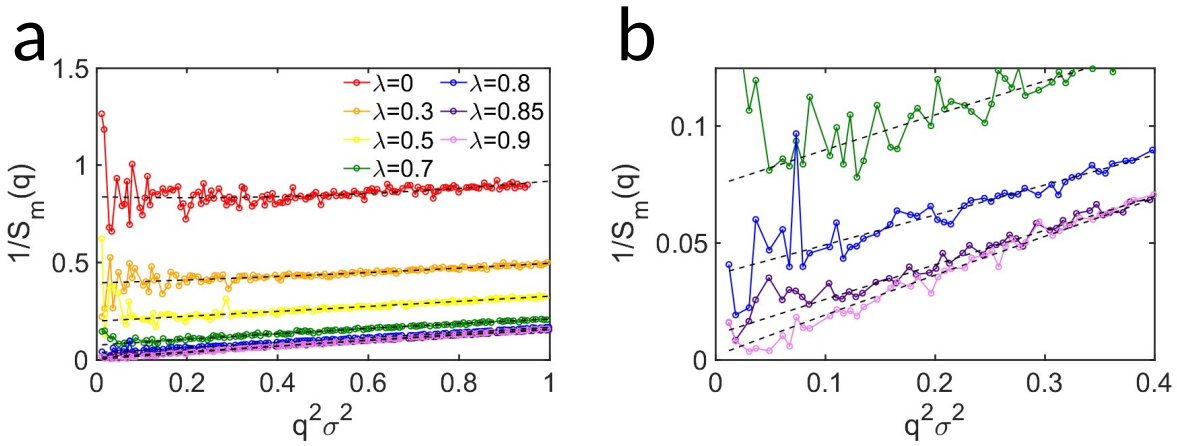

Figure 3.17: Inverse structure factors, $1/S_m(q)$ for different λ values as a function of q^2 fitted by microemulsion structure factor: $1/S(q)_m = c_0q^4 + c_1q^2 + c_2$. Dash lines are fitted lines. a: full plot with $0 < 1/S_m(q) < 1.5$ and $0 < q^2\sigma^2 \leq 1$; b: partially enlarged plot of a with $0 < 1/S_m(q) < 0.125$ and $0 < q^2\sigma^2 \leq 0.4$. Simulation parameters: $f_+ = f_- = 0.5$, $N = 10^2$, and $l_B/\sigma = 1.68$ (good solvent).

λ	c_0	c_1	c_2
0	0.132	-0.051	0.838
0.3	0.030	0.072	0.394
0.5	0.004	0.124	0.198
0.7	-0.022	0.156	0.074
0.8	0.003	0.127	0.036
0.85	-0.008	0.151	0.011
0.9	-0.020	0.176	0.002

Table 3.1: Fitted coefficients of microemulsion structure factor for Figure 3.17.

3.5.9 Inverse Structure Factors Calculated Based on Density Difference between Neutral and Charged Monomers for Different λ Values are Fitted by Porod's law

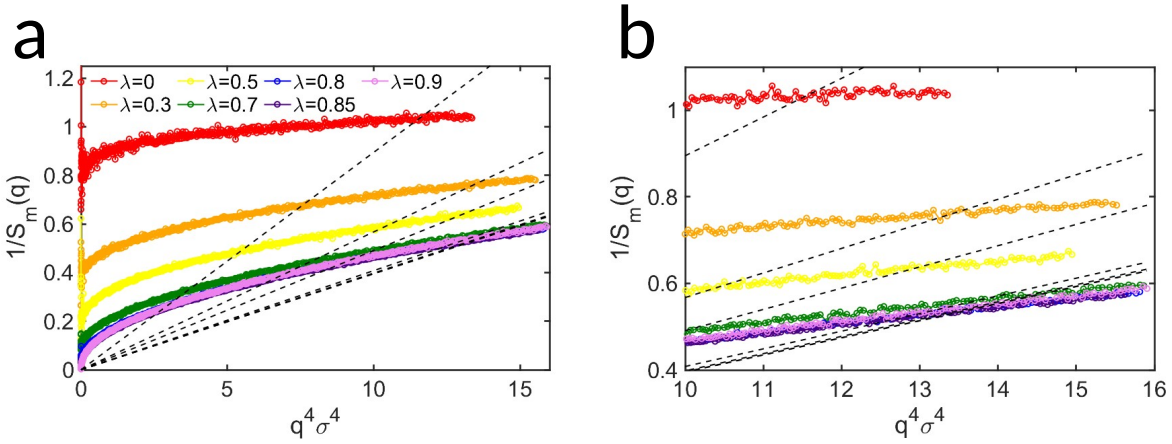

Figure 3.18: Inverse structure factors, $1/S_m(q)$ for different λ values as a function of q^4 fitted by Porod's law: $1/S(q)_m = c_0 q^4$ at high q regime ($10 < q^4\sigma^4 < 16$). Dash lines are fitted lines. a: full plot with $0 < 1/S_m(q) \leq 1.2$ and $0 < q^4\sigma^4 < 16$; b: partially enlarged plot of a with $0.4 \leq 1/S_m(q) \leq 1.2$ and $10 < q^4\sigma^4 < 16$. Simulation parameters: $f_+ = f_- = 0.5$, $N = 10^2$, and $l_B/\sigma = 1.68$ (good solvent).

CHAPTER 4

ISOTROPIC TO NEMATIC TRANSITION INDUCED BY THE CHAIN STIFFNESS IN COMPLEX COACERVATES

4.1 Introduction

Mixtures of oppositely charged polyelectrolytes (PEs) in solution can undergo phase separation into a polymer-rich coacervate phase and a polymer-lean supernatant phase. This phenomenon is partly responsible for the liquid-liquid phase separation (LLPS) of biological macromolecules,[157, 158, 159] which is important for intracellular organization [160, 161, 162] and the formation of membraneless organelles[163, 164, 165, 166] within living cells. Recent studies have also shown that complex coacervation between charged biopolymers such as polypeptides and polynucleotides can be a potential route of prebiotic evolution, since the coacervate droplets provide molecular crowding and compartmentalized environments, which are necessary to achieve high efficiency of the underlying biochemical reactions. [167, 162, 168, 169]

Extensive studies have sought to understand how the equilibrium and rheological properties of complex coacervates can be altered by charge fraction, monomer sequence, added salt concentration, etc. [170, 171, 78, 172, 173, 76, 174, 72, 175, 77, 176, 39, 57, 7, 177, 178, 75] However, the majority of past work has focused on isotropic (and homogeneous rather than microphase separated [179, 180, 116, 4]) coacervate phases. When considering coacervation in the context of bioPEs, an important feature is that polyanions, particularly double-stranded DNA (dsDNA) and/or polycations, have limited flexibility. It is known that semidilute solutions of neutral semiflexible polymers are prone to forming ordered liquid crystalline phases (LCO) even at low polymer concentrations. [181, 182, 183] Phase transitions from disordered (isotropic) to ordered (nematic or smectic) states can be triggered by increasing the polymer concentration and chain stiffness. [181, 184, 185, 186, 187]. It is therefore natural

to expect that orientational order could emerge in coacervates containing semiflexible PEs, since the internal structure of coacervates is similar to that of semidilute solutions of neutral polymers. [56, 57]

Experimental evidence of liquid crystalline order was first reported by Shakya and King, [188] who studied coacervates formed from poly-L-lysine (PLL) and either single-stranded DNA (ssDNA) or dsDNA. It was shown that the secondary phase transition from isotropic to a LC cholesteric state takes place within coacervate droplets when they contain stiff dsDNA, but is absent if stiff DNA duplexes are replaced by flexible ssDNA.

Recently, Jia and Fraccia [167] considered PLL-dsDNA coacervates and reported a phase diagram expressed in terms of salt and polymer concentration. This diagram included regions where an isotropic coacervate is found and other regions with several LC mesophases. The addition of salt was shown to trigger transitions from more ordered states to less ordered LC phases, namely, from a highly-ordered columnar phase C_s to a uniaxial columnar phase C_U, to a twisted nematic (cholesteric) phase N^*. Additional increases in the salt concentration resulted in a transition to the isotropic coacervate phase and, eventually, in the coacervate's dissolution. [167]

Liquid crystalline order in dsDNA was also observed in the cores of polyelectrolyte complex micelles composed of dsDNA and PLL-b-poly(ethylene glycol). [189] In this case, cryo-TEM studies revealed that stiff dsDNA rods are organized in the (uniaxial) columnar phase within the cylindrical micellar cores. Substituting stiff dsDNA with flexible ssDNA resulted in the breakdown of orientational order and in a change of the micellar morphology from wormlike to spherical.

The examples above serve to illustrate that liquid crystallinity in coacervates leads to a rich phase behavior; it is also believed to play an essential role in prebiotic molecular evolution. The higher polymer concentrations encountered in LC coacervates (as compared to their isotropic counterparts) promote selective uptake of biomolecules, and the orientational

order facilitates more rapid and efficient polymerization of nucleic acids (non-enzymatic ligation) and peptides. [167, 190, 191, 192]

Theoretical approaches based on the random phase approximation (RPA) have also been developed to describe the phase behavior of symmetric coacervates formed from the oppositely charged rod-like PEs [193], and that of asymmetric coacervates containing semiflexible polyanions and flexible polycations. [194] In both cases, isotropic-to-nematic (I-N) phase transitions at increasing coacervate densities have been predicted, and electrostatic interactions have been shown to facilitate the emergence of liquid crystalline order. [193, 194] While these past studies provide useful insights into the underlying physics of liquid crystallinity in systems that exhibit long-range Coulomb interactions, they have been limited to weakly charged, infinitely long or perfectly stiff, rod-like PEs. [193, 194]. Molecular simulations provide a useful tool to bridge theoretical and experimental studies, and they can offer additional molecular-level insights into these systems. Additionally, they provide a means to directly corroborate some of the basic theoretical predictions of refs. 193 and 194.

To the our best knowledge, comprehensive simulation studies that address specifically intra-coacervate I-N transitions have not been reported before. The most relevant work on this topic is that of ref. 195, where coarse-grained molecular dynamics (MD) were used to consider the complexation of long flexible polycations with short semiflexible polyanions. That study was focused on the role of chain flexibility on the density of the isotropic coacervate and the salt partitioning between the polymer-rich phase and the supernatant. The formation of nematic coacervates was not considered. Our work is therefore represents a first attempt to provide a molecular-level understanding of orientational order in polyelectrolyte complex coacervates.

A unique feature of LC coacervates is that they represent a special type of LC, which is sensitive not only to temperature and polymer concentration, but also to salt concentration. The addition of salt screens the orientation-dependent Coulomb interactions between the

polyions, and induces a nematic-to-isotropic (N-I) transition, even for a constant mesogen (i.e., polyions) concentration. The sensitivity of LC coacervates to this new stimulus could provide opportunities for design of systems that are responsive to multiple orthogonal stimuli.

In the absence of salt, Coulomb interactions also alter the traditional behaviors observed in polymer liquid crystals. For example, neutral stiff polymers in an athermal solvent only undergo lyotropic phase transitions (Onsager model). In contrast, in PE systems, the presence of Coulomb interactions makes them sensitive to temperature, that is, the LC becomes thermotropic.

In the present study, we consider simple but representative salt-free coacervates and focus on the transition from the isotropic to the nematic state. We perform coarse-grained MD simulations of 1) symmetric semiflexible–semiflexible coacervates and 2) asymmetric semiflexible–flexible coacervates, both in an implicit solvent. The first, symmetric case was theoretically considered in ref. 193; that work, however, dealt with only perfectly rod-like polymers but not semiflexible chains. The asymmetric system was studied theoretically in ref. 194, and can be viewed as a minimal model for coacervates formed from dsDNA and PLL [188] or for other dsDNA-containing coacervate phases.

We aim to consider how increasing the stiffness of semiflexible chains in both systems induces the I-N transition and examine whether the predictions provided by the RPA-based theories are valid in systems with strongly charged short PEs. In particular, we elucidate the role of Coulomb and excluded volume interactions in the LCO by comparing coacervates to their corresponding neutral systems.

The interfacial properties of complex coacervates are also of great interest, as they play an important role in determining the functionality of polymeric materials. [196, 197, 198, 199, 200, 201] Since the nematic phase is less symmetric than the isotropic and there is a preferential direction along which semiflexible PEs are aligned, the question of the relative orientation of the director and the coacervate interface (which is irrelevant for isotropic

phases) arises naturally. For this reason, we also examine in some detail the preferential orientation of PE chains at the interface between the nematic coacervate and the supernatant.

This chapter is organized as follows. The details of our coarse-grained MD simulations are specified in Sections 4.2. Section 4.3 presents our main results and consists of three parts. First, symmetric coacervates formed from semiflexible PEs of equal stiffness are considered in Section 4.3.1, where we demonstrate the formation of nematic coacervates and discuss the effect of electrostatic interactions on the I-N transition by comparing coacervates with the corresponding solutions of neutral polymers. Second, Section 4.3.2 is devoted to the study of asymmetric flexible-semiflexible coacervates. In Section 4.3.3 we discuss the orientation of semiflexible PEs at the coacervate-supernatant interface. Our findings are summarized in Section 4.4.

4.2 Method

The classic Kremer-Grest model [60] is used to model PEs in an implicit solvent. Specifically, PE chains are represented by spherical interaction sites (beads) connected by springs. The solvent is included implicitly for computational efficiency. As a result, solvent quality is controlled by the non-bonded interactions between the monomers. In our simulations, we consider good (athermal) solvent conditions for the polymer chains. The coacervate is electroneutral, and consists of an equal number of polyanions and polycations, both with chain length $N = 20$. Polyanions are fully charged semiflexible chains while polycations can be either semiflexible or flexible chains, with a fraction of ionic beads $f_+ = 0.5, 0.55, 0.6, 0.75,$ and 1.0. The total number of beads in the system is up to 31000.

The connectivity of beads is provided by a finitely extensible nonlinear elastic (FENE) potential between adjacent neighbors along the polymer backbone

$$U_{FENE} = -0.5KR_0^2 \ln\left[1 - \left(\frac{r}{R_0}\right)^2\right] \tag{4.1}$$

with $K = 30k_BT/\sigma^2$ and $R_0/\sigma = 1.5$. [60] All beads interact through a shifted and truncated Lennard-Jones (LJ) potential, which mimics good solvent conditions:

$$U_{LJ} = \begin{cases} 4\varepsilon\left[\left(\frac{\sigma}{r}\right)^{12} - \left(\frac{\sigma}{r}\right)^{6} - \left(\frac{\sigma}{r_c}\right)^{12} + \left(\frac{\sigma}{r_c}\right)^{6}\right] & \text{for} \quad r \leq r_c \\ 0 & \text{for} \quad r > r_c \end{cases} \tag{4.2}$$

where $\varepsilon = k_BT$, $r_c/\sigma = 2^{1/6}$, and σ is the size of a bead. For this form of the pairwise potential, one can calculate the corresponding second virial coefficient, $B_{LJ} = 2.2\sigma^3$. By equating this value to that for neutral hard spheres, [202] $B_{LJ} = 2\pi d^3/3$, one finds $d = 1.02\sigma$, which we use as an estimate for the thickness (diameter) of the chain.

To simulate semiflexible chains, and to control their chain stiffness, we use an angle potential of the form:

$$U_{angle} = k[1 - \cos\theta_i] \tag{4.3}$$

where the tunable parameter k is a bending constant expressed in units of ε. The angle between adjacent bonds is equal to $\theta_i = \angle(\mathbf{u_{i-1}}; \mathbf{u_i})$ where $\mathbf{u_i}$ is the unit bond vector connecting the i and $i+1$ monomers. [203] Increasing chain stiffness leads to an increasing Kuhn segment length l, which can be calculated as follows: [204]

$$l = \frac{1 + \coth(k) - k^{-1}}{1 - \coth(k) + k^{-1}} b \approx \begin{cases} b, & k \ll 1 \\ 2kb, & k \gg 1 \end{cases} \tag{4.4}$$

where b is the bond length. For our model, we found that $b = 0.968\sigma$. Note that, for low $k \ll 1$, this formula neglects the (moderate) additional stiffening induced by local short-range repulsive interactions, but the system remains isotropic for low k. In contrast, at $k \gg 1$, when the stiffness is sufficiently high to induce LCO, eq. 4.4 is rather precise. In what follows, the stiffness of the chains is quantified by the ratio $l/d \approx l/\sigma$ between the

chain Kuhn segment length and the chain diameter, which is a measure of the local polymer anisodiametry (inequality of the characteristic sizes along different axes). [181]

Coulomb interactions between charged beads are given by

$$\frac{U_{coul}}{k_B T} = \frac{z_i z_j l_B}{r} \tag{4.5}$$

where z_i is the charge valence for species i ($z_i = \pm 1$). We consider Bjerrum length values equal to $l_B = 3\sigma$ and $l_B = 5\sigma$, respectively. Long-range Coulomb interactions are calculated via the Particle-Particle Particle-Mesh (PPPM) method using LAMMPS. [61, 129] The targeted error for the long-range part of the PPPM method is set to 10^{-4}. The velocities and positions of particles are updated using the velocity-Verlet algorithm with a timestep of $0.005\tau_{LJ}$, where $\tau_{LJ} = \sigma(m/k_B T)^{1/2}$ and m is the particle mass.

The number density of polymer beads within the coacervate is denoted by ρ. We further define the equilibrium volume fraction

$$\phi = \frac{\pi}{4} d^2 b \rho = \frac{\pi}{4} \rho \sigma^3 \tag{4.6}$$

of the salt-free coacervate. Here each monomer is considered to be a cylinder of diameter d and height b. In what follows, we preferentially use volume fraction ϕ, which is the function of the number density ρ. We simulate the salt-free coacervate in the NPT ensemble with zero external pressure, $P = 0$, to mimic the coexistence of the coacervate in equilibrium with a highly dilute supernatant phase. [124, 7] We use a cubic simulation box with periodic boundary conditions. The external pressure is maintained through a Berendsen barostat, and constant temperature T is maintained by coupling the system to a Langevin thermostat with damping parameter $\Gamma = 1.0m/\tau_{LJ}$. [124, 7]

Nematic ordering within the system is measured through the orientation order parameter S: $S = 0$ in the isotropic state and $S \to 1$ in the ideally ordered state. S is the largest

eigenvalue of the orientational (order parameter) tensor Q, whose elements are given by:

$$Q_{\alpha\beta} = \frac{1}{\mathcal{N}_c(N-1)} \sum_{m=1}^{\mathcal{N}_c} \sum_{i=1}^{(N-1)} \frac{1}{2}(3\mathbf{u}_{i,m}^{\alpha}\mathbf{u}_{i,m}^{\beta} - \delta_{\alpha\beta}) \tag{4.7}$$

where $\mathcal{N}_c$ is the number of polymer chains and N is the chain length. Here $\mathbf{u}_{i,m}^{\alpha}$ and $\mathbf{u}_{i,m}^{\beta}$ denote the α-th and β-th components of the unit bond vector $\mathbf{u_i}$ connecting the i and $i+1$ monomers of the m-th chain; $\delta_{\alpha\beta} = 1$, if $\alpha = \beta$ while $\delta_{\alpha\beta} = 0$ if $\alpha \neq \beta$. [205] For the symmetric coacervate, we calculate the Q tensor and the resulting order parameter S via a sum over all (semiflexible) chains, as suggested by eq. 4.7. For asymmetric coacervates, Q and S are calculated separately for flexible polycations and semiflexible polyanions.

All simulations are initialized by generating either polymer chains as self-avoiding random walks, or by using a previously obtained nematic state as the initial configuration. Equilibrium is ensured by monitoring the convergence of the coacervate density and the order parameter, and by the decay of end-to-end vector autocorrelation function as a function of simulation time. [7, 124] Block averaging is performed after the system relaxes to the equilibrium. The OVITO package [1] is used to visualize the results of simulations.

4.3 Results and Discussion

4.3.1 Symmetric Coacervates of Semiflexible Polyelectrolytes

To characterize the isotropic-nematic (I-N) phase transition in salt-free coacervates, we start with a symmetric system of semiflexible polycations and polyanions of equal stiffness, i.e., equal bending constants k. This system is similar to a neutral semidilute solution of semiflexible polymers, but the chains also interact via long-range Coulombic forces. We consider fully charged chains, $f_+ = f_- = f = 1$, of $N = 20$ monomers. The chain length was limited to $N = 20$ because of limitations imposed by our computational resources. Choosing longer

chain lengths would require a larger simulation box, a higher number of particles, and longer simulation runs because of the increase in the relaxation time. The Bjerrum length is set to $l_B/\sigma = 3$ to ensure that (i) the system reaches equilibrium within a reasonable amount of computer time and, (ii) the coacervate is sufficiently dense, and hence the bending constant l/d required for nematic phase formation is not too large. At equilibrium, owing to the system's symmetry, the orientational order parameters for polyanions and polycations are equal, i.e. $S_+ = S_- = S$.

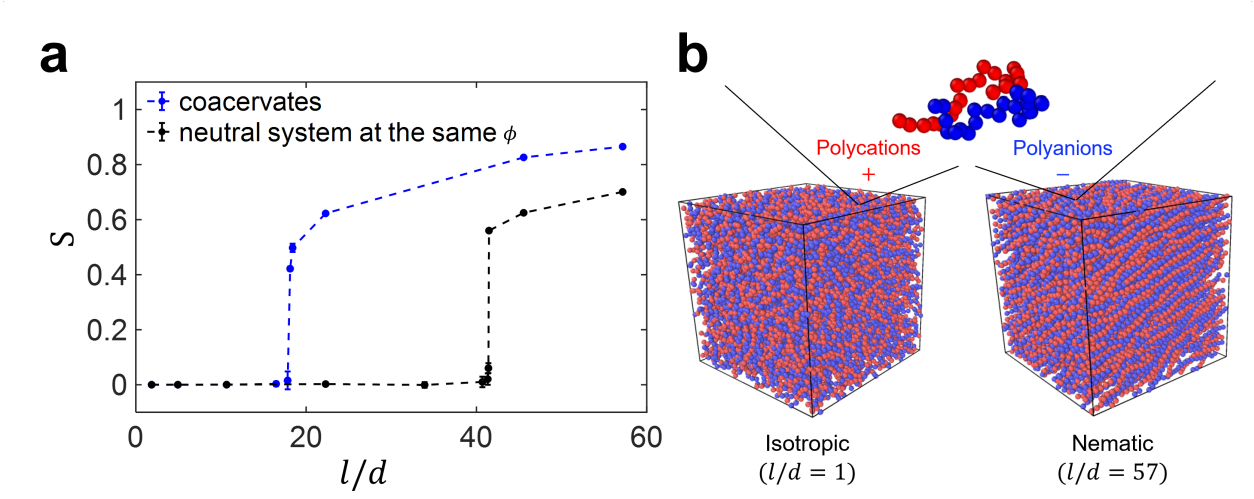

Figure 4.1: a) Dependence of the order parameter S on the chain stiffness l/d for salt-free coacervates (blue curve) and the corresponding neutral semidilute solution of polymers at the same volume fraction ϕ (black curve); b) Visualization of the salt-free coacervate in the isotropic and nematic states, $l/d = 1$ and $l/d = 57$, respectively. Polyanions and polycations are shown in blue and red. Simulation parameters are equal to $f_+ = f_- = 1.0$, $l_B/\sigma = 3$, and $N_+ = N_- = 20$.

The dependence of S on chain stiffness l/d is shown in Figure 4.1a in blue. Increasing chain stiffness induces a transition from the isotropic to the nematic state within the complex coacervate. At $l/d = 18$, the orientational order parameter S increases from 0 to 0.4 in a jump-like manner, which is indicative of a first-order phase transition. As in refs.186 and206, we do not observe the coexistence of isotropic and nematic phases at the transition. In Figure 4.10 of the Section 4.5, we evenly divide the simulation box into 8 cubic sub-regions, labeled with index $i = 1, 2, ..., 8$, and measure the order parameter S_i for each sub-region i

for three different values of l/d near the transition point. These results show that, for each l/d, the values of S_i are independent of the sub-region number i. Therefore, all parts of the system exhibit identical order and there are no signatures of a phase coexistence region in the system. To study whether hysteresis occurs in these systems, we also performed simulations starting from two different configurations, the isotropic state with random chain orientations, and an ordered nematic state. Figure 4.11 in the Section 4.5 shows that the sharp transition happens at almost the same values of l/d in both cases.

A coexistence region (nematic to isotropic) is absent because the coacervate corresponds to a system under a constant external pressure (NPT ensemble), rather than constant volume (NVT ensemble). In the latter case, the I-N phase coexistence always accompanies this first-order phase transition. [181] To corroborate that, we additionally performed NVT simulations of the system at the transition point, for $l/d = 18$. The total polymer density was chosen to be $\phi \approx 0.283$, which is a condition between the isotropic and nematic states observed in NPT simulations near the transition, $\phi_i = 0.28$ and $\phi_n = 0.29$. Figure 4.2 and Figure 4.12 of the Section 4.5 demonstrate the anticipated 2-phase state within the coexisting nematic and isotropic phases of our oppositely charged PEs in the NVT ensemble.

The internal structures of the isotropic and nematic coacervate phases are shown in Figure 4.1b. For $l/d = 1$, the system is homogeneous and isotropic, and no orientation order of PE chains is observed. For $l/d = 57$, stiff, almost perfectly rod-like PE chains are parallel to each other, but no long-range translational order is detected, which is indicative of a nematic liquid crystal.

Isotropic-to-Nematic Transition in the Corresponding Neutral Solution

The observed I-N transition in coacervates of semiflexible PEs induced by stiffness is predicted by theory [193, 194] and resembles that encountered in neutral semidilute solutions of semiflexible polymers. [207, 208, 209, 210, 181, 184, 206, 186] The only difference be-

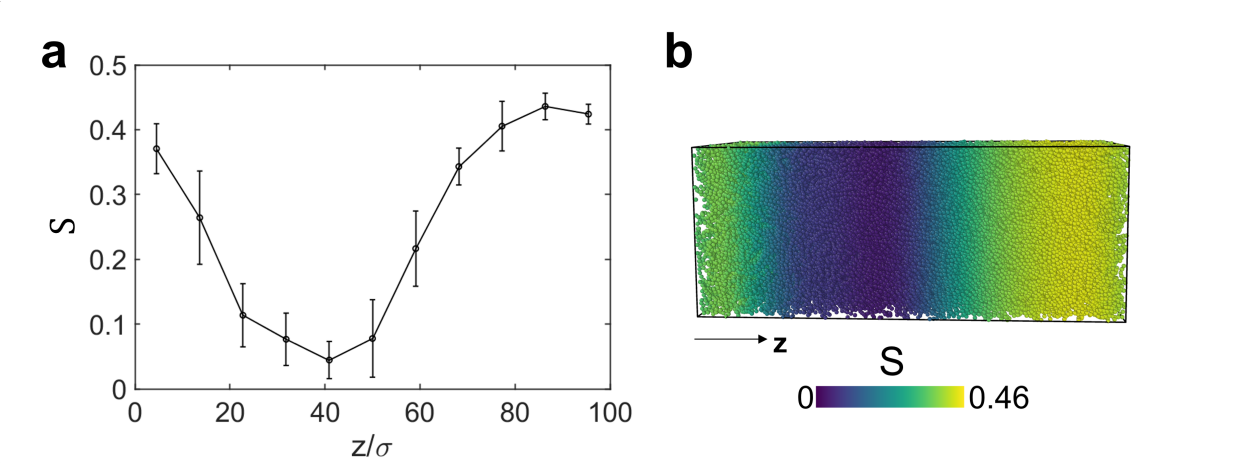

Figure 4.2: a) Average order parameter S as a function of the z-axis position from NVT ensemble simulations of oppositely charged polymers. Average values are calculated by block averaging S for each sub-region of the simulation box (evenly divided the box along z axis). b) Configuration of the system where each monomer is colored by the value of S at its location along the z axis. Simulation parameters are: $f_+ = f_- = 1.0, l_B/\sigma = 3$, chain length $N = 20$, number of chains $\mathcal{N} = 2880$, and box size $X/\sigma = y/\sigma = 40$, $Z/\sigma = 100$.

tween salt-free coacervates and neutral semidilute solutions is the presence of electrostatic interactions. To elucidate their role in the I-N transition, we performed simulations of the corresponding solution of *neutral* semiflexible polymers. To this end, we first obtain the equilibrium density ϕ of the salt-free coacervate formed by semiflexible PEs for each value of l/d. Then, for each value of l/d, we run NVT simulations of semidilute solutions of neutral semiflexible polymers of the same stiffness (i.e., equal k value) at the same density ϕ. The neutral solution corresponds exactly to the salt-free coacervate with Coulomb interactions turned off.

The procedure outlined above was repeated for a series of l/d values; the corresponding order parameters for the neutral semidilute solutions are shown in Figure 4.1a in black. As expected, the neutral semidilute solutions undergo an I-N first-order phase transition at increasing values of l/d. [184, 211] In addition, the coexistence of two phases is also supported by the hysteresis observed in these NVT simulations, which is highlighted in Figure 4.13; for these simulation runs, the neutral system was initialized either from a random state or an

ordered state. [212] At the transition point given by $l/d = 41$, the density of the system is equal to $\phi = 0.33$. One can also find that, at the transition, the dimensionless parameters that define its position are

$$\frac{l}{d}\phi = 13.2 \tag{4.8}$$

or equivalently

$$\frac{L}{d}\phi = 6.6 \tag{4.9}$$

Here the value of the polymer contour length that was used is $L/d \approx N = 20$.

While in simulations of neutral persistent chains molecules adopt almost ideal rod-like conformations and $L < l$, their flexibility is important. We find that the position of the transition differs considerably from the Onsager prediction for ideal stiff rods [213]. Within the Onsager model, the position of the spinodal

$$\left(\frac{L}{d}\phi\right)_{rod} = 4 \tag{4.10}$$

depends on the rod length L, and the transition takes place near the spinodal. [214] Onsager's value differs substantially from that found in simulations and given by eq. 4.9. Furthermore, the observed value of the order parameter S at the nematic phase at the transition, $S = 0.53$, is substantially lower than that expected from the Onsager model, namely $S_{rod} = 0.84$.

In contrast, our results are much closer to those for long polymer chains with persistent semiflexibility.[207, 181] For solutions of infinitely long persistent chains, $L \gg l$, the isotropic state becomes unstable when the Kuhn segment length is sufficiently high [207]

$$\left(\frac{l}{d}\phi\right)_{pers,\, N\to\infty} = 12 \tag{4.11}$$

and, at the transition, the order parameter in the nematic phase equals $S_{pers} = 0.49$. This good agreement between eqs. 4.8 and 4.11 is also consistent with the results of Khokhlov and

Semenov [207], who predicted that even short persistent chains with a contour length as low as $L \approx 0.5l$ are much more akin to long persistent chains rather than short ideal stiff Onsager rods. [207] This effect has been attributed to the role of chain ends. In persistent chains, due to the underlying bending fluctuations, the ends are much less aligned than the middle monomers, even for $L < l$. The Onsager theory of perfectly stiff rods predicts much easier and stronger ordering (that is, a lower l/d transition value and a higher order parameter, S, in the nematic phase) and is inaccurate because it neglects these orientation fluctuations of the polymer ends. [207]

The following spinodal found by Khokhlov and Semenov in ref. 207

$$\frac{L}{d}\phi = \frac{12L/l}{1 - \dfrac{1 - \exp\left(-6L/l\right)}{6L/l}} \tag{4.12}$$

unifies the limiting cases of Onsager's rods and long persistent chains. It reproduces eq. 4.10 for ideally stiff rods, $L \ll l$, and eq. 4.11 for long persistent polymers, $L \gg l$. Substituting the parameters of our system at the transition, $L/\sigma = 20$ and $l/\sigma = 40$, in the r.h.s. of this interpolating formula, one finds $\phi L/d = 8.8$, which is somewhat above the observed value of $\phi L/d = 6.6$. Eq. 4.12 overestimates the spinodal value of L/d because it is based on the Onsager approach to anisotropic excluded volume interactions that considers only *pairwise* repulsions between polymer statistical segments. As any virial expansion, it is limited to low density solutions, $\phi \ll 1$. The density of the studied solution at the I-N transition is relatively large, $\phi = 0.33$, and higher order (at least three-body) contributions become significant.

Onsager's approach to anisotropic repulsive interactions can be systematically generalized to dense polymer solutions by decoupling translational and orientational degrees of freedom. The latter enable the density-dependent renormalization of the second virial coefficient of

anisotropic interactions between statistical segments: [215, 209, 210, 181]

$$B(\gamma) = 2l^2 d \sin\gamma \quad \rightarrow \quad \widetilde{B}(\gamma,\phi) = 2l^2 d \, \frac{|\ln(1-\phi)|}{\phi} \sin\gamma \tag{4.13}$$

where γ is the angle between interacting segments. The Onsager second virial coefficient is reproduced at low densities, $\widetilde{B}(\gamma,\phi) \approx B(\gamma)$ for $\phi \ll 1$. After this renormalization, the modified spinodal, which is an extension of eq. 4.12 for dense solutions, reads

$$\frac{L}{d}\phi = \frac{12L/l}{1 - \dfrac{1-\exp\left(-6L/l\right)}{6L/l}} \times \frac{\phi}{|\ln(1-\phi)|} \tag{4.14}$$

Subsisting $L/l = 0.5$ and $\phi = 0.33$, one finds that the prediction of this modified spinodal, $L\phi/d = 7.3$, is remarkably close to the value observed in simulations, $L\phi/d = 6.6$.

To recapitulate, if we had used much shorter chains, the simulation results would have become closer to the predictions of the Onsager theory for rod-like polymers, which is accurate at $L \ll l$. On the contrary, for much higher N values providing $L \gg l$, simulation results are expected to better agree with the theoretical predictions for long persistent chains. In the case of intermediate chain lengths considered in this work, the unifying formula given by eq. 4.14 should be used to accurately predict the spinodal of the I-N transition.

Comparison between Neutral and Charged Systems

We now return to the I-N transition in the complex coacervate. Compared to the corresponding neutral systems, the coacervate becomes liquid crystalline at substantially lower magnitudes of the chain stiffness. The threshold values differ more than twice, $(l/d)_{coac} = 18$ versus $(l/d)_{neut} = 41$, as seen in Figure 4.1a. This result is consistent with earlier theoretical works [193, 194], which predicted that anisotropic Coulomb interactions between semiflexible PEs facilitate nematic ordering in coacervates.

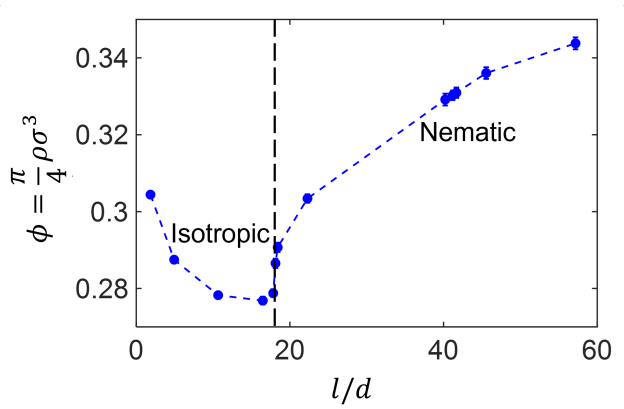

Figure 4.3: Dependence of coacervate volume fraction ϕ on chain stiffness l/d. The black dash line indicates the approximate position of the transition between the isotropic and nematic states. Simulation parameters: $f_+ = f_- = 1.0, l_B/\sigma = 3$.

The dependence of the coacervate density on PE stiffness is shown in Figure 4.3. The vertical dash line given by $l/d = 18$ delineates the isotropic and nematic coacervate states. The coacervate density is a non-monotonic function of l/d, which decreases when the coacervate is isotropic and increases when it is nematic. For isotropic coacervates, a similar decrease in the density has been recently reported in ref. 195. This can be primarily attributed to the increasing strength of excluded volume interactions between randomly oriented segments/rods, i.e. the increase in the second virial coefficient given by eq. 4.13, $B \sim l^2$. Additionally, higher values of l/d lead to effectively lower local fractal dimensions of the PEs (their conformations) and hence weaker Coulomb correlation attractions. [216, 194] At the I-N transition, the nematic ordering of PEs reduces their excluded volume repulsions and enhances their Coulomb attractions, [193, 194] leading to a sudden growth of the coacervate density. (In a similar way, the nematic phase in solutions of neutral semiflexible polymers is always denser than the coexisting isotropic phase. [217, 218, 206, 186, 181]) Finally, in the nematic coacervate, an increase in the PE stiffness improves alignment of the chains. The growth of the order parameter shown in Figure 4.1a, from $S = 0.53$ at the transition to $S \approx 0.8$ for $l/d \geq 40$, results in decreasing steric repulsions and increasing electrostatic attractions, [219, 220, 193, 194] thereby increasing the density of the LC coacervate.

The observations above demonstrate the effect that Coulomb interactions have on the macroscopic phase behavior of coacervates. However, the results shown in Figure 4.1 do not allow us to separate contributions due to the (i) electrostatic stiffening of PEs [221, 222, 223, 224, 225] and the (ii) bare anisotropic, orientation-dependent Coulomb interactions. [219, 220, 193, 194] We emphasize that the former effect facilitates nematic order indirectly, through the renormalization of the net polyion stiffness. This effect has been neglected in past theoretical considerations of LC phases of semiflexible PEs, which mostly deal with perfectly stiff, rod-like chains. In contrast, theoretical models [219, 220, 193, 194] predict a strong role for the second factor. It is therefore of interest to examine these predictions more rigorously by untangling contributions (i) and (ii).

In our simulations we can consider the conformational statistics of each PE within the coacervate phase. To this end, we again compare complex coacervates and neutral semidilute solutions of equal density, but now we match *chain conformations*, as opposed to only non-electrostatic contributions due to the chain stiffness, l/d. We emphasize that conformations are representative of the net persistent length of the chains, which for PEs includes two terms, $l_{tot} = l_0 + l_{el-st}$. Here l_0 is the "bare" stiffness of the polymer in the absence of Coulomb interactions, which is defined by the bending constant k in the angle potential of eq. 4.4, and l_{el-st} represents the electrostatic stiffening. [221, 222, 223, 224, 225]

The comparison procedure is as follows. For the coacervate simulations at a given bare stiffness of the PEs, $l_0/d = (l/d)_{coac}$, we calculate the mean-square internal distance $\langle R^2(n)\rangle$. Then simulations of the neutral solution of equal density are performed and the stiffness of the neutral chains $l_{tot}/d = (l/d)_{neut}$ is adjusted to provide a $\langle R^2(n)\rangle$ that coincides with that of the PEs within the coacervate. One can expect $(l/d)_{neut} > (l/d)_{coac}$, and the difference between these values corresponds to the effective electrostatic persistent length of the PEs

within the coacervate:

$$\frac{l_{el-st}}{d} = \frac{l_{tot} - l_0}{d} = \left(\frac{l}{d}\right)_{neut} - \left(\frac{l}{d}\right)_{coac} \tag{4.15}$$

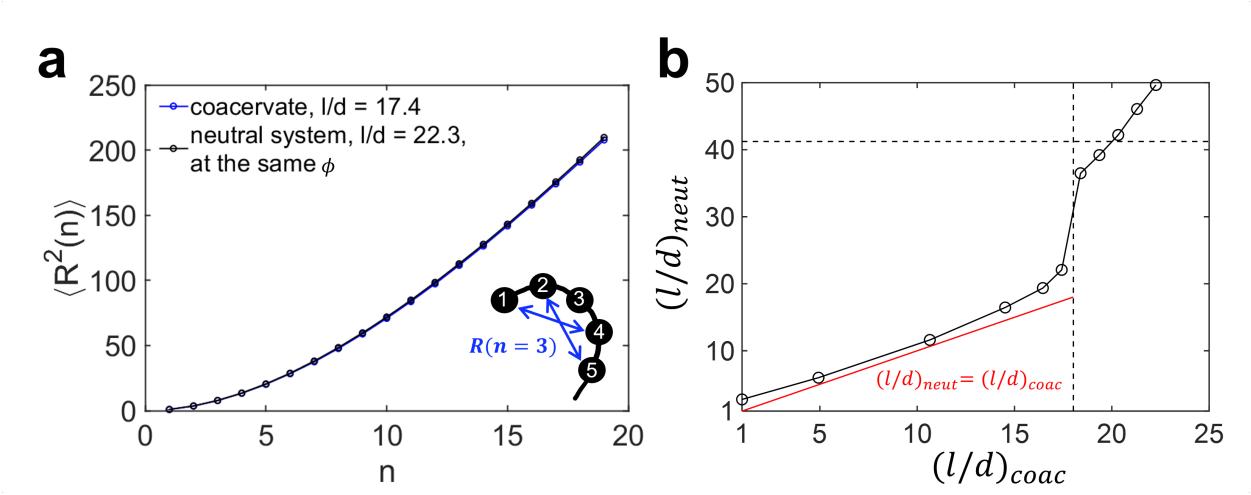

Figure 4.4: a) Mean-squared internal distance $\langle R^2(n)\rangle$ of PE chains in the salt-free coacervate (blue) and for neutral polymers in the respective semidilute solution with the same polymer volume fraction, ϕ (black). The schematic illustrates the value of $\langle R^2(n)\rangle$ for $n = 3$. b) Dependence of chain stiffness in neutral semidilute solutions, $(l/d)_{neut}$, on the bare stiffness of PEs in the complex coacervate, $(l/d)_{coac}$. Neutral solutions and coacervates have equal densities and identical chain conformational statistics. The red solid line is given by $(l/d)_{coac} = (l/d)_{neut}$, and the vertical and horizontal dash lines denote the positions of I-N transitions in coacervates and neutral solutions, respectively. The simulation parameters are $f_+ = f_- = 1.0$ and $l_B/\sigma = 3$.

An example that illustrates this procedure is provided in Figure 4.4a. The polymer statistics in the neutral semidilute solution at $(l/d)_{neut} = 22.3$ are very close to those of PEs in the coacervate at $(l/d)_{coac} = 17.4$, as evidenced by the agreement between the blue and black curves. The process of matching neutral and charged polymer chains was performed over a wide range of chain stiffness $(l/d)_{coac}$, and the results are summarized in Figure 4.4b. Here, each point corresponds to a pair of values, $((l/d)_{coac}; (l/d)_{neut})$. The vertical and horizontal dashed lines, given by $(l/d)_{coac} = 18$ and $(l/d)_{neut} = 41$, denote the transition between the isotropic and nematic states in the coacervate and in the corresponding neutral solution,

respectively. We emphasize that the horizontal dashed line intersects the obtained curve at $(l/d)_{coac} \approx 21$, which is noticeably higher than the transition value for the coacervate, $(l/d)_{coac} = 18$. That is, at $18 < (l/d)_{coac} < 21$ the coacervate is a nematic LC, but the respective neutral solution of the same density and the same net polymer stiffness remains isotropic. This result serves to clarify the role of factor (ii), and it proves that anisotropic Coulomb interactions between stiff/semiflexible PEs enhance their orientational order, as expected theoretically. [219, 220, 193, 194]

The red straight line in Figure 4.4b is given by $(l/d)_{coac} = (l/d)_{neut}$, and it corresponds to the equality between bare and net persistent length, $l_{tot} = l_0$. Below the I-N transition point, the black curve is only slightly above this straight red line, indicating minor contributions from the electrostatic stiffening [221, 222, 223, 224, 225] to the net persistent length of the PEs. The strong growth in the apparent persistent length at $(l/d)_{coac} > 18$ is due to the orientation order of the PEs. (We recall that, for $18 < (l/d)_{coac} < 21$, their conformations are comparable to those of the neutral polymers in the isotropic solution.)

Another way to highlight the role of Coulomb interactions in the intra-coacervate LC order is to compare the position of I-N transition across coacervates of PEs with different fractions of ionic monomers. We consider systems with a fixed value of $f_- = 1.0$, and a series of f_+ equal to $1.0, 0.75, 0.6, 0.55$, and 0.5, with the charged/neutral monomers as evenly spaced as possible in the polycations to minimize the effect of sequence. [41] To separate the contributions due to Coulomb and excluded volume interactions, the coacervates are compared to the respective neutral semidilute solutions of equal density. The dependence of the order parameter S on the bending constant k is shown in Figure 4.1a for $f_+ = 1.0$ and in Figure 4.14 of Section 4.5 for $f_+ = 0.75$ and 0.5. To quantify the I-N transition, we use the value of the chain stiffness at the transition, l/d, which corresponds to a sharp increase of the order parameter, S.

Figure 4.5 shows the transition values of l/d plotted as a function of f_+. The blue and

black curves correspond to coacervates and neutral solutions, respectively. The black curve represents the position of the I-N transition in the absence of Coulomb forces, when LC ordering is driven solely by excluded volume interactions. Two conclusions can be drawn on the basis of the results in Figure 4.5. First, electrostatic interactions facilitate the phase transition since the threshold stiffness l/d is always lower in their presence (the blue curve is below the black one). Second, the difference between the threshold l/d values goes down as f_+ increases. This effect has been theoretically predicted in our earlier work, ref. 194, for asymmetric semiflexible-flexible coacervates (see Figure 9 therein) and can be explained as follows. The high charge density of PEs results in a high coacervate density. Coulomb interactions play a dominant role in LC order at low coacervate densities while, in dense coacervate phases, excluded volume interactions are the key factor for the nematic phase formation. [194] For this reason, the values of l/d for coacervates and for neutral solutions are the closest when the polycation ionization is the highest, $f_+ = 1$.

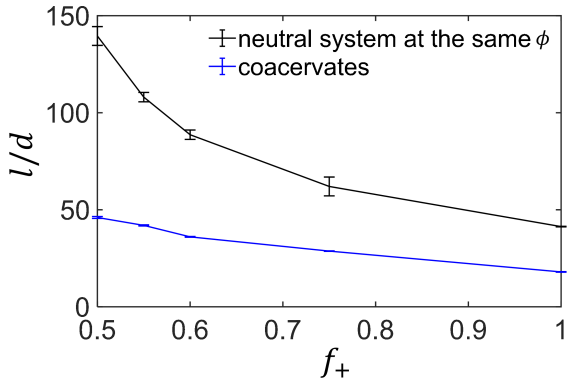

Figure 4.5: Dependence of the stiffness l/d at the I-N transition on the charge fraction of polycations f_+ for salt-free coacervates (blue), and the corresponding solutions of neutral polymers with equal density ρ (black). The error bar indicates the estimated range of l/d values at the transition from the isotropic state to the nematic state (corresponding to a sudden increase of the order parameter S). The simulation parameters are: $f_- = 1.0$, $l_B/\sigma = 3$, and $N = 20$.

While the predictions of the RPA theory [193, 194] and our simulations are consistent with each other, the the agreement is not quantitative. For example, one can consider

the symmetric coacervate with $f_+ = f_- = f$. Following the analysis for neutral solutions performed in Section 4.3.1, it is reasonable to approximate PEs as long persistent chains. In this case, the resulting spinodal can be written as [194]

$$\frac{l}{d}\phi = \frac{12}{1 + \frac{\pi f^2 l_B}{3\phi d}} \tag{4.16}$$

and the second term in the denominator quantifies the relative importance of Coulomb interactions in inducing LCO. When it is much lower than unity, excluded volume interactions dominate, and eq. 4.16 reduces to the result for neutral persistent chains, eq. 4.11. In contrast, at $\pi f^2 l_B/3\phi d \gg 1$, Coulomb interactions are dominant. Substituting $l_B/d \approx l_B/\sigma = 3$ and $f_+ = f_- = 1$ into the r.h.s. of eq. 4.16, we find that the theoretical prediction, $l\phi/d = 1.17$, differs drastically from the simulated value of the l.h.s. at the I-N transition for the coacervate, $l\phi/d = 5.04$. Since agreement for neutral chains was reasonable, this mismatch highlights that the RPA-based theory strongly overestimates the role of Coulomb interactions. Another way to see this is to calculate $\pi f^2 l_B/3\phi d \approx 11 \gg 1$. In fact, this parameter should be on the order of unity because the l/d value for coacervates with $f_+ = f_- = 1$ differs from that for the respective neutral solutions by only a factor of two.

This discrepancy can be attributed to the limited applicability range of theories based on the RPA, which are only justified for weakly charged coacervates, [193, 194] $f^2 l_B/d \ll 1$. In contrast, simulations are performed at high Bjerrum lengths, $l_B/d \approx 3$, and high PE ionizations, $f = 1$, which represent the fully charged homoPEs that are studied in experiments, when correlations are strong. To quantitatively corroborate the theoretical predictions of ref. 194 and access intra-coacervate LC ordering at low f and l_B values, simulations of much longer chains are required. The latter are computationally demanding. To quantitatively match the simulation results presented here, the RPA-based theory of refs. 193 and 194 should be extended to include strong charge correlations. This can be

potentially achieved by following the method of our recent work 226, namely, by taking into account the discreteness of charges in PEs [220] and the finite number of fluctuation wave-modes in the system. [227] The second aspect appears particularly important for stiff PEs with rigidly connected neighboring charges that have no independent translational degrees of freedom, [226] and neglecting it may be the primary reason behind the standard RPA's limitations.

4.3.2 Asymmetric Coacervates of Semiflexible Polyanions and Flexible Polycations

In this subsection, we consider coacervates with a stiffness asymmetry, formed from semi-flexible polyanions and flexible polycations. These systems represent a minimal model of coacervates formed from dsDNA and a flexible, oppositely charged polyanion such as PLL. Such systems have been studied in recent experiments. [188] An additional motivation to simulate these coacervates is a desire to test several theoretical assumptions and conclusions from our recent work, ref. 194.

The simulation setup and procedure are similar to those mentioned in Subsection 4.3.1, except that an angle potential is only used for polyanion chains. We first calculate the order parameter S_- only for the polyanions to quantify the nematic order in the coacervate. These results are shown in Figure 4.6. Here, we use a larger Bjerrum length, $l_B/\sigma = 5$ instead of the $l_B/\sigma = 3$ value that was used for stiffness-symmetric coacervates in Section 4.3.1; we do so to provide easier access to low values of f_+, which we consider in what follows.

The observed I-N transition, which is accompanied by a sudden change in S_-, has been theoretically predicted. [194] Note that previous theoretical work neglected the ordering of flexible polycations and assumed $S_+ = 0$ both below and above the transition. We examine this assumption by calculating the nematic order parameter S_+ for flexible polycations. The results for S_- and S_+ for two coacervate systems, one with $f_- = f_+ = 1.0$ and another

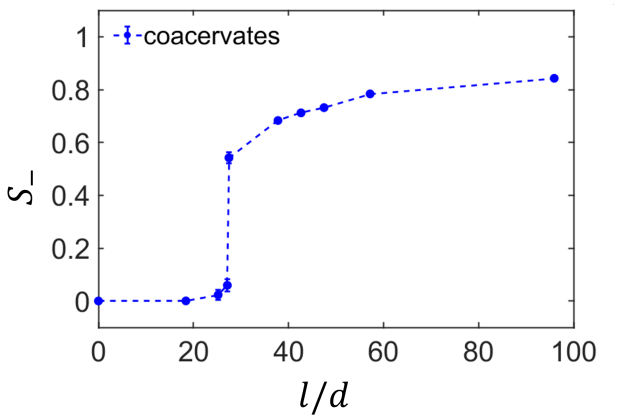

Figure 4.6: Dependence of the order parameter S_- semiflexible polyanions on their stiffness l/d for salt-free coacervates. The simulation parameters are $f_+ = f_- = 1.0$ and $l_B/\sigma = 5$.

with $f_- = 1.0$, $f_+ = 0.5$, are shown in Figure 4.7. One can see that the I-N transition in complex coacervates is accompanied by a weak ordering of the flexible polycations, with the corresponding order parameter S_+ being in the range of 0.15–0.2. We emphasize that S_+ is approximately 4 times lower than the corresponding value S_- for semiflexible polycations, which makes the theoretical assumption of ref. 194 reasonable, though not quantitative. The nematic ordering of flexible polycations is induced by the strong ordering of the semiflexible polyanions and the Coulomb attractions between oppositely charged PEs. The role of the second factor can be clearly seen by comparing the results in Figure 4.7a and 4.7b. As f_+ decreases from 1 to 0.5 and electrostatic attractions weaken, the order parameter S_+ for flexible chains decreases from around 0.2 to 0.1, while the value of S_- remains almost unchanged. Hence, one can expect that, for PEs with low charge densities, $f_\pm \ll 1$, which we considered in ref. 194, S_+ should be sufficiently close to zero.

Also note that a similar ordering of flexible chains induced by the ordering of stiff chains has been reported in simulations of mixtures of neutral amphiphilic polymers with different stiffness, [228] although attractions between the polymers of various types were induced by poor solvent conditions, rather than Coulomb interactions between them.

For stiffness-asymmetric coacervates, separating the roles of Coulomb and excluded vol-

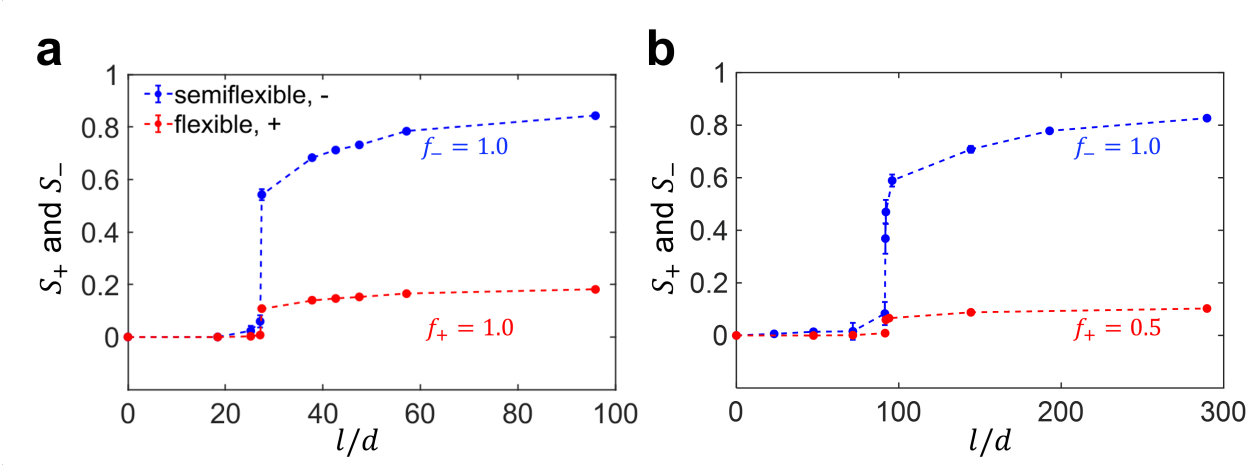

Figure 4.7: Dependence of the order parameters S_- and S_+ for semiflexible polyanions (blue curve) and flexible polycations (red curve), respectively, on polyanion stiffness l/d in salt-free coacervates with different polycation charge densities: a) $f_+ = 1.0$; b) $f_+ = 0.5$. Other simulation parameters are $f_- = 1.0$ and $l_B/\sigma = 5$ for both plots.

ume interactions is more challenging because direct comparison of results for coacervates with those for neutral semidilute solutions is not always possible. This arises because, in mixed neutral solutions, flexible and semiflexible chains are prone to segregation from each other, forming two coexisting macroscopic phases, one isotropic and one nematic. For this reason, we were unable to perform a comparison of the coacervate with $f_+ = f_- = 1$ to the respective neutral solution. The latter does not remain in one phase, and the corresponding order parameter for the homogeneous neutral solution (shown in Figure 4.1 for the stiffness-symmetric system with the black curve) cannot be added to Figure 4.6.

Figure 4.8 shows that the same effect takes place for the neutral solution corresponding to the stiffness-asymmetric coacervate with $f_- = 1$ and $f_+ = 0.5$. For $f_- = 1$ and $f_+ = 0.5$, simulation configurations of the uniphase complex coacervate and the respective phase-separated neutral solution are shown in Figure 4.8b. One can clearly see two coexisting domains (phases), rich in flexible (red) chains and semiflexible (blue) chains. The nematic phase has lower volume because of the higher density and the stoichiometry of the reference coacervate: There are twice as many flexible chains than semiflexible chains in the system.

To confirm the phase separation of the mixed solution of neutral flexible and semiflexible chains, the cubic simulation box was divided into 8 cubic sub-boxes, and the nematic order parameter S_{-} was calculated for each of them. Note that, for the neutral system, S_{-} denotes the order parameter for semiflexible chains. The dependence of S_{-}^{i} on the sub-box number i is shown in Figure 4.8a and demonstrates that the coacervate remains homogeneous, while the respective neutral system is phase separated. For the latter case, the nematic order parameter is high in the phase rich in semiflexible chains and close to zero for the coexisting phase, which consists predominantly of flexible polymers. For mixed solutions of neutral polymers of different stiffness, a similar demixing transition has also been reported by our group and by others in theoretical studies, [229, 230] Monte Carlo [231, 232, 230, 233, 212] and molecular dynamics simulations. [234, 235, 236]

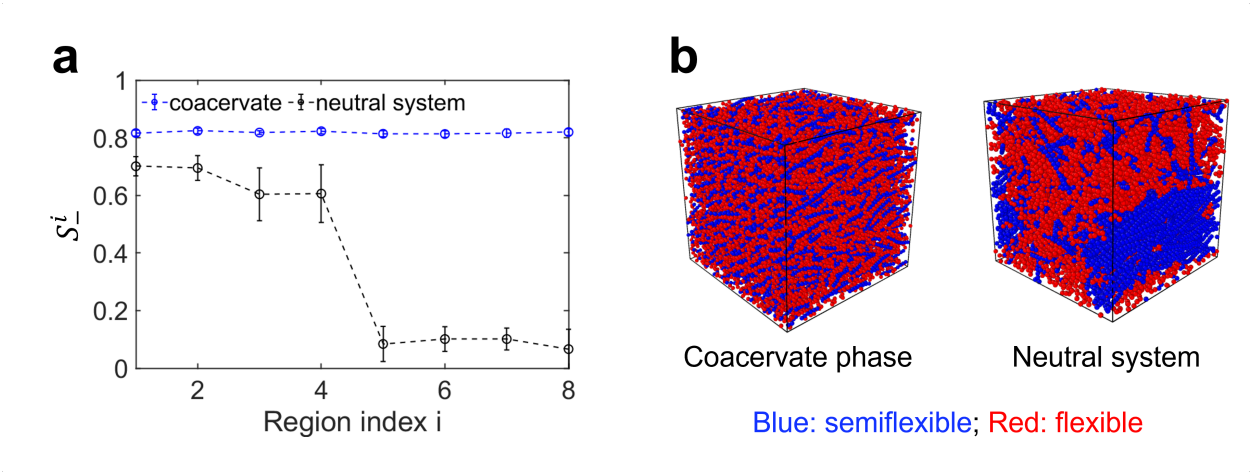

Figure 4.8: a) Order parameter S_{-}^{i} for semiflexible chains in each cubic sub-region of the simulation box as a function of the region index i for the salt-free coacervate at $l/d = 289$ (blue symbols) and the corresponding neutral system of the equal density (block symbols); b) Simulation configurations of these coacervate and neutral systems. Semiflexible and flexible chains — PEs in coacervate and non-ionic polymers in the neutral system — are shown in blue and red, respectively. The simulation parameters are $f_{+} = 0.5$, $f_{-} = 1.0$, and $l_B/\sigma = 5$.

The effective short-range incompatibility between flexible and semiflexible polymers, which is induced by the stiffness mismatch, does not manifest itself in the complex coacervate (see Figure 4.7b). This is due to the strong Coulomb attractions between oppositely

charged PEs, which overcome the weak short-range repulsions. Generally speaking, the formation of a microphase separated complex coacervate can be expected theoretically provided that (i) the difference in the stiffness of the PEs is high and (ii) the fraction of ionic monomers in the PEs is very low, $f_{\pm} \ll 1$. The latter provides a low Coulomb energy for the charge-imbalanced oppositely charged domains rich in polyanions and polycations. This type of electrostatically stabilized microphase separation has been recently studied in coacervates/blends of flexible but chemically incompatible PEs. [179, 180, 137, 237, 238] For the mixture of PEs with unequal stiffness, the only difference is the orientational order inside the domains: Polyanion-rich domains may be nematic, while polycation-rich domains remain isotropic.

4.3.3 Interfacial Orientational Ordering in Nematic Coacervates

Subsections 4.3.1 and 4.3.2 were devoted to a characterization of the macroscopic phase behavior of complex coacervates and the role of Coulomb interactions in such systems. In this subsection, we consider the interfacial properties of nematic coacervates and focus on the chains' orientation at the coacervate-supernatant interface — a phenomenon referred to as anchoring in the liquid crystal literature.

We consider a stiffness-symmetric complex coacervate, which was discussed in Section 4.3.1 and Figure 4.1. At $l/d = 22$ this coacervate is nematic, as was found in NPT simulations. We now perform direct NVT simulations of coexistence between the coacervate and the supernatant phases. The configuration of the nematic coacervate obtained in NPT simulations is inserted inside an empty elongated cuboid box of the same cross-section, as shown in Figure 4.9a. The axis parallel to the longest cuboid size is denoted by z.

Simulations are then performed in the NVT ensemble with periodic boundary conditions; the solvent is included implicitly. This setup enables consideration of the coacervate film between two coacervate-supernatant interfaces, which are approximately perpendicular to

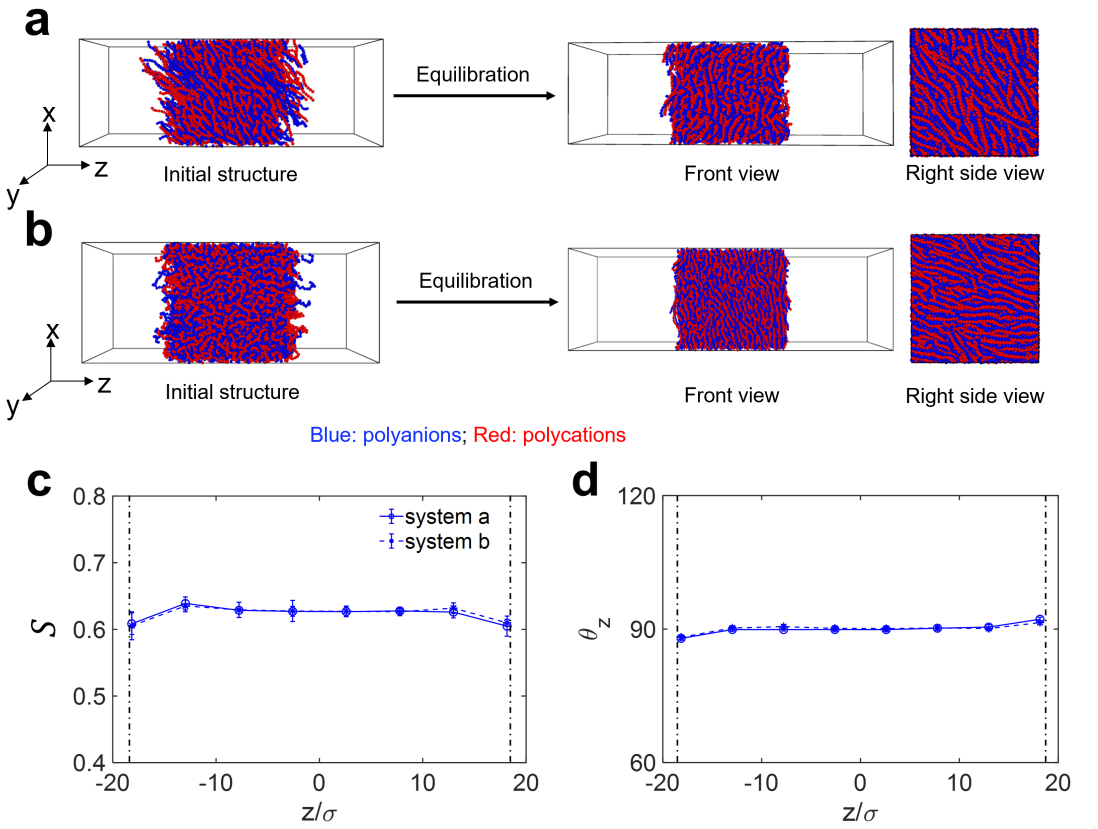

Figure 4.9: Simulation visualization of the interface between a nematic coacervate phase formed from semiflexible PEs with $l/d = 22$ and the supernatant. Figures a) and b) correspond to simulations started from nematic (equilibrium) and isotropic (non-equilibrium) initial states of the coacervate phase, respectively. Polyanions and polycations are shown in blue and red, and the simulation parameters are $f_+ = f_- = 1.0$ and $l_B/\sigma = 3$. Average values of c) order parameter S and d) angle θ_z between bond vectors and the z-axis, along the z-axis, are plotted for systems shown in a) and b) at equilibrium. The center of mass of the coacervate phase is chosen as the origin of the Cartesian coordinate. The two dash-dotted lines in c) and d) mark the boundaries of coacervate phases.

the z-axis.

After equilibration, the coacervate phase remains nematic (as shown in Figure 4.9c), and its density is unchanged, as expected. Snapshots in Figure 4.9a show that, at equilibrium, the PEs align parallel to the coacervate-supernatant interface, i.e., they exhibit homogeneous alignment. The front view demonstrates that very few chain ends protrude from the coacervate into the supernatant, and the interface is flat, with some deviations due to thermal fluctuations and the low coacervate-supernatant interfacial tension. On the right-hand side view, one can see that chains at the interface lie parallel to it, in spite of the fact that they had a different relative orientation in the initial configuration of the system.

To quantify the interfacial ordering of the semiflexible PEs, we calculated the nematic order parameter that characterizes the ordering along the z-axis, i.e., perpendicular to the coacervate-supernatant interface:

$$S_z = Q_{zz} = \frac{3\left\langle \cos^2 \theta_z \right\rangle - 1}{2} \tag{4.17}$$

Here θ_z is the angle between the bond direction and the z-axis. The distribution of θ_z along z-axis is plotted in Figure 4.9d. The resulting average value of $S_z = -0.33$ within the coacervate phase supports our conclusions, as seen in Figure 4.15 of Section 4.5. (Recall that $S_z = -0.5$ would correspond to an ordering perfectly parallel to the OXY plane.) Additionally, it demonstrates that the film thickness is relatively low, and the preferential parallel orientation at the interface induces the same orientation inside the entire film.

To confirm this finding, we performed analogous simulations starting from another initial configuration, in which the coacervate has the same density (that of the equilibrium nematic coacervate for $l/d = 22$) but is isotropic. Figure 4.9b shows that the system relaxes to an identical equilibrium configuration, with nematic order, and homogeneous alignment of the PE chains at the interface.

For our complex coacervates, this result can be rationalized as follows. By adopting the

parallel orientation, the interfacial chains can move/slide freely with respect to each other along the interface while remain inside the nematic coacervate phase. In contrast, if they were perpendicular to the interface, the relative motion of rod-like chains would result in the chains' protruding into the supernatant and a loss of electrostatic interactions with their oppositely charged counterparts, which would be energetically unfavorable. This restricted movement of the chains would result in a lower configurational (translational) entropy of a system with homeotropic (perpendicular) alignment. This entropic difference makes the in-plane, parallel orientation of PEs at the interface theormodynamically favorable. We finally note that the orientational ordering parallel to the interface has also been theoretically predicted for interfaces of coexisting nematic and isotropic phases. [239]

The planar anchoring, which was observed at the coacervate-supernatant interface, is not typical of most liquid crystals. We cannot rule out that this result could be influenced by finite-size effects; the dimensions of the macroscopic coacervate phase in the z-direction exceed the contour length of the semiflexible polyions by a factor of 2, $\Delta Z/L \approx 2$, as seen in Figure 4.9. We also note that the ratio of the box length to the PE length could not be sufficiently large to observe the formation of a smectic phase, which has been documented in systems of neutral stiff rods (spherocylinders) [240] and semiflexible polymers. [187] According to ref. 187, a large simulation box with dimensions exceeding the chain length by an order of magnitude is needed to obtain a smectic phase in a system of neutral polymers. A more comprehensive study of interfacial chain orientation and smectic phase formation will be conducted in the future using large-scale simulations and advanced sampling techniques.

4.4 Conclusions

We have investigated the emergence of liquid crystalline order (LCO) within salt-free coacervates containing semiflexible polyelectrolytes (PEs) using molecular dynamics simulations. PEs were represented within the Kremer-Grest model, augmented with Coulomb interactions

and angle-bending potentials. The main findings of the present work can be summarized as follows:

(i) For both symmetric semiflexible-semiflexible and asymmetric semiflexible-flexible coacervates, the transition from the isotropic to the nematic state (I-N) has been observed at increasing stiffness of the semiflexible chains. This result is consistent with earlier theoretical predictions and experimental findings. The I-N transition is a first-order phase transition accompanied by a pronounced increase in the nematic order parameter S_- of the semiflexible polyanions.

(ii) For stiffness-symmetric coacervates, the density is a non-monotonic function of the PE stiffness l/d. At low l/d, when the coacervate is isotropic, the density decreases with increasing the chain stiffness. However, at the I-N transition, the density abruptly increases and keeps growing with increasing l/d in the nematic state. This is due to the dependence of anisotropic excluded volume repulsions and anisotropic Coulomb attractions on the orientational order of the PEs, S. The higher the order parameter S, the weaker the excluded volume effects and the stronger the electrostatic attractions between the polyions.

(iii) To confirm earlier theoretical predictions concerning how Coulomb interactions facilitate intra-coacervate LCO, [193, 194] the coacervate phase behavior was compared with that of semidilute solutions of neutral polymers of equal density. The I-N transition in the latter systems takes place at approximately twice the value of l/d. While this effect can be partially attributed to the electrostatic stiffening of PEs, a comparison between coacervates and neutral polymer solutions of equal *total* stiffness demonstrates that the transition l/d value remains higher in neutral systems. This is in qualitative agreement with theoretical calculations based on the random phase approximation (RPA). [193, 194] Moreover, a comparison of the I-N transition across coacervates (and the respective neutral systems) having different ionization of polycations demonstrates that Coulomb interactions are the main trigger for the nematic ordering of coacervates with low density. In contrast, when the

coacervate density is high, excluded volume interactions are the dominant driving force for orientational order, as was anticipated by theory. [193, 194]

(iv) For asymmetric semiflexible-flexible coacervates, in addition to the strong nematic ordering of semiflexible polyanions expected by theory, we also observe a weak ordering of flexible polycations, which was neglected in previous theoretical treatments. [194] As an example, for coacervates formed from fully charged PEs, we find $S_- \approx 0.6$ and $S_+ \approx 0.15$ in the ordered phase at the I-N transition. For asymmetric coacervates, we were unable to perform a comparison to neutral systems because the latter undergo a macroscopic phase separation into two phases. This phase separation is absent in coacervates because of the strong Coulomb attractions between oppositely charged PEs. This Coulomb coupling is also the reason for the weak ordering of flexible polycations that is induced by the strong polyanion ordering.

(v) Simulations have revealed a preferential, parallel ordering (planar anchoring) at the interface between the nematic coacervate and the supernatant.

The results presented here could be helpful in understanding some of the molecular mechanisms for prebiotic evolution involving dsDNA and polyelectrolytes, including disordered proteins, and for inspiring new ways of designing coacervate-based materials by turning the stiffness of the underlying molecules.

4.5 Supporting Information

4.5.1 Spacial Distribution of Order Parameter for Salt-Free Coacervates Formed by Semiflexible PEs around Transition Bending Constant

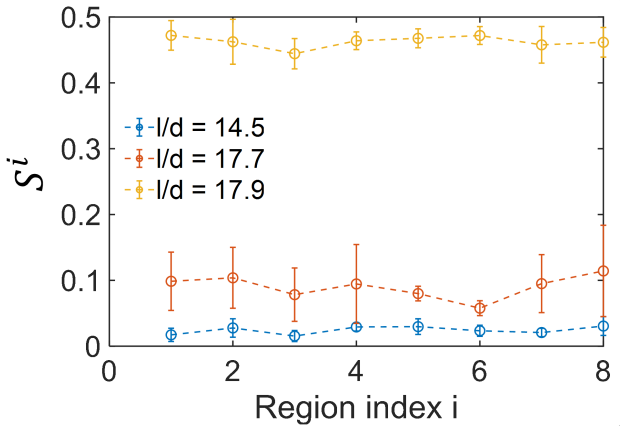

Figure 4.10: Order parameter S^i in each cubic sub-region of the simulation box as a function of region index i for salt-free coacervates at three bending constants. Blue: $l/d = 14.535$; Red: $l/d = 17.762$; Yellow: $l/d = 17.975$. Simulation parameters: $f_+ = f_- = 1.0, l_B/\sigma = 3$.

4.5.2 Isotropic-to-Nematic Transition in Salt-Free Coacervates Formed by Semiflexible PEs with Different Initial Configurations

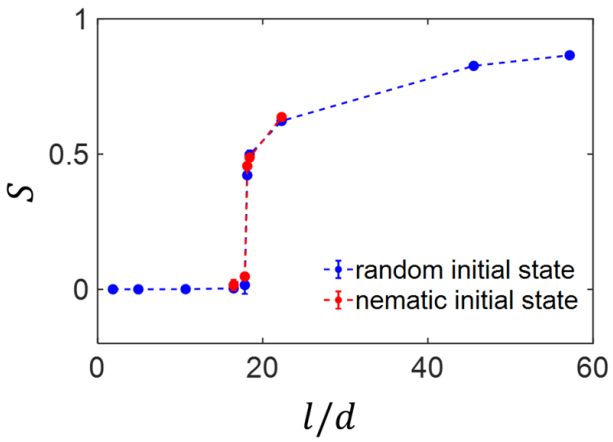

Figure 4.11: Order parameter S as a function of the chain stiffness l/d for salt-free coacervates with different initial configurations. The blue curve shows results for the random initial state (self-avoiding random walk) while the red curve shows results for the nematic initial state. Simulation parameters: $f_+ = f_- = 1.0, l_B/\sigma = 3$.

4.5.3 Coexistence of the Nematic and Isotropic Phases in Charged System with NVT Ensemble Simulation

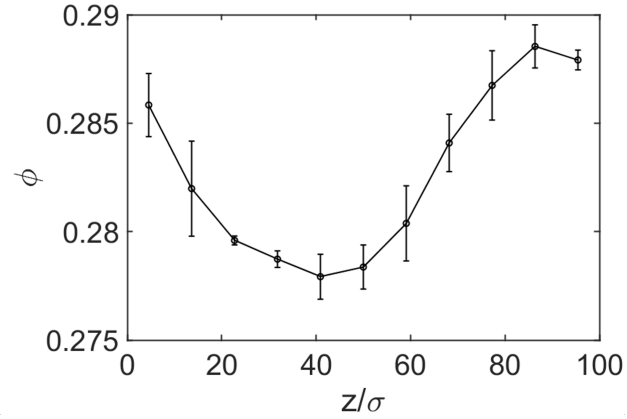

Figure 4.12: The average volume fraction ϕ as a function of z axis position for NVT ensemble of oppositely charged polymers. The average values are calculated by block averaging ϕ for each sub-region of the simulation box (evenly divided the box along z axis). To ensure equilibration, before calculating the average values, long simulation was performed until the profile of ϕ was stable as the simulation time further increased. Simulation parameters: $f_+ = f_- = 1.0, l_B/\sigma = 3$, chain length $N = 20$, number of Chains $n = 2880$, box size $(x/\sigma = y/\sigma = 40, z/\sigma = 100)$.

4.5.4 Isotropic-to-Nematic Transition for Neutral Semiflexible Polymer Solution with Different Initial Configurations

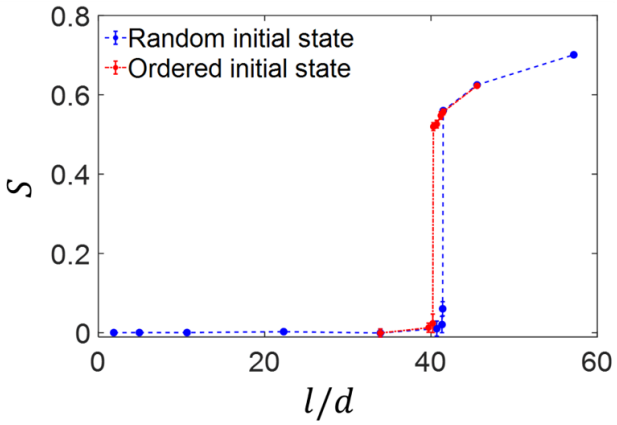

Figure 4.13: Order parameter S as a function of the chain stiffness l/d for neutral semiflexible polymer solution with different initial configurations. The density of each point is the same as the equilibrium density of salt-free coacervates with the same chain stiffness. The blue curve shows results for the random initial state (self-avoiding random walk) while the red curve shows results for the nematic initial state.

4.5.5 Isotropic-to-Nematic Transition in Salt-Free Coacervates Formed by Semiflexible PEs with Different Charge Fractions of Polycations

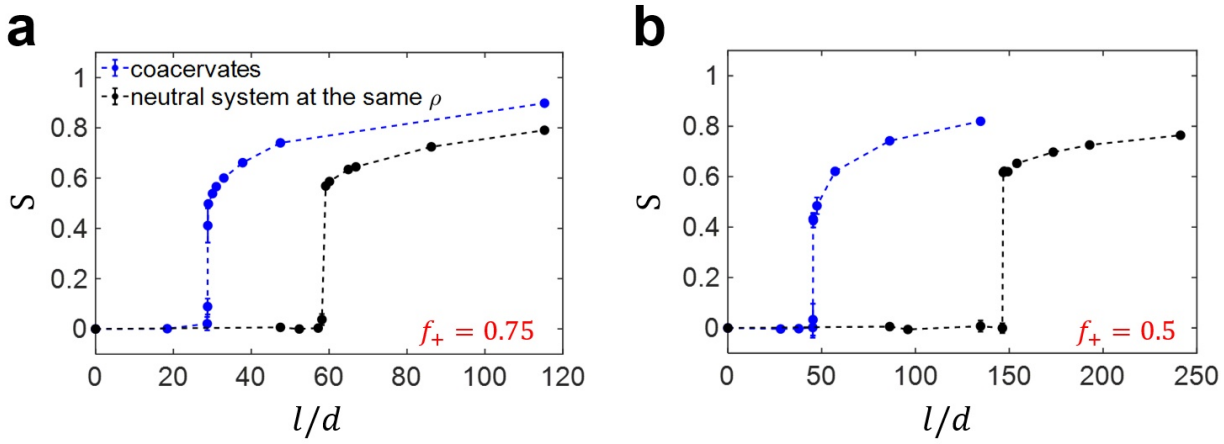

Figure 4.14: Dependence of order parameter S on chain stiffness l/d for coacervates and corresponding neutral system at same density with charge fraction of polycations in coacervates: a) $f_+ = 0.75$; b) $f_+ = 0.5$. Blue curves show results for coacervates while black curves show results for corresponding neutral systems. Simulation parameters: $f_- = 1.0, l_B/\sigma = 3$.

4.5.6 Nematic Order Parameter along the z-Axis of PEs within Salt-Free Coacervate Interfaced with the Supernatant Phases

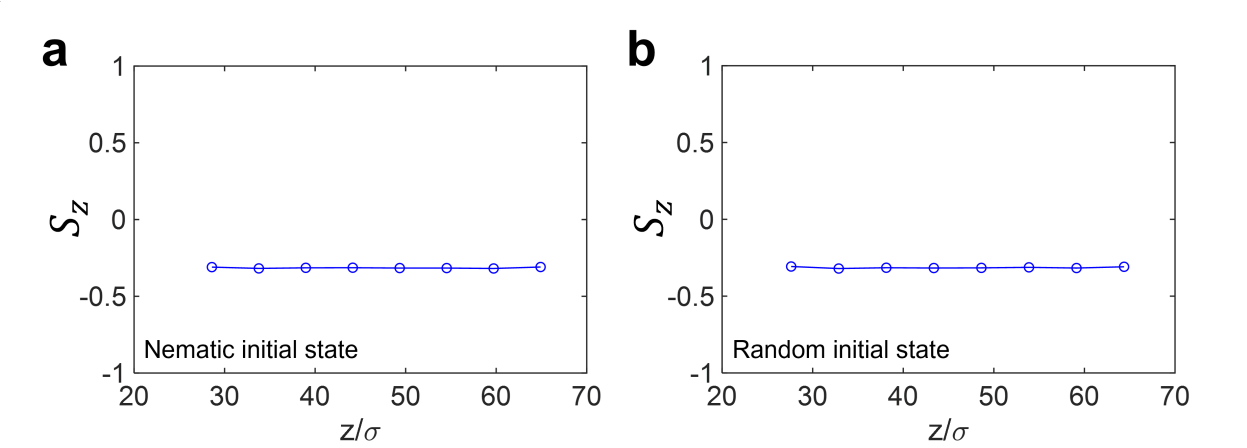

Figure 4.15: The nematic order parameter S_z characterizing the ordering along the z-axis, i.e., perpendicular to the coacervate-supernatant interface, as a function of sub-region center z position for two different initial states: a) nematic initial state (corresponding to Figure 8a); b) random initial state (corresponding to Figure 8b). The errors are within the symbols. Simulation parameters: $f_+ = f_- = 1.0, l_B/\sigma = 3$.

CHAPTER 5

PHASE BEHAVIOR AND DYNAMICS OF HYBRID COACERVATES FORMED BY POLYELECTROLYTES AND COLLOID PARTICLES

5.1 Introduction

Complex coacervation between oppositely charged linear polyelectrolytes (PEs) has been extensively studied theoretically, in simulation, and in experiments. Substantial progress has been made in revealing the relationship between the coacervate properties and the characteristics of PEs, such as the charge fraction, the sequence of monomers, and the chain stiffness. In particular, theoretical and simulation work can rationalize experimental observations and provide valuable predictions regarding the equilibrium and dynamic properties of coacervates formed by linear PEs. [241, 11, 12, 242] However, similar coacervate systems where linear PEs are mixed with other charged colloidal species such as charged solid nanoparticles, micelles of ionic surfactants, or globule proteins, are much less explored and understood.

This work is aimed at systematically studying this type of coacervate and considering how the substitution of one PE component with the charged colloids alters the properties of the resulting coacervate phases. We refer to these colloid-PE coacervate systems as *hybrid* coacervates in order to emphasize their similarity to the conventional interPE coacervates, which are formed as the result of the electrostatically driven phase separation in the solutions of the oppositely charged PEs; this nomenclature also reflects the unique properties of colloid-PE complexes, which emerge due to the introduction of the new, colloidal component. The research interest in hybrid coacervates, especially in those formed by PEs and proteins, has been fueled by the ability of the resulting coacervate phases to stabilize the structure and functionality of proteins. [243] This has promising implications for protein purification, [244, 243] protein separation, [245, 243] antigen delivery, [246, 247] and food

science. [248, 249] Hybrid coacervates can also be viewed as the model systems mimicking intracellular compartmentalization and the formation of membrane-less organelles, particularly those comprising nucleic acids (DNA/RNA) and proteins carrying the opposite, positive net charge. [250, 251]

Experimental studies of coacervates consisting of globular proteins and PEs, revealed that the formation of the coacervate phase can be influenced by many factors including pH, which affects the net charge of the protein, [252, 253] the charge stoichiometry between proteins and PEs, [254, 255] PE stiffness, [256] and the distribution/patchiness of the (generally speaking, opposite) charges at the protein surface. [257] We refer to excellent reviews 253, 258, 259, and 260 by Dubin group and Obermeyer group for a more comprehensive overview of experimental activities in this area.

The similarity between hybrid and conventional coacervates is supported by the available experimental data. For example, an increase in the charge density controlling the strength of the electrostatic interactions has been shown to promote coacervation for both interPE and colloid-PE coacervates. For conventional coacervates of linear PEs, an increase in the fraction of ionic monomers at the fixed chain length leads to denser coacervate phases and their higher salt resistance. [54] Similarly, for hybrid coacervates of green fluorescent protein (GFP) and synthetic or biological polyanions, Cummings and Obermeyer demonstrated that the increase in the net surface charge of GFP from $Q/e = +2$ to $Q/e = +26$ facilitates coacervation in a wider range of pH and salt concentration. [261] Initially observed *in vitro*, this trend also holds *in vivo* for *E. Coli*, where the supercharged GFP with a sufficiently high charge forms intracellular condensates via complexation with RNA. [262]

In addition, the 1D sequence of neutral and ionic monomers in linear PEs and the 2D distribution of charges at the protein surface also influence phase behaviors of usual and hybrid coacervates, respectively, in a similar fashion. For coacervates of linear PEs, the monomer sequence has been shown to govern coacervation in a way that the higher blocki-

ness of charged monomers favors the formation of denser and more salt-resistant coacervate phases. [41, 4, 87, 40] Charge patchiness of the protein surface has an analogous effect on the hybrid coacervates. Comparison across a series of GFP mutants demonstrated that, upon hybrid coacervation with various linear synthetic polyanions, the proteins with a higher anisotropy of the surface charge form condensed phases, which remain stable up to higher concentrations of salt. [257]

Despite recent experimental advances, the number of simulations and theoretical efforts is limited. The computational activity would help to better rationalize available experimental data and guide further experiments. Theory and simulations can also provide valuable predictive capabilities accelerating the targeted design of hybrid coacervate-based materials with predetermined equilibrium and rheological properties. Ref. 263 provides an overview of how Monte Carlo simulations combined with a single chain in mean field methodology have been used to investigate the structure of PE-charged particle mixtures. [263] Within this approach, the conditions necessary for the formation of the macroscopic condensed phase or the finite-size aggregates of nanoparticles with PEs can be found. A similar method has been applied by Ganesan and co-workers to demonstrate the effects of the surface charge patchiness on the coacervation between proteins and PEs. [264, 265, 266] Madinya and Sing considered the phase behavior of hybrid coacervates between worm-like ionic micelles and PEs using a hybrid Monte Carlo and self-consistent field theory model. [267] Albeit these works provided important physical insights into the complexation between PEs and colloids/surfactants, the treatments provided were numerical and limited to the equilibrium structure of the condensed phases.

To provide more universal, analytical considerations of hybrid coacervates and extend theoretical predictions to their dynamics/rheology, our group has recently developed a scaling theory of coacervation between linear PEs and colloids. [6] At that, the latter were treated as charged and impenetrable balls. This method enabled predicting the dependence of coac-

ervate structural properties, such as the average polymer density and the distance between the adjacent colloids, and dynamic properties, such as the coacervate viscosity and colloid diffusion coefficient, on the size and net charge of the colloid. Driven by this theoretical analysis, in the present simulation study, we aim to further explore the system, test scaling predictions and assumptions, and provide molecular-level information to further improve theoretical arguments. Moreover, simulations enable going beyond the limits of the scaling theory applicability and exploring the regions of the parameter space, which are not yet theoretically described, and where new, unexpected system behavior may take place.

In this work, we use coarse-grained molecular dynamics simulations based on the Kremer-Grest model [60] augmented by Coulomb interactions. It has been earlier successfully applied to model both the structural [4, 268, 269] and rheological properties [7, 270] of conventional coacervates. To extend this approach from conventional interPE coacervates to their hybrid counterparts, we replace one type of PE chain with charged spherical particles. In agreement with the theoretical representation [6], we model a colloid particle as a spherical interaction site with the charge either assigned at the center of the sphere or uniformly smeared at the sphere surface. It is important to note that, for the equal size and net charge of the colloid, these two alternatives appear equivalent and lead to identical results. We limit our simulations to the salt-free hybrid coacervates and focus on the dependencies of the coacervate structural and dynamical properties on the nanoparticle size R, charge Q, and PE chain length N. Simulation results are systematically compared to the theoretical scaling (power) laws derived in ref. 6.

This chapter is organized as follows. The details of our coarse-grained model are presented in Section 5.2. Then the results of our simulations are discussed in Section 5.3. Specifically, we first demonstrate the scaling relationships between the structure of coacervates (polymer density and PE layer thickness) and the characteristics of charged particles (size and charges of the particle) in Section 5.3.1. Then we discuss how the bulk modulus of the coacervate

phase is influenced by the particle size and the charges per particle in Section 5.3.2. Finally, to understand the dynamics of the hybrid coacervate phase, the diffusive behavior of charged particles is measured when the chain lengths of oppositely charged PEs vary (polymer dynamics crossovers from Rouse to entanglement dynamics) [7] in Section 5.3.3. The significant findings of this work are summarized in Section 5.4.

5.2 Method

A Kremer-Grest model [60] with electrostatic interactions between charged species is used to simulate the hybrid coacervate phase. Each PE chain is represented by spherical interaction sites (beads) connected by springs. Each chain has the same charge fraction $f = 0.2$, which is the ratio between the number of charged beads and the chain length N. Since the previous studies [39, 40, 41] demonstrate that the charge sequence greatly influences the phase behavior of coacervates, the charged beads are equidistantly distributed along each chain. The charged particles are modeled as spherical particles with different diameters (d) and charges (Q). The charges for each particle are placed at its center. The results are the same when the charges are smeared evenly at the surface of the particle in our simulation conditions (see Section 5.5.1 for detailed comparison). As a result, we choose to use the more straightforward approach to assign the charges at the center of the particle, and the results shown in Section 5.3 are obtained accordingly. The polymers are in the Θ solvent condition in our simulations, and the implicit solvent is used to save computational power.

The connectivity of copolymer chains is represented by Finitely Extensible Nonlinear Elastic (FENE) potential between boned beads:

$$U_{FENE} = -0.5KR_0^2 \ln\left[1 - \left(\frac{r}{R_0}\right)^2\right] \tag{5.1}$$

with $K = 30k_BT/\sigma^2$ and $R_0 = 1.5\sigma$. [60]

All beads interact through a shifted and truncated Lennard-Jones (LJ) potential:

$$U_{LJ} = \begin{cases} 4\varepsilon \left[\left(\frac{\sigma_i}{r}\right)^{12} - \left(\frac{\sigma_i}{r}\right)^{6} - \left(\frac{\sigma_i}{r_c}\right)^{12} + \left(\frac{\sigma_i}{r_c}\right)^{6} \right] & \text{for} \quad r \leq r_c \\ 0 & \text{for} \quad r > r_c \end{cases} \tag{5.2}$$

where ε describes the strength of interaction, r_c is the cutoff radius, and σ_i is the bead diameter. Here $i = m$ is the monomer bead, p is the charged particle, and mix is the size for the mixing rule between the monomer bead and particle. $\sigma_m = \sigma$, $\sigma_p = 2R$ where R is the radius of the particle, and $\sigma_{mix} = \sigma_p/2 + \sigma$. For all bonded beads, $\varepsilon = k_BT$, $\sigma_i = \sigma_m$, and $r_c = 2^{1/6}\sigma_m$ to balance the FENE potential. For all non-bonded monomer beads, $\varepsilon = 0.314k_BT$, $\sigma_i = \sigma_m$, and $r_c = 2.5\sigma_m$ to represent Θ solvent condition. [62] For the LJ potentials between charged particles, $\varepsilon = k_BT$, $\sigma_i = \sigma_p$, and $r_c = 2^{1/6}\sigma_p$. For the LJ interactions between monomer bead and charged particle, $\varepsilon = k_BT$, $\sigma_i = \sigma_{mix}$, and $r_c = \sigma_{mix}$.

The electrostatic interactions in the system are given by:

$$\frac{U_{coul}}{k_BT} = \frac{z_i z_j l_B}{r} \tag{5.3}$$

where z_i is the valence of charge for i species and $z_i = -1$ for charged monomers and $+Q$ for each charged particle. l_B is the Bjerrum length and $l_B = \sigma$ for this work. The Coulomb interaction is solved by the Particle-Particle Particle-Meshm method with the error for the long-range force set to be within 10^{-4}.

To simulate the salt-free coacervate phase in the equilibrium state, the simulation box was maintained in an NPT ensemble with $p = 0$ since the osmotic pressure of the polymers in highly diluted supernatant coexisting with the coacervate is close to 0. [57, 7] This NPT ensemble was achieved by coupling a Berendsen barostat and a Langevin thermostat with damping parameter $\Gamma = 1.0m/\tau_{LJ}$, where τ_{LJ} is the reduced time unit and $m = 1$ is the

reduced particle mass. The bead velocities and positions were updated by a velocity-Verlet algorithm. The time step was set to be $0.01\tau_{LJ}$. The equilibrium of the system is ensured by monitoring the convergence of coacervate density and the relaxation of end-to-end auto-correlation vectors of PE chains. All the properties of the coacervate phase are measured by block average after the systems reach equilibrium.

5.3 Results and Discussion

In this work, we focus on the effects of particle radius R and charges per particle Q on the properties of the hybrid coacervate phase. Thus, as stated in Section 5.2, for all the simulations, Bjerrum length is fixed at 1σ and $f = 0.2$ for each PE chain.

Following the theoretical assumption [6], when studying the system's structural properties and bulk modulus, we also limit our simulations to the charge matching case where the charges on one PE chain equal the charges on one particle but with the opposite sign. Namely, $Q = fN$, where N is the PE chain length. For the investigation of particle dynamics within the coacervate phase, we release this constraint but maintain the overall charge neutrality. We consider two cases: $Q = 24$ and $Q = 40$ per particle. We also study how the diffusion behavior of particles with different radii changes as the chain length N of oppositely charged PEs increases.

Typical snapshots of the salt-free hybrid coacervate phase are shown in Figure 5.1. For both scenarios —charges at the center of the particles (Figure 5.1a) and charge assigned uniformly at the particle surface (Figure 5.1b) — we can see a homogeneous mixture of charged particles and linear PE chains where PE chains can absorb onto particles and form bridges between neighboring particles. Since the two approaches give the same results (see Section 5.5.1 for detailed comparison), for simplicity and computational efficiency, for the rest of this section, we use the simulation results obtained by assigning charges to the center of the particles. The simulation snapshots are generated by software OVITO. [1]

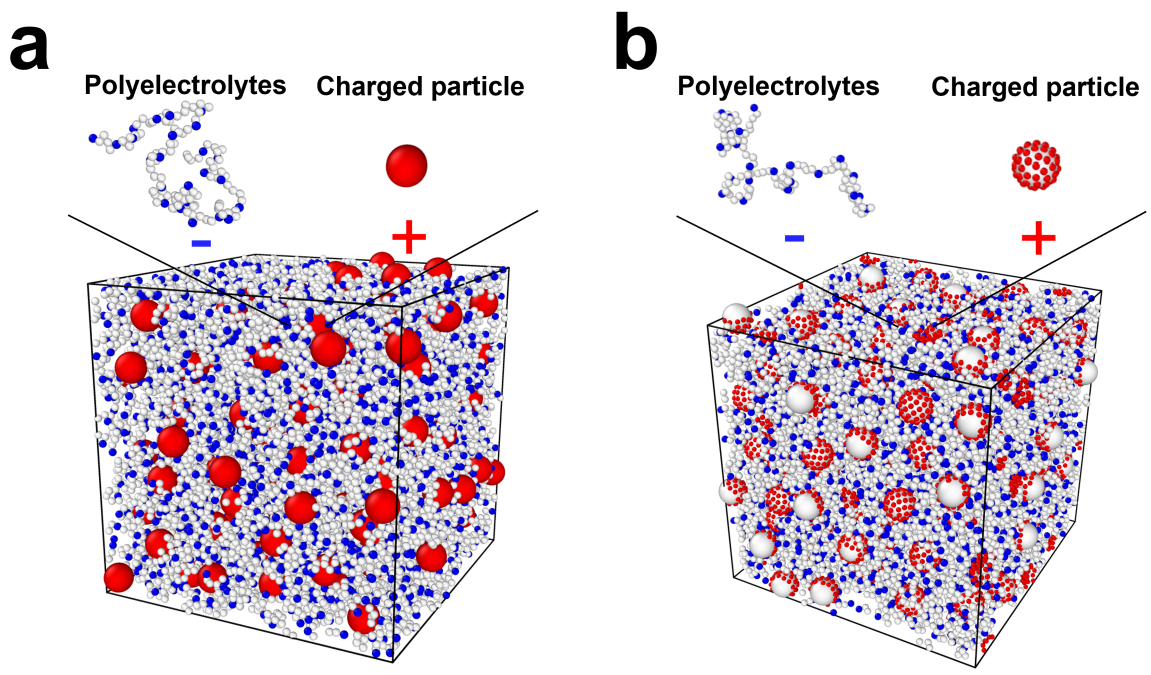

Figure 5.1: a) Snapshot for a hybrid coacervate phase in simulation with the charges Q assigned at the center of each particle. b) Snapshot of a hybrid coacervate phase in simulation with the charges evenly distributed at each particle's surface (64 charged sites in red color). The detailed comparison can be found in Section 5.5.1. The simulation parameters are $f = 0.2, R = 2\sigma, Q = fN = 24$ and $l_B = \sigma$. Blue: negatively charged; Red: positively charged; white: neutral.

5.3.1 Structural Properties of Coacervate Phase

Due to space limitation, we refer to the theoretical paper 6 for detailed derivations and discussions. The critical assumptions for theory are charge matching between a PE chain and a charged particle ($Q = fN$) and no ion pairing as the radius of impenetrable particles is much larger than monomer size. Following the assumptions, the structure of the hybrid coacervate phase is quantified by the structure of the PE absorption layer for each PE-particle pair (absorption of a single PE chain at a charged particle). Precisely, the scaling dependence of polymer number density within the absorption layer ϕ and absorption layer thickness H on particle radius R and charges per particle Q are predicted. Depending on

the strength of absorption (strong and weak absorption) and the geometry of the absorbed PE layer (spherical $H \gg R$ and quasi-planar $R \gg H$), theory predicts three different scaling regimes for the structure of coacervate phase: i) strong spherical absorption (defined as Region I); ii) strong quasi-planar absorption (defined as Region II); iii) weak quasi-planar absorption (defined as Region III). [6]

For Region I:

$$\phi_I \simeq u^{3/5} f^{4/5} Q^{2/5} \tag{5.4}$$

$$H_I \simeq u^{-1/5} f^{-3/5} Q^{1/5} \tag{5.5}$$

where u is the Bjerrum length.

For Region II:

$$\phi_{II} \simeq u^{1/3} Q^{2/3} R^{-4/3} \tag{5.6}$$

$$H_{II} \simeq u^{-1/3} f^{-1} Q^{1/3} R^{-2/3} \tag{5.7}$$

For Region III:

$$\phi_{III} \simeq u^{1/3} f^{-2/3} Q^{4/3} R^{-8/3} \tag{5.8}$$

$$H_{III} \simeq u^{-1/3} f^{-1/3} Q^{-1/3} R^{2/3} \tag{5.9}$$

As the particle radius R increases or charges per particle Q decreases, theory predicts that the scaling behavior changes from Region I to Region II and further from Region II to Region III. The reversed change can also be triggered by the decrease of R or the increase of Q. [6]

Polymer Layer Number Density ϕ

We first study how the number density ϕ of the polymer absorption layer depends on R and Q in our simulations. Here, for our simulations, ϕ is defined as the average monomer number

density within the volume occupied by PEs (subtracting particle volumes from the volume of the simulation box):

$$\phi = \frac{N n_c}{l^3 - 4/3\pi R^3 n_p} \tag{5.10}$$

where n_c is the number of PE chains, N is the PE chain length, l is the length of the cubic box, and n_p is the number of colloid particles.

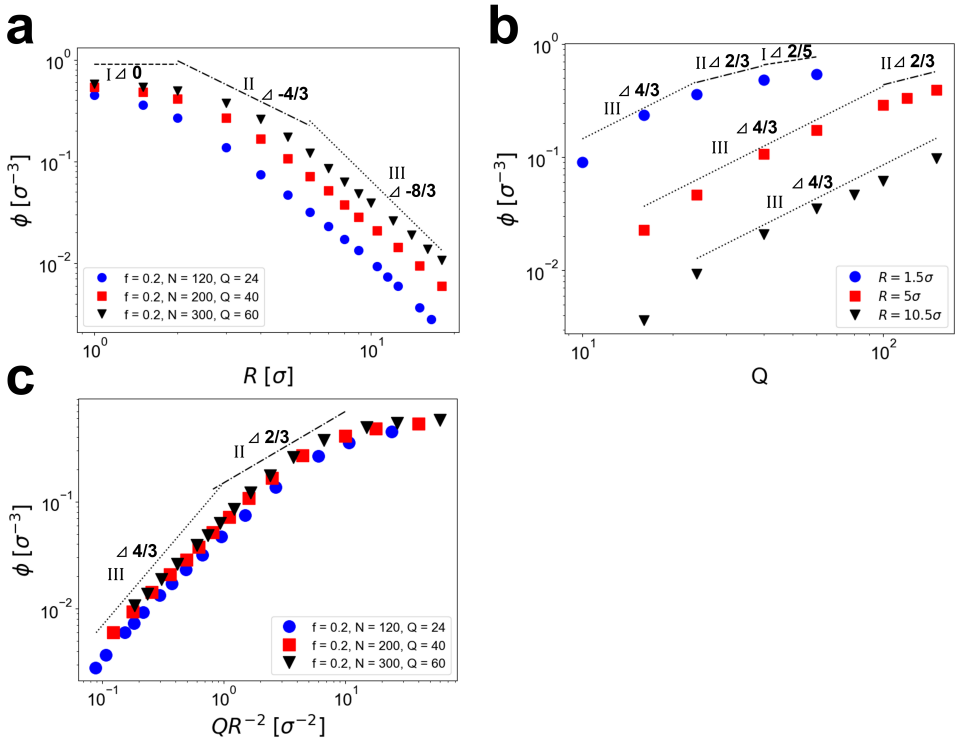

Figure 5.2: a) Polymer layer density ϕ as a function of the particle radius R in log-log scale for $Q = 24, 40$, and 60. b) Polymer layer density ϕ as a function of the particle charges Q in log-log scale for $R = 1.5\sigma, 5\sigma$, and 10.5σ. c) Polymer layer density ϕ as a function of particle surface charge density QR^{-2} in log-log scale for $Q = 24, 40$, and 60. The dots represent simulation data obtained by time average. The errors are estimated by the standard deviation and are within the size of the data points. The straight lines represent the theoretical predictions for each scaling regime. The numbers show the scaling exponents (slopes) following the right triangle symbol. The simulation parameters are $f = 0.2, Q = fN$ and $l_B = \sigma$.

The density ϕ as a function of particle radius R for three different fixed values of charges per particle Q is plotted in Figure 5.2a in a log-log scale. The straight lines have the

same slopes as the theoretically predicted scaling exponents for ϕ and R relationships in three different regimes. From the results, we can see in our simulations that the ϕ also exhibits roughly three different scaling regimes with slopes that closely follow the theoretical predictions. For small R values ($R \leq 2\sigma$), although the density ϕ is not entirely independent of R as predicted for Region I, a clearer plateau can be observed for the curve for $Q = 60$ comparing with the curve for $Q = 24$. For larger R, we can see a intermediate regime with a slope close to $-4/3$ as predicted for Region II develops in our simulation curves. After that, the ϕ decreases much faster as R increases with a slope approximately $-8/3$, which is predicted in theory for Region III. This continuous change of scaling behavior (slopes) from Region I to Region III as the particle radius R increases is also qualitatively in line with the theoretical arguments.

After discussing the scaling behavior for each curve in Figure 5.2a, we can further compare the overall trend across the three simulation curves. The first observation is that as Q increases, the density curve shifts upwards, indicating that for the same particle size, increased charges lead to denser absorption layers. This phenomenon can be understood as the increase of electrostatics enhances coacervation. In addition, as Q increases, the transition between different scaling regimes becomes more noticeable. The crossover positions between each scaling regime also shift to larger R. For example, for $Q = 24$, the dependence of ϕ on R almost continuously drops to $-8/3$ without a clear region of slope 0 or slope $-4/3$. However, for $Q = 60$, a plateau develops up until $R = 2$, and the dependence of ϕ on R reaches the slope of $-8/3$ at a much larger R compared with the case of $Q = 24$. This shift of scaling boundary of the crossover in simulation data is in line with the theoretical predictions. In theory, the crossover between Region I and II, $R_{I \to II} \sim Q^{1/5}$. The crossover between Region II and III, $R_{II \to III} \sim Q^{1/2}$. [6] Both positions of the crossover will shift to larger R values as Q increases, which is observed in the simulation data.

Besides the scaling dependence, the theory also assumes that the absorption layer is

inhomogeneous for Region I. Namely, the polymer layer is denser near the charged particle surface and thinner at the outer layer of the PE-particle pairs. To understand the density distribution in our simulations for Region I, we calculate the average monomer number density within the spherical shell as a function of the distance between the particle center and the shell. From the results for $Q = 40, R = 1.5\sigma$(see in Figure 5.9), we can see the density decreases as the distance increases away from the particle surface, which proves the theoretical prediction of the inhomogeneous structure of the adsorbed layer.

The density ϕ as a function of charges per particle Q for three different fixed values of particle radius R is plotted in Figure 5.2b in a log-log scale. The straight lines have slopes similar to the predicted scaling exponents for ϕ and Q relationships in three different regimes. The simulation results again indicate the change of scaling behaviors (slopes) as Q increases, and the simulation data approximately follows the slopes predicted by the theory. However, the difference between Region II (slope equals to 2/3) and Region I (slope equals to 2/5) is hard to distinguish. The fact that the scaling behavior of simulation data changes from a more significant slope to a smaller slope as Q increases (Region III towards Region I) also agrees with the theoretical predictions, as smaller Q provides weak absorption. In addition, the fact that the density ϕ monotonically increases with the increase of the particle charges Q is also qualitatively in line with the experimental observations. [261]

Like the R dependence, here, the positions of the crossover between different scaling regimes shift to larger Q values for larger R. As a result, for $R = 1.5\sigma$, all three regimes can be approximately distinguished. However, each regime spans very narrow Q values. For larger R, such as $R = 10.5\sigma$, we can only find Region III in our simulation for all Q values considered. This shift of the crossover position for different R values again qualitatively agrees with the theoretical predictions. In theory, the crossover between Region III and II is given by $Q_{III\to II} \sim R^2$. The crossover between Region II and I is given by $Q_{II\to I} \sim R^5$. [6] Both crossovers will shift to larger Q values as R increases, which is again observed

in the simulation data. Another limitation, which does not enable us to reproduce more scaling regimes for larger particles is that it requires huge Q values, which consumes too many computational resources to equilibrate, and the particles start to show structures with the long-range order (see Figure 5.11b in Section 5.5.4) which contradicts the theoretical assumption on the liquid (amorphous) structure of the hybrid coacervate.

According to Eq. 5.6 and Eq. 5.8, for quasi-planar regime (Region II and III), the scaling dependence of polymer layer density on particle radius and charges can be expressed by a single quantity QR^{-2}, which corresponds to the particle surface charge density. Namely, for Region II, $\phi_{II} \simeq (QR^{-2})^{2/3}$. For Region III, $\phi_{III} \simeq (QR^{-2})^{4/3}$. Thus, if we plot the polymer layer density ϕ in Figure 5.2a as a function of QR^{-2} instead of R, we shall be able to collapse the simulation data for three different Q values into one curve in these two scaling regimes (Region II and III). The results are shown in Figure 5.2c, where the data do collapse in Region II and III and the corresponding slope changes from 2/3 to 4/3. The simulation data also collapse in Region I since the polymer layer density *phi* only depends on Q (independent of R) in this scaling regime.

Polymer Layer Thickness H

The thickness of absorption layer H in the simulation is estimated by the equation below:

$$H = \Delta d_p/2 - R \tag{5.11}$$

where Δd_p is the average distance between two neighboring charged particles, and R is the particle's radius. Specifically, Δd_p is measured as the location of the first peak in the particle-particle radius distribution function (see Figure 5.10a in Section 5.5.3 as an example).

The resulting H as a function of particle radius R for three fixed charge values $Q = 24, 40,$ and 60 is shown in Figure 5.3a with the straight lines representing the scaling exponents

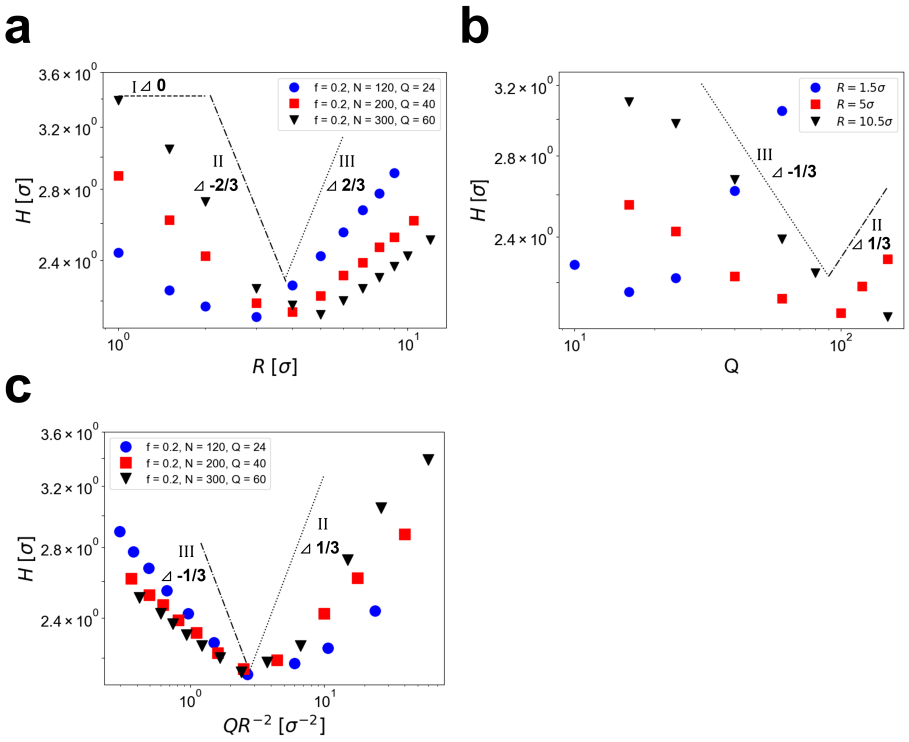

Figure 5.3: a) Polymer layer thickness H as a function of particle radius R in log-log scale for $Q = 24, 40$, and 60. b) Polymer layer thickness H as a function of particle charges Q in log-log scale for $R = 1.5\sigma, 5\sigma$, and 10.5σ. c) Polymer layer thickness H as a function of particle surface charge density QR^{-2} in log-log scale for $Q = 24, 40$, and 60. The dots represent simulation data obtained by averaging over several independent runs. The errors are estimated by the standard deviation and are within the size of the data points. The straight lines represent the theoretical predictions for each scaling regime. The numbers show the scaling exponents (slopes) following the right triangle symbol. The simulation parameters are $f = 0.2, Q = fN$ and $l_B = \sigma$.

(slopes) from the theoretical predictions. The coincidence between the simulation scaling slopes and the theoretical predictions for the H dependence on R is not as good as the previous layer density scaling, especially for Region I where the simulations are unable to show the independence of H on R. However, simulations do preserve the most interesting theoretical prediction: non-monotonic dependence of H on R as the R increases (from $-2/3$ dependence in Region II to $2/3$ dependence in Region III). [6] As shown in Figure 5.3a, all three curves show that the thickness H first decreases and then increases as the particle

radius R increases. The fact that simulation data cannot reproduce the theoretical scaling exponents, as well as the case of layer density vs. R, should be primarily attributed to the lower magnitude of thickness change (no more than 50%) compared with density change (more than ten times) across the different R values.

The simulation results also demonstrate the shift of the crossover positions as Q increases, as discussed in Section 5.3.1. As shown in Figure 5.3a, the minimum of each curve can be used to estimate the crossover between Region II and Region III. As Q increases from 24 to 60, the R value corresponding to the minimum changes from 3σ to 5σ, which agrees with the theoretical prediction that the crossover between II and III shift to larger R as Q increases. In fact, the numerical ratio $5/3 \approx 1.67$ is also close to the scaling prediction $R_{II \to III} \sim Q^{1/2} = (60/24)^{1/2} \approx 1.58$.

Similarly, the dependence of H on the charges per particle Q for three fixed R values is shown in Figure 5.3b with the straight lines representing the scaling exponents (slopes) from the theoretical predictions. Again, due to a minor change of H, the theoretical scaling exponents are not well reproduced in simulations. However, the simulation results corroborate theoretical prediction on the the non-monotonic relationships between H and Q as the Q increases across the Region III (exponent $-1/3$) to II (exponent $1/3$). In addition, the order of scaling regime changes in simulations is also consistent for the dependence of ϕ and H on R (Region I to III) as well as the dependence of ϕ and H on Q (Region III to I), which agrees with the theoretical arguments.

As R increases, the same crossover shift can also be found in Figure 5.3b. The minimum of each curve can be used to estimate the crossover between Region III and Region II. As R increases from 1.5σ to 5σ, the Q value corresponding to the minimum changes from $Q = 10$ to $Q = 100$, which agrees with the theoretical prediction that the crossover shift to larger Q as R increases. In fact, the numerical ratio $100/10 = 10$ is also close to the scaling prediction $Q_{III \to II} \sim R^2 = (5/1.5)^2 \approx 11.11$.

According to Eq. 5.7 and Eq. 5.9, for the quasi-planar regime (Region II and III), the scaling dependence of polymer layer thickness on particle radius and charges can also be expressed by the particle surface charge density QR^{-2}. Namely, for Region II, $H_{II} \simeq (QR^{-2})^{1/3}$. For Region III, $\phi_{III} \simeq (QR^{-2})^{-1/3}$. Thus, if we plot the polymer layer thickness H in Figure 5.3a as a function of QR^{-2} instead of R, we shall be able to collapse the simulation data for three different Q values into one curve in these two scaling regimes (Region II and III). The results are shown in Figure 5.3c. Although the collapse of simulation data in these two scaling regimes is not as good as in Figure 5.2c, we do observe the non-monotonic dependence of H on QR^{-2} and the overlap of minimum positions, which again indicates the universality of our results.

5.3.2 Bulk Modulus B of Coacervate Phase

Based on the predictions for the internal structures of the coacervate phase, the theory further develops the scaling relationships between osmotic properties and particle radius R and charges Q. [6] Here, we focus on the predictions for the bulk/osmotic modulus B of the coacervate phase which quantify its comprehensibility under uniform external pressures along three dimensions.

According to the theory, for both Region I and II:

$$B_{I,II} \simeq uf^2 \tag{5.12}$$

which means that the bulk modulus is independent of both Q and R.

For Region III:

$$B_{III} \simeq uQ^2R^{-4} \tag{5.13}$$

The bulk modulus B is calculated in our simulations following the procedures in Reference 271. Detailed descriptions can be found in Section 5.5.5. The scaling relationships

between B and R are shown in Figure 5.4a for $Q = 24, 40$, and 60. From the results, we can see that the slope approaches 0 at a small R limit, indicating the independence of B on R in Region I and II. For large R, the simulation data also exhibit a scaling slope close to the theoretical prediction -4. Furthermore, similar to the results in Section 5.3.1, the crossover positions between Region II and III for the dependence of bulk modulus B on R also shift to larger R as the charges per particle Q increase.

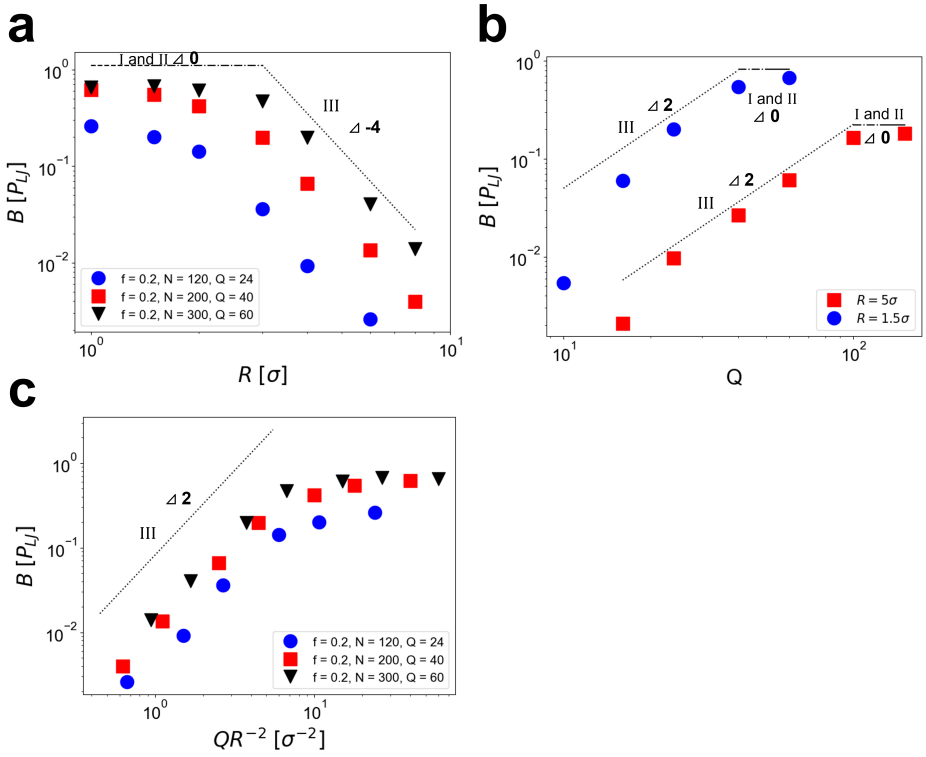

Figure 5.4: a) Bulk modulus B of the coacervate phase as a function of particle radius R in log-log scale for $Q = 24, 40$, and 60. b) Bulk modulus B of the coacervate phase as a function of particle charges Q in log-log scale for $R = 1.5\sigma$ and 5σ. c) Bulk modulus B of the coacervate phase as a function of QR^{-2} in log-log scale for $Q = 24, 40$, and 60. The dots represent simulation data obtained by averaging over several independent runs. The errors are estimated by the standard deviation and are within the size of the data points. The straight lines represent the theoretical predictions for each scaling regime. The numbers show the scaling exponents (slopes) following the right triangle symbol. The simulation parameters are $f = 0.2, Q = fN$ and $l_B = \sigma$.

Similarly, the scaling relationships between B and Q are shown in Figure 5.4b for $R =$

1.5σ, and 5σ. From the results, we can see that both of the curves approach a plateau at large Q, which indicates the crossover from Region III to Region II and I, where B is independent of Q. Before reaching the plateau, the slopes of the two curves are also sufficiently close to 2 the theoretical prediction. The deviation only happens at small Q values, where the electrostatic interactions are very weak. Again, the crossover between Region III and Region II also shifts to higher Q values as the particle radius R increases.

According to Eq. 5.13, for the weak quasi-planar regime (Region III), the scaling dependence of bulk modulus on particle radius and charges can also be expressed by the particle surface charge density QR^{-2}. Namely, for Region III, $B_{III} \simeq (QR^{-2})^2$. Thus, if we plot the bulk modulus B in Figure 5.4a as a function of QR^{-2} instead of R, we shall be able to collapse the simulation data for three different Q values into one curve in the scaling Region III. The results are shown in Figure 5.4c, which demonstrates the collapse of simulation data for Region III with the slope close to the theoretical prediction (2).

5.3.3 Dynamics of Charged Particles

Theory only provides scaling predictions for the dynamics of hybrid coacervates in Region I, where most of the coacervate phase volume is occupied by PEs, and the dynamics are polymer-controlled. Under the theoretical assumption, due to the lack of electrostatic activation barrier, the coacervate dynamics are similar to the dynamics of non-sticky particles in the semidilute polymer solution. [6] As a result, the PE chains will undergo a crossover from Rouse to entanglement dynamics as the chain length N increases. [7, 272] In the meantime, particles smaller than the entanglement tube size are not affected by the entanglement dynamics of polymer chains. Their dynamics are also Rouse-like, and the diffusivity (D_p^{unent}) is determined by the effective viscosity experienced by the particles, which is the Rouse viscosity of of the chain fragment of the characteristic size comparable to the particle radius R.

Thus, the scaling relationships are given as follows:

$$D_p^{unent} \simeq \frac{k_B T}{\eta_s \phi_I^2 R^3} \simeq D_0 u^{-6/5} f^{-8/5} Q^{-4/5} R^{-3} \tag{5.14}$$

where η_s is the solvent viscosity and D_0 is the diffusivity of a single disjointed monomer. [6] If the particle size is larger than the entanglement tube size, they undergo the entanglement effects, which leads to a different scaling behavior:

$$D_p^{ent} \simeq D_0 u^{-14/5} f^{-56/15} Q^{-28/15} R^{-1} N_e^2 N^{-3} \tag{5.15}$$

where N_e is the entanglement strand length in the melt. [6]

Recall that in our simulation, we are only able to test the coacervate dynamics in Region I and its vicinity, and we are using the implicit solvent model. As a result, it is hard to verify the above scaling relationships directly (mainly driven by the change of coacervate density) from our simulation. Instead, we aim to study the applicability of the non-sticky assumption in our simulation and explore the dynamics of charged particles as the length of PE chains changes for two different particle charges, $Q = 24$ and $Q = 40$.

As shown in Figure 5.5a and Figure 5.5b, we first perform simulations for particles with $R = 2\sigma$ and $Q = 24$ and PEs with $f = 0.2$ and various chain lengths. From Section 5.3.1, we know that under this condition, the system is close to the scaling Region I. In Figure 5.5a, the mean squared displacement (MSD) of central five monomers MSD_m scaled by $t^{0.5}$ is plotted as a function of time. From these results, we can see that as the PE chain length increases, the polymer exhibits the crossover from Rouse dynamics ($MSD_m/t^{0.5} \simeq t^0$) to entanglement dynamics ($MSD_m/t^{0.5} \simeq t^{-0.25}$) which is shown by the occurrence of negative slope in the curves for large N ($N > 240$). These results are similar to what we have demonstrated for conventional coacervates. Namely, the dynamics of PE chains in salt-free coacervates are analogous to the dynamics of neutral polymer chains in semidilute solution. [7] While the

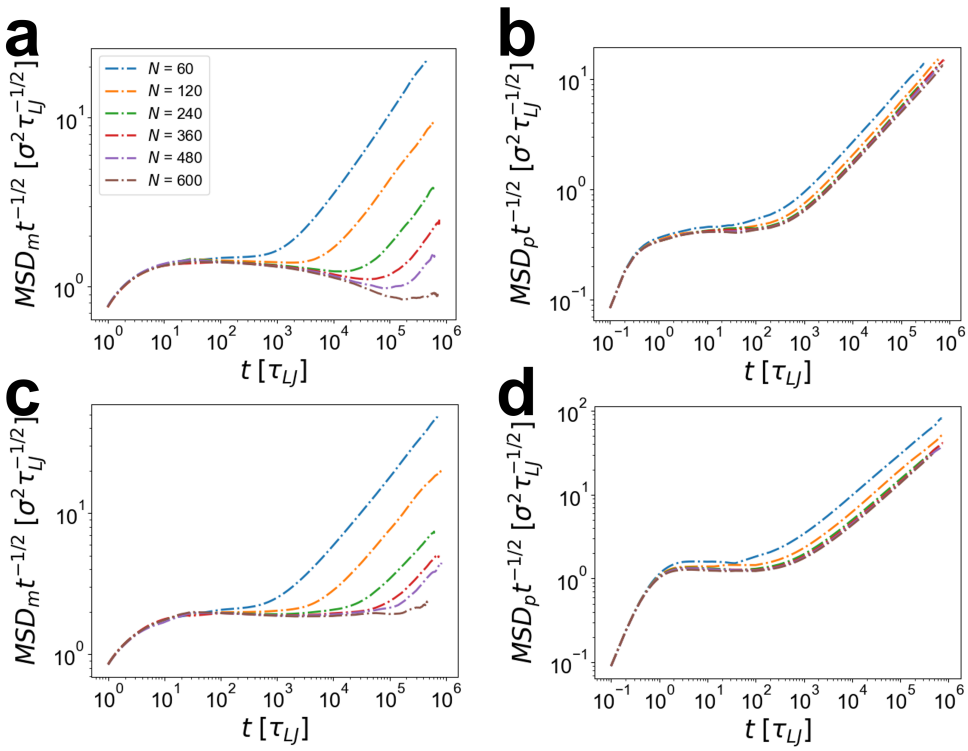

Figure 5.5: MSD of central five monomers of each PE chain MSD_m scaled by $t^{1/2}$ as a function of simulation time for different PE chain lengths for particle radius a) $R = 2\sigma$ and c) $R = 5\sigma$. MSD of particle center of mass MSD_p scaled by $t^{1/2}$ as a function of simulation time for different PE chain lengths for particle radius b) $R = 2\sigma$ and d) $R = 5\sigma$. The simulation parameters are $f = 0.2, Q = 24$ and $l_B = \sigma$.

polymer chains undergo crossover to entanglement dynamics, the particle dynamics remain Rouse-like at the intermediate time scale as shown by the plateaus in Figure 5.5b, which is similar to the predictions for the MSD of non-sticky intermediate size nanoparticles in neutral polymer solutions. [273] This is in line with the non-sticky assumption, as the small particles are unaffected by the entanglement dynamics of polymers.

For the particle to *feel* the entanglement effects, its size should be comparable to entanglement tube size, which can be estimated by $blN_e^{1/2}\phi^{-2/3} \simeq 20$ monomers using $N_e = 70$, Kuhn length $b = 1.82\sigma$, bond length $l = 0.96\sigma$ and $\phi = 0.27\sigma^{-3}$. [203] As a result, a particle size much larger than 27σ is needed to demonstrate the entanglement effects. However,

larger particle size will lead to much smaller coacervate density, resulting in an even larger particle size and longer chain length for the appearance of entanglement effects. Thus, different model parameters and setups are required to reproduce this behavior, which is beyond the scope of this study.

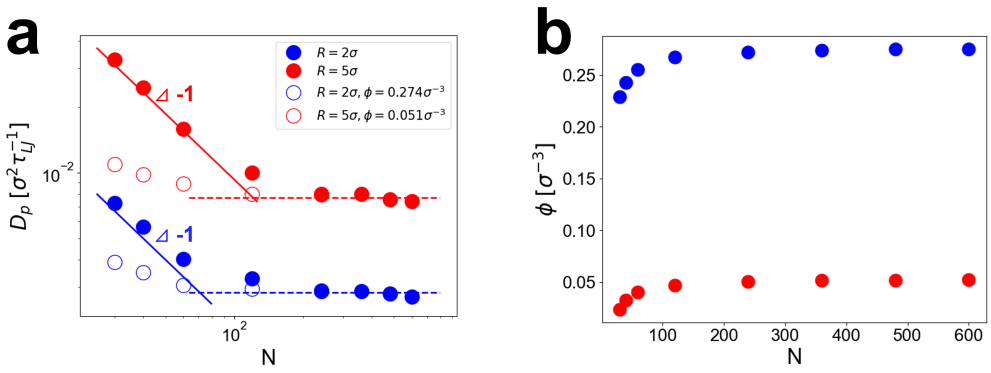

Figure 5.6: a) Diffusion coefficient of particles D_p as a function of PE chain length N. Solid lines have slope -1 while dash lines have slope 0. The errors are estimated by dividing the particles into five groups and calculating the standard deviation of diffusivity for each group. The errors are within the size of each data point. b) Polymer layer density ϕ as a function of PE chain length N. The errors are estimated by the standard deviation of sampling data after equilibrium. The errors are within the size of each data point. The simulation parameters are $f = 0.2, Q = 24$ and $l_B = \sigma$.

Similar simulations are conducted for larger particle $R = 5\sigma$, where the system is in scaling Region III. Due to much smaller density, the polymer chains retain Rouse dynamics even at very long chain lengths, as shown in Figure 5.5c. As expected, the particles also demonstrate Rouse dynamics in Figure 5.5d, which indicates that similar theoretical approaches may be applicable also in Region II and Region III, despite the potential concerns raised in the theoretical paper. [6] To further understand the particle dynamics, the diffusion coefficient of charged particles D_p is obtained by fitting the normal diffusive regime of MSD curves (the regime of large t where MSD is linearly dependent on t). The diffusivity of charged particles with $R = 2\sigma$ and 5σ is shown in Figure 5.6a. From the results, we can see that the larger particles diffuse faster than the smaller particles, which seems to contradict

the theoretical predictions from Eq. 5.14. However, this prediction is valid for scaling Region I while for $R = 5\sigma$, the coacervates are already in Region III. The full scaling relationships between D_p and R for $Q = 24$ is shown in Figure 5.13 in Section 5.5.6, where the diffusivity first decreases weakly with increases of R and then increases as particle size increases. This observation can be attributed to the decrease of coacervate density as particle size increases. Using a similar argument as in Eq. 5.14, we can estimate the scaling relationships between D_p and R for Region II and Region III based on the dependence of density on R. For Region II, $D_p^{unent} \simeq \frac{k_B T}{\eta_s \phi_{II}^2 R^3} \sim R^{-1/3}$. For Region III, $D_p^{unent} \simeq \frac{k_B T}{\eta_s \phi_{III}^2 R^3} \sim R^{7/3}$. This preliminary theoretical estimation also predicts that the non-monotonic dependence of the diffusion coefficient on particle radius, which qualitatively agrees with the simulation results.

Figure 5.6a also shows the relationship between diffusion coefficient and PE chain length N. For both particle sizes, the particle diffusivity first decreases with the increase of N and then reaches a plateau (independent of N), as shown by the solid points. The decrease of D_p follows a slope of -1 indicated by the solid lines. This scaling behavior is in line with the predictions for non-sticky particles in polymer solution for intermediate particle size. [273] It should be noticed here that the -1 slope is predicted for the coacevates of long PEs with the N-independent density. At the same time, for hybrid coacervates, there is a significant decrease of density with the decrease of chain length as shown in Figure 5.6b. To factorize the density and diffusion effects, we also perform NVT simulation and fix the density of the coacervates formed from short PEs to be the same as the density at the long chain limit. The resulting diffusion coefficient is shown in Figure 5.6a with open square symbols. The diffusion coefficient of nanoparticles in coacervates with short PEs decreases since their densities increase. In addition, the diffusion coefficient also decreases slower with the increase of N, and the scaling slope has yet to reach -1 for the chain lengths considered here.

The above results indicate that for small Q values, the non-sticky assumption can be used to estimate the dynamics of charged particles even at scaling Region II and Region

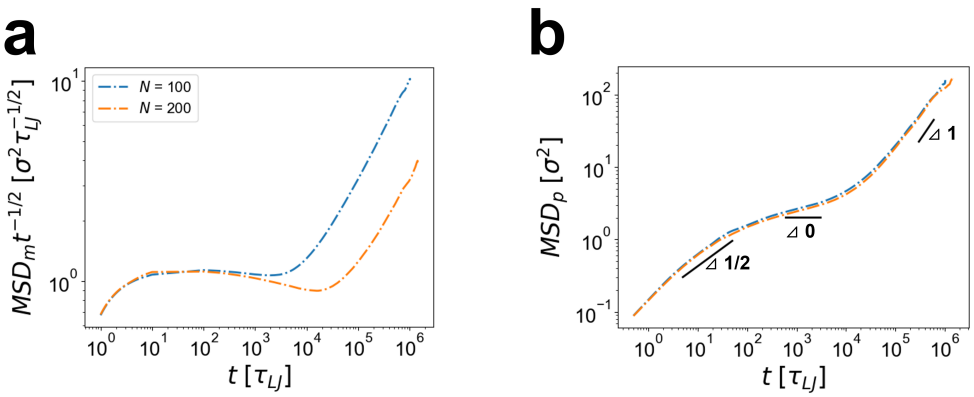

Figure 5.7: a) MSD of central five monomers of each PE chain MSD_m scaled by $t^{1/2}$ as a function of simulation time for different PE chain lengths for particle radius $R = 2\sigma$. b) MSD of particle center of mass MSD_p as a function of simulation time for different PE chain lengths for particle radius $R = 2\sigma$. Each black straight line has the slope indicating by the number close to the right triangle. The simulation parameters are $f = 0.2, Q = 40$ and $l_B = \sigma$.

III beyond what is proposed in the theoretical paper. [6] However, the actual underlying physics for the dynamics of hybrid coacervates can be more complicated, especially as the charges per particle Q increase. Firstly, the similar dependence of diffusion coefficient on PE chain length as shown in Figure 5.6a can also be found for an attractive (sticky) particle in polymer solution but for a very different reason compared with non-sticky particles. [274] Here, the change of scaling relationships is due to the change of the microscopic transport mechanism from the "core-shell" mechanism to the "vehicle" mechanism. [274] Secondly, the MSD of particles with $Q = 40$ and $R = 2\sigma$ is shown in Figure 5.7. In this case, the PE chains also demonstrate Rouse to very weak entanglement dynamics as the chain length increases. However, the dynamics of particles become non-Rouse and remain very slow (the slope of the MSD curve close to 0 in a log-log scale) for a long time before reaching the diffusive regime. This phenomenon indicates a potential absorption-desorption-related mechanism where the stickiness of particles or the electrostatic energy barrier should be considered. Namely, the particles may be trapped due to the Coulomb attraction and eventually become diffusive

when the activation barrier is overcome. As a result, the current theoretical description of the particle dynamics may be too simplified, especially the dependence on the charges per particle Q is underestimated. A more comprehensive study combining theory and simulation is needed to fully reveal the underlying mechanisms.

5.4 Conclusions

In this chapter, we extend the Kremer-Grest model to simulate the salt-free hybrid coacervates formed by spherical charged particles and linear PE chains. Our model gives consistent results for the charges assigned at the center of each particle or evenly distributed at the particle surface. The results are an initial effort to understand the hybrid coacervates from coarse-grained simulations systematically.

For structural properties, our simulation demonstrates the similar dependence of polymer layer density ϕ and layer thickness H on the particle radius R and charges per particle Q as compared with the predictions from the scaling theory. Simulation results can show the change of scaling regimes (scaling exponents for $\phi \sim R^x$ and Q^y as well as $H \sim R^x$ and Q^y) and the shift of the crossover position in terms of R (or Q) as Q (or R) increases. The quantitative agreement between simulation and theory is better for density ϕ compared with thickness H since the relative change of thickness is much smaller than the relative change of density. However, simulation can reveal the non-monotonic dependence of H on R and Q, which is the essential finding from the theory.

To understand how the hybrid coacervates respond to uniform compression, the bulk modulus of the coacervate phase is obtained from our simulation. Simulation results also confirm the scaling relationships between bulk modulus and particle properties (R and Q) predicted in theory. Both simulation and theory show the bulk modulus first independent of R and then decreases with the increase of R. In the meantime, bulk modulus first increases with the increase of Q and eventually becomes independent of Q.

The MSD of particles is measured in simulation for coacervates with different PE chain lengths. For small Q, the particle exhibits dynamics that can be described by the theory of the non-sticky particles in the polymer solution. For example, while the PE chains undergo crossover from Rouse dynamics to entanglement dynamics, the particle smaller than the entanglement tube size remains demonstrating the Rouse-like dynamics. In addition, the diffusion coefficient of particles first decreases as the chain length increases and then becomes independent of the chain length. However, the dynamics become much more complicated as Q increases, where the small particles also experience non-Rouse dynamics. New mechanisms related to the strong Coulomb coupling between particles and PEs and to the resulting sticky (attractive) particles may be needed to describe the dynamics of hybrid coacervates. Thus, the current theoretical treatment for particle dynamics is only applicable to the case of weak Coulomb interactions, as suggested in Ref 56. When Coulomb interactions become strong and the respective activation barriers substantially exceed the thermal energy, this theoretical framework in no more adequate and applicable. More comprehensive studies from theory and simulation are needed in the future to understand further the dynamics and rheology of PE-particle coacervates, especially when particle-PE attractions become strong.

5.5 Supporting Information

5.5.1 Effects of Charge Assignment per Particle on the Coacervate Properties

To test the effects of charge assignment for each particle on the coacervate properties, we use the same model described in Section 5.2 except that the charges are not assigned as a single point charge at the center of the particle. Instead, for each particle, we discretize the spherical surface into n virtual interaction sites by Fibonacci Sphere algorithm [275] where each site has the valence of charges $z_i = +Q/n$. Then we group the spherical particle (with

no charge now) and its n virtual charged sites into one rigid body (the new charged particle). To maintain the same excluded volume interactions, each virtual site has no LJ interactions with other beads, particles, or sites but only Coulomb interactions with other charged beads or sites. In addition, for the new charged particle, we assign $m = 0.5$ to the spherical particle and $m = 0.5/n$ to each virtual charged site so that the new particle has the same mass as the original particle whose charges are at its center.

We perform the same NPT simulations to study the coacervate phase of PE chains and the new charged particles with uniformly distributed surface charges. The structural (polymer layer density and thickness) and dynamic properties (particle center of mass diffusivity) of two hybrid coacervate phases are listed in the Table 5.1 and 5.2. For the two cases, we can see the properties of particles with the charges assigned at the center of the particle ($n = 1$) are the same within errors compared with the properties of new particles with various degrees of surface charge smearing ($n = 64, 128, 256$).

charge distribution	$\phi[\sigma^{-3}]$	$H[\sigma]$	$D_p[\sigma^2\tau_{LJ}^{-1}] \times [10^3\tau_{LJ}]$
$n = 1$	0.267 ± 0.001	2.18 ± 0.01	3.4 ± 0.2
$n = 64$	0.267 ± 0.001	2.18 ± 0.01	3.3 ± 0.2
$n = 128$	0.267 ± 0.001	2.17 ± 0.01	3.5 ± 0.2
$n = 256$	0.268 ± 0.001	2.17 ± 0.01	3.5 ± 0.2

Table 5.1: Structural and dynamic properties of hybrid coacervate phase for different particle charge distribution. $n = 1$ donates charges at the center of the particle. $n = 64, 128, 256$ represents different degrees of charge smearing for uniformly distributed surface charges. ϕ is polymer layer density, H is polymer layer thickness, and D_p is diffusion coefficient of particle center of mass diffusion. The simulation parameters are $N = 120, f = 0.2$ for PE chains, $R = 2\sigma, Q = 24$ for charged particles, and $l_B = \sigma$.

We can further compare their internal structures by calculating the radius distribution functions between different species in the coacervate phase. From the Figure 5.10 in Section 5.5.3, we can also see the curves for different degrees of surface charge smearing ($n = 64, 128, 256$), and charges at the center of the particle overlap with each other perfectly.

Finally, we also plotted the mean squared displacement of charged particles' center of

charge distribution	$\phi[\sigma^{-3}]$	$H[\sigma]$	$D_p[\sigma^2\tau_{LJ}^{-1}] \times [10^5\tau_{LJ}]$
$n = 1$	0.411 ± 0.001	2.45 ± 0.01	2.0 ± 0.1
$n = 128$	0.411 ± 0.001	2.46 ± 0.01	1.9 ± 0.1
$n = 256$	0.410 ± 0.001	2.45 ± 0.01	2.0 ± 0.1

Table 5.2: Structural and dynamic properties of hybrid coacervate phase for different particle charge distributions. $n = 1$ donates charges at the center of the particle. $n = 128, 256$ represent different degrees of charge smearing for uniformly distributed surface charges. ϕ is polymer layer density, H is polymer layer thickness, and D_p is diffusion coefficient of particle center of mass diffusion. The simulation parameters are $N = 200, f = 0.2$ for PE chains, $R = 2\sigma, Q = 40$ for charged particles, and $l_B = \sigma$.

mass in Figure 5.8 to reveal both the short and the long time scale diffusion behavior of original and new charged particles. From the curves in Figure 5.8, we can see that the uniform distribution of charges at the particle surface does not change either the short or the long time scale diffusion of charged particles compared with assigning the charges at the center of the particle.

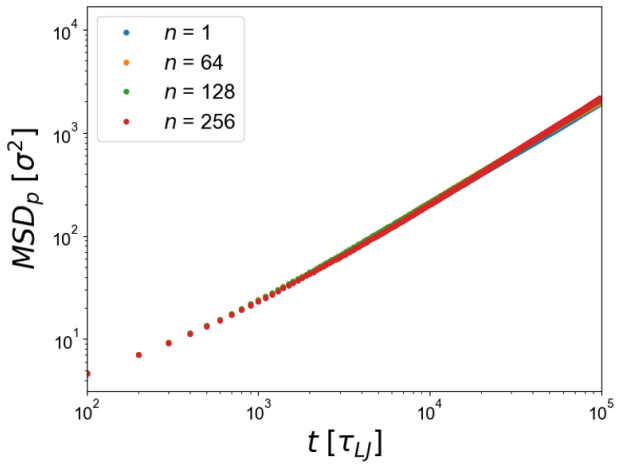

Figure 5.8: Mean squared displacement of the charged particles' center of mass (MSD_p) as a function of simulation time in log-log scale for different particle charge distributions. $n = 1$ donates charges at the center of the particle. $n = 64, 128, 256$ represent different degrees of charge smearing for uniformly distributed surface charges. The simulation parameters are $N = 120, f = 0.2$ for PE chains, $R = 1.5\sigma, Q = 24$ for charged particles, and $l_B = \sigma$.

5.5.2 Absorption Layer Density Distribution

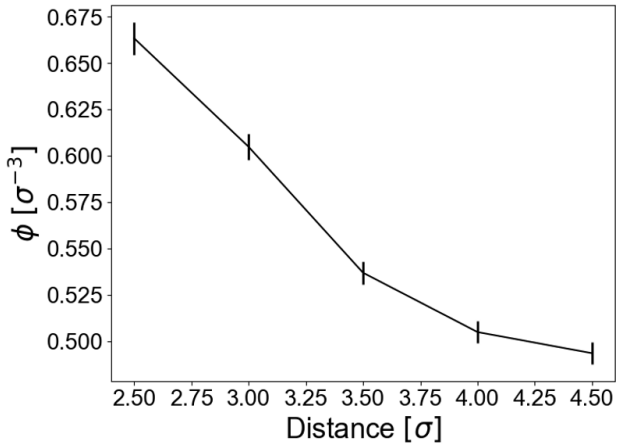

Figure 5.9: The layer density ϕ as a function of distance away from the particle center. The simulation parameters are $N = 200, f = 0.2$ for PE chains, $R = 1.5\sigma, Q = 40$ for charged particles, and $l_B = \sigma$.

5.5.3 Radius Distribution Function of Charged Particles and Ionic Monomers

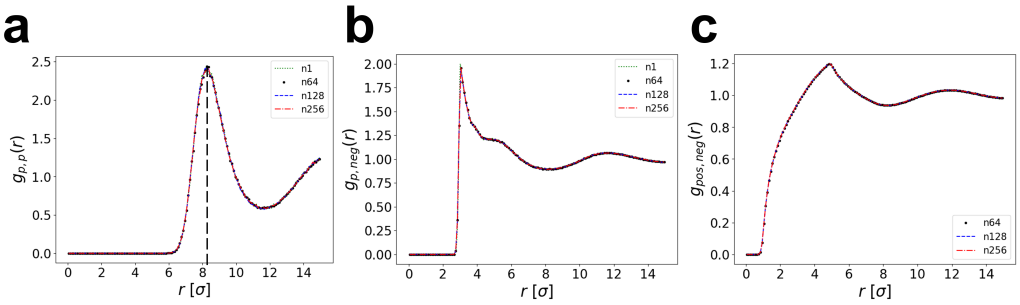

Figure 5.10: a) Dependence of radius distribution function between different particle center of masses $g_{p,p}(r)$ on separation distance r for different ways of charge assignment. Black straight dash line marks to the first peak location. b) Dependence of radius distribution function between particle center of mass and negatively charged monomer $g_{p,neg}(r)$ on separation distance r for different ways of charge assignment. c) Dependence of radius distribution function between positively charged cite on the particle surface and negatively charged monomer $g_{pos,neg}(r)$ on separation distance r for different ways of charge assignment. $n1$ represents charges assigned at the center of the particle. $n64, n128, n256$ represent charges evenly assigned at the particle's surface with $64, 128, 256$ sites, respectively (see Section 5.5.1 for details). The simulation parameters are $N = 120, f = 0.2$ for PE chains, $R = 2\sigma, Q = 24$ for charged particles, and $l_B = \sigma$.

5.5.4 Snapshots of Hybrid Coacervate Phases

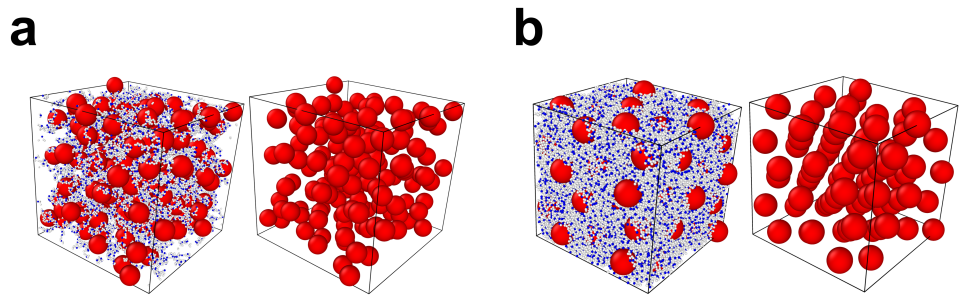

Figure 5.11: a) Snapshots for hybrid coacervate phase for small charges Q per particle. The whole coacervate phase is shown on the left, while only the charged particles are shown on the right. The simulation parameters are $N = 120, f = 0.2$ for PE chains, $R = 5\sigma, Q = 24$ for charged particles, and $l_B = \sigma$. b) Snapshots for hybrid coacervate phase for large charges Q per particle. The whole coacervate phase is shown on the left, while only the charged particles are shown on the right. The simulation parameters are $N = 750, f = 0.2$ for PE chains, $R = 5\sigma, Q = 150$ for charged particles, and $l_B = \sigma$. Red: positively charged; Blue: negatively charged; white: neutral.

5.5.5 *Bulk Modulus Calculation*

The bulk modulus (B) or osmotic modulus of the hybrid coacervate phase is calculated in the following way. [271] First, an external pressure P is applied to compress the coacervate phase along three dimensions uniformly, and the corresponding volume V is measured. Then we repeat this process with different P values and obtain the relationship between P and the specific volume $V_{sp} = V/N_{total}$, where N_{total} is the total number of beads (monomers and particles) in the system since we assume all beads have the same unit mass. To maintain the linear relationship assumption, the volume change is within 5%. [271] Finally, the bulk modulus can be obtained from the slope of the fitted line for P vs the natural logarithm of V_{sp} ($\ln V_{sp}$), where $B = -\frac{dP}{d(lnV_{sp})}$. One example of the fitting results for PE chain length $N = 120$, particle radius $R = 1.5\sigma$, and charges per particle $Q = 24$ is shown in Figure 5.12.

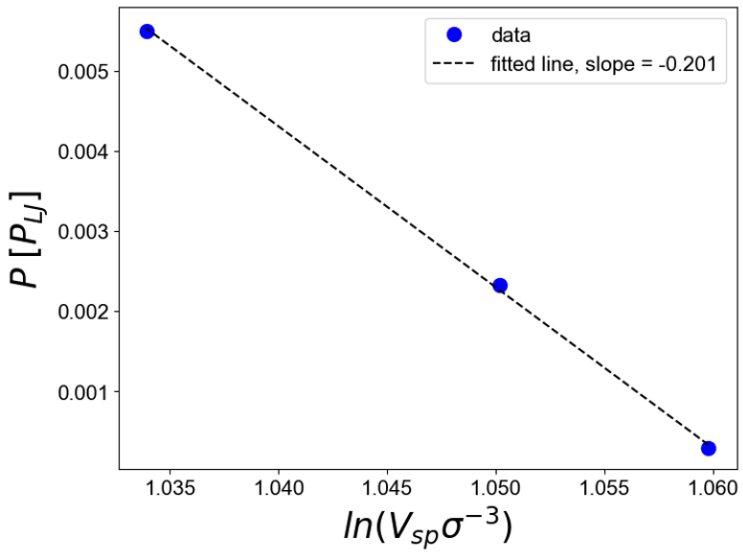

Figure 5.12: The relationship between applied external pressures P and the natural logarithm of specific volume lnV_{sp}. Simulation data are shown in blue points. A linear function fits data, and the legend shows the slope. The simulation parameters are $N = 120, f = 0.2$ for PE chains, $R = 1.5\sigma, Q = 24$ for charged particles, and $l_B = \sigma$.

5.5.6 Scaling Relationships between Particle Diffusion Coefficient and Particle Radius

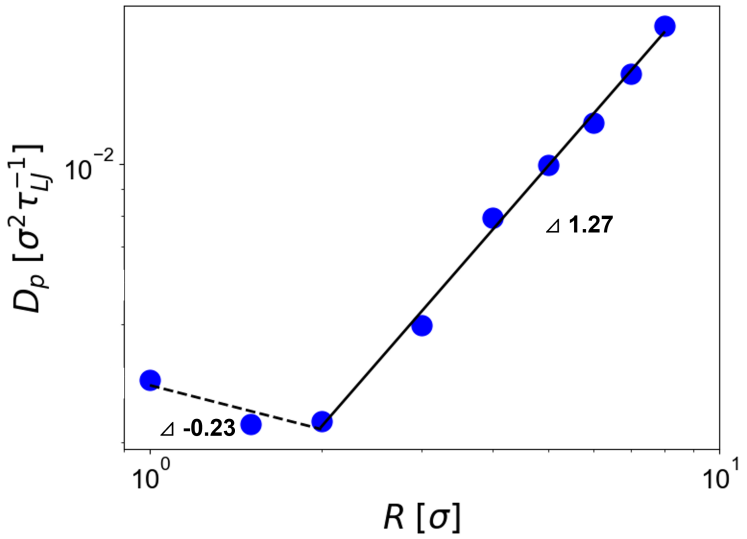

Figure 5.13: The relationship between the diffusivity of particles D_p and particle radius R. Straight lines are fitted from simulation data. The errors are estimated by dividing the particles into five groups and calculating the standard deviation of diffusivity of each group. The errors are within the size of each data point. The simulation parameters are $N = 120, f = 0.2$ for PE chains, $Q = 24$ for charged particles, and $l_B = \sigma$.

CHAPTER 6

CONCLUSIONS AND FUTURE WORK

In this dissertation, I have conducted a comprehensive study on the phase behavior of complex coacervates using coarse-grained simulations. Our results reveal in detail how the charge fraction, charge sequence, chain stiffness, and coacervate compositions affect the properties of the corresponding coacervate phase, as well as demonstrate the capabilities of simulations as a valuable tool to verify theoretical predictions and provide helpful guidance for experimental studies. In addition, the models and methods presented in this work can be easily extended to study other coacervate systems with different chain architectures, shapes of charged species, and types and strengths of interactions (polymer-polymer, polymer-salt, and salt-salt interactions).

Based on the current findings shown in this work, many future directions can be further pursued. In Chapter 2, we explore the dependence of polymer volume fraction in the coacervate phase on the charge fraction of PE chains. In the future, beyond volume fraction, we can further study the dependence of other quantities, such as interfacial tension and PE chain relaxation time, on the charge fraction. To do so, we can follow this work [270], where both coacervate and supernatant phases are simulated in the simulation with the interfaces between them. In this chapter, we also show that the salt partitioning is PE chain chemistry dependent via simulations. However, our simulations cannot reproduce some more complicated trend related to salt partitioning in experiments. In order to further understand them, we need to use a more systematic approach to parameterize our model based on experimental conditions and introduce explicit solvent to the model. In addition, we only consider the linear PE chains in this chapter. We can also consider other chain architectures like ring and branch and compare how the scaling behaviors differ among different chain architectures.

In Chapter 3, we study the effects of monomer sequence on the phase behavior of complex coacervates. The higher the blockiness of the sequence, the denser the coacervate phase.

At very high sequence blockiness, there is a tendency for the coacervate phase to become inhomogeneous with the formation of domains of charged and neutral monomers. In the future, understanding how the interfacial tension and dynamic properties like chain diffusion coefficient and viscosity change upon this homogeneous to inhomogeneous transition is of interest. This understanding could provide valuable information about sequence effects on coacervate dynamics and rheology.

In Chapter 4, we explore the isotropic-to-nematic transition inside the coacervate phase triggered by the increase of chain stiffness. In this study, we only consider the isotropic and nematic phases. It is natural to extend our study to the smectic phase and identify the conditions for the nematic-to-smectic transition. In this chapter, we also investigate the orientation of interfacial chains at the interface of supernatant and coacervate phases. In the future, a similar study can be conducted to understand the chain orientations at the interface between the coexisting isotropic and nematic coacervate phases.

In Chapter 5, we investigate the properties of hybrid coacervates where one of the components changes from liner PE chains to charged spheres. The natural extension to this study would be to understand the influence of surface charge distributions on the properties of coacervate phases (in this work, we only consider the charge at the center of the sphere or evenly distributed on the surface). Another direction would be exploring the effects of particle shapes by replacing the spherical particles with cylindrical particles (different aspect ratios) or polygons.

Beyond the explorational study done in this dissertation, a more challenging task is the reversed problems of designing the target materials based on certain requirements. Namely, finding the parameters of PE chains that produce coacervates with desired properties. Machine learning (ML) methods are the promising tools in this area. For example, ML models have been developed to find sequences corresponding to the target self-assembly structures. [276, 277] In the future, by combining the understanding of coacervates and ML tech-

niques, our abilities to predict and design coacervation-based materials will be significantly increased.

REFERENCES

[1] Alexander Stukowski. Visualization and analysis of atomistic simulation data with ovito–the open visualization tool. *Modelling and Simulation in Materials Science and Engineering*, 18(1):015012, 2009.

[2] Charles E Sing and Sarah L Perry. Recent progress in the science of complex coacervation. *Soft Matter*, 16(12):2885–2914, 2020.

[3] Angelika E Neitzel, Yan N Fang, Boyuan Yu, Artem M Rumyantsev, Juan J de Pablo, and Matthew V Tirrell. Polyelectrolyte complex coacervation across a broad range of charge densities. *Macromolecules*, 2021.

[4] Boyuan Yu, Artem M Rumyantsev, Nicholas E Jackson, Heyi Liang, Jeffrey M Ting, Siqi Meng, Matthew V Tirrell, and Juan J de Pablo. Complex coacervation of statistical polyelectrolytes: role of monomer sequences and formation of inhomogeneous coacervates. *Mol. Syst. Des. Eng.*, 6(10):790–804, 2021.

[5] Boyuan Yu, Heyi Liang, Artem M Rumyantsev, and Juan J de Pablo. Isotropic-to-nematic transition in salt-free polyelectrolyte coacervates from coarse-grained simulations. *Macromolecules*, 2022.

[6] Artem M Rumyantsev, Oleg Borisov, and Juan J de Pablo. Structure and dynamics of hybrid colloid-polyelectrolyte coacervates. *Macromolecules*, 2022.

[7] Boyuan Yu, Phillip M Rauscher, Nicholas E Jackson, Artem M Rumyantsev, and Juan J de Pablo. Crossover from rouse to reptation dynamics in salt-free polyelectrolyte complex coacervates. *ACS Macro Letters*, 9(9):1318–1324, 2020.

[8] Boyuan Yu, Artem Rumyantsev, Heyi Liang, and Juan de Pablo. Structure and dynamics of hybrid colloid-polyelectrolyte coacervates from coarse-grained simulations. 2022.

[9] Arthur Veis. A review of the early development of the thermodynamics of the complex coacervation phase separation. *Advances in colloid and interface science*, 167(1-2):2–11, 2011.

[10] Samanvaya Srivastava and Matthew V Tirrell. Polyelectrolyte complexation. *Advances in chemical physics*, 161:499–544, 2016.

[11] Charles E Sing and Sarah L Perry. Recent progress in the science of complex coacervation. *Soft Matter*, 16(12):2885–2914, 2020.

[12] Artem M Rumyantsev, Nicholas E Jackson, and Juan J De Pablo. Polyelectrolyte complex coacervates: Recent developments and new frontiers. *Annu. Rev. Condens. Matter Phys*, 12(1):155–176, 2021.

[13] Jasper Van der Gucht, Evan Spruijt, Marc Lemmers, and Martien A Cohen Stuart. Polyelectrolyte complexes: Bulk phases and colloidal systems. *Journal of colloid and interface science*, 361(2):407–422, 2011.

[14] Qifeng Wang and Joseph B Schlenoff. The polyelectrolyte complex/coacervate continuum. *Macromolecules*, 47(9):3108–3116, 2014.

[15] Clifford P Brangwynne, Peter Tompa, and Rohit V Pappu. Polymer physics of intracellular phase transitions. *Nature Physics*, 11(11):899–904, 2015.

[16] Joshua A Riback, Lian Zhu, Mylene C Ferrolino, Michele Tolbert, Diana M Mitrea, David W Sanders, Ming-Tzo Wei, Richard W Kriwacki, and Clifford P Brangwynne. Composition-dependent thermodynamics of intracellular phase separation. *Nature*, 581(7807):209–214, 2020.

[17] Jarrett Smith, Deepika Calidas, Helen Schmidt, Tu Lu, Dominique Rasoloson, and Geraldine Seydoux. Spatial patterning of p granules by rna-induced phase separation of the intrinsically-disordered protein meg-3. *Elife*, 5, 2016.

[18] Alexander Baer, Nils Horbelt, Marlies Nijemeisland, Santiago J Garcia, Peter Fratzl, Stephan Schmidt, Georg Mayer, and Matthew J Harrington. Shear-induced β-crystallite unfolding in condensed phase nanodroplets promotes fiber formation in a biological adhesive. *ACS nano*, 13(5):4992–5001, 2019.

[19] Russell J Stewart, Todd C Ransom, and Vladimir Hlady. Natural underwater adhesives. *Journal of Polymer Science Part B: Polymer Physics*, 49(11):757–771, 2011.

[20] Hadi M Fares, Alexander E Marras, Jeffrey M Ting, Matthew V Tirrell, and Christine D Keating. Impact of wet-dry cycling on the phase behavior and compartmentalization properties of complex coacervates. *Nature communications*, 11(1):1–13, 2020.

[21] Allie C Obermeyer, Carolyn E Mills, Xue-Hui Dong, Romeo J Flores, and Bradley D Olsen. Complex coacervation of supercharged proteins with polyelectrolytes. *Soft Matter*, 12(15):3570–3581, 2016.

[22] Whitney C Blocher and Sarah L Perry. Complex coacervate-based materials for biomedicine. *Wiley Interdisciplinary Reviews: Nanomedicine and Nanobiotechnology*, 9(4):e1442, 2017.

[23] Daniel V Krogstad, Nathaniel A Lynd, Soo-Hyung Choi, Jason M Spruell, Craig J Hawker, Edward J Kramer, and Matthew V Tirrell. Effects of polymer and salt concentration on the structure and properties of triblock copolymer coacervate hydrogels. *Macromolecules*, 46(4):1512–1518, 2013.

[24] Samanvaya Srivastava, Marat Andreev, Adam E Levi, David J Goldfeld, Jun Mao, William T Heller, Vivek M Prabhu, Juan J De Pablo, and Matthew V Tirrell. Gel phase formation in dilute triblock copolyelectrolyte complexes. *Nature communications*, 8(1):1–9, 2017.

[25] Katie A Black, Dimitrios Priftis, Sarah L Perry, Jeremy Yip, William Y Byun, and Matthew Tirrell. Protein encapsulation via polypeptide complex coacervation. *ACS Macro Letters*, 3(10):1088–1091, 2014.

[26] Patrick M McCall, Samanvaya Srivastava, Sarah L Perry, David R Kovar, Margaret L Gardel, and Matthew V Tirrell. Partitioning and enhanced self-assembly of actin in polypeptide coacervates. *Biophysical journal*, 114(7):1636–1645, 2018.

[27] Qiang Zhao, Quanfu F An, Yanli Ji, Jinwen Qian, and Congjie Gao. Polyelectrolyte complex membranes for pervaporation, nanofiltration and fuel cell applications. *Journal of membrane science*, 379(1-2):19–45, 2011.

[28] GT Zhumadilova, AD Gazizov, LA Bimendina, and SE Kudaibergenov. Properties of polyelectrolyte complex membranes based on some weak polyelectrolytes. *Polymer*, 42(7):2985–2989, 2001.

[29] B Smitha, S Sridhar, and AA Khan. Polyelectrolyte complexes of chitosan and poly (acrylic acid) as proton exchange membranes for fuel cells. *Macromolecules*, 37(6):2233–2239, 2004.

[30] Xiangxi Meng, Jessica D Schiffman, and Sarah L Perry. Electrospinning cargo-containing polyelectrolyte complex fibers: Correlating molecular interactions to complex coacervate phase behavior and fiber formation. *Macromolecules*, 51(21):8821–8832, 2018.

[31] Xiangxi Meng, Sarah L Perry, and Jessica D Schiffman. Complex coacervation: Chemically stable fibers electrospun from aqueous polyelectrolyte solutions. *ACS Macro Letters*, 6(5):505–511, 2017.

[32] Pierre Schaaf and Joseph B Schlenoff. Saloplastics: Processing compact polyelectrolyte complexes. *Advanced Materials*, 27(15):2420–2432, 2015.

[33] Mo Yang, Jianbing Shi, and Joseph B Schlenoff. Control of dynamics in polyelectrolyte complexes by temperature and salt. *Macromolecules*, 52(5):1930–1941, 2019.

[34] Evan Spruijt, Adrie H Westphal, Jan Willem Borst, Martien A Cohen Stuart, and Jasper van der Gucht. Binodal compositions of polyelectrolyte complexes. *Macromolecules*, 43(15):6476–6484, 2010.

[35] Lu Li, Samanvaya Srivastava, Marat Andreev, Amanda B Marciel, Juan J de Pablo, and Matthew V Tirrell. Phase behavior and salt partitioning in polyelectrolyte complex coacervates. *Macromolecules*, 51(8):2988–2995, 2018.

[36] William M Aumiller and Christine D Keating. Phosphorylation-mediated rna/peptide complex coacervation as a model for intracellular liquid organelles. *Nature chemistry*, 8(2):129–137, 2016.

[37] Sara Tabandeh and Lorraine Leon. Engineering peptide-based polyelectrolyte complexes with increased hydrophobicity. *Molecules*, 24(5):868, 2019.

[38] Jeffrey R Vieregg, Michael Lueckheide, Amanda B Marciel, Lorraine Leon, Alex J Bologna, Josean Reyes Rivera, and Matthew V Tirrell. Oligonucleotide–peptide complexes: phase control by hybridization. *Journal of the American Chemical Society*, 140(5):1632–1638, 2018.

[39] Li-Wei Chang, Tyler K Lytle, Mithun Radhakrishna, Jason J Madinya, Jon Vélez, Charles E Sing, and Sarah L Perry. Sequence and entropy-based control of complex coacervates. *Nat. Commun.*, 8(1):1273, 2017.

[40] Tyler K Lytle, Li-Wei Chang, Natalia Markiewicz, Sarah L Perry, and Charles E Sing. Designing electrostatic interactions via polyelectrolyte monomer sequence. *ACS central science*, 5(4):709–718, 2019.

[41] Artem M Rumyantsev, Nicholas E Jackson, Boyuan Yu, Jeffrey M Ting, Wei Chen, Matthew V Tirrell, and Juan J de Pablo. Controlling complex coacervation via random polyelectrolyte sequences. *ACS Macro Lett.*, 8(10):1296–1302, 2019.

[42] Junzhe Lou, Sean Friedowitz, Jian Qin, and Yan Xia. Tunable coacervation of well-defined homologous polyanions and polycations by local polarity. *ACS central science*, 5(3):549–557, 2019.

[43] Lu Li, Artem M Rumyantsev, Samanvaya Srivastava, Siqi Meng, Juan J de Pablo, and Matthew V Tirrell. Effect of solvent quality on the phase behavior of polyelectrolyte complexes. *Macromolecules*, 54(1):105–114, 2020.

[44] Kazi Sadman, Qifeng Wang, Yaoyao Chen, Bavand Keshavarz, Zhang Jiang, and Kenneth R Shull. Influence of hydrophobicity on polyelectrolyte complexation. *Macromolecules*, 50(23):9417–9426, 2017.

[45] Sarah L Perry, Lorraine Leon, Kyle Q Hoffmann, Matthew J Kade, Dimitrios Priftis, Katie A Black, Derek Wong, Ryan A Klein, Charles F Pierce, Khatcher O Margossian, et al. Chirality-selected phase behaviour in ionic polypeptide complexes. *Nature Communications*, 6(1):1–8, 2015.

[46] Brandon M. Johnston, Cameron W. Johnston, Rachel A. Letteri, Tyler K. Lytle, Charles E. Sing, Todd Emrick, and Sarah L. Perry. The effect of comb architecture on complex coacervation. *Organic & Biomolecular Chemistry*, 15(36):7630–7642, 2017.

[47] Mo Yang, Zachary A. Digby, and Joseph B. Schlenoff. Precision doping of polyelectrolyte complexes: Insight on the role of ions. *Macromolecules*, 53(13):5465–5474, 2020.

[48] Vaqar M. S. Syed and Samanvaya Srivastava. Time–Ionic Strength Superposition: A Unified Description of Chain Relaxation Dynamics in Polyelectrolyte Complexes. *ACS Macro Letters*, 9(7):1067–1073, July 2020.

[49] Siqi Meng, Yueming Liu, Jihyeon Yeo, Jeffrey M Ting, and Matthew V Tirrell. Effect of mixed solvents on polyelectrolyte complexes with salt. *Colloid and Polymer Science*, 298(7):887–894, 2020.

[50] F Weinbreck, R De Vries, P Schrooyen, and CG De Kruif. Complex coacervation of whey proteins and gum arabic. *Biomacromolecules*, 4(2):293–303, 2003.

[51] Samim Ali, Markus Bleuel, and Vivek M Prabhu. Lower critical solution temperature in polyelectrolyte complex coacervates. *ACS macro letters*, 8(3):289–293, 2019.

[52] H. Bungenberg-De Jong and H. Kruyt. *Proc. Sect. Sci., K. Ned. Akad. Wetenschappen*, 32:849–856, 1929.

[53] J Th G Overbeek and MJ Voorn. Phase separation in polyelectrolyte solutions. theory of complex coacervation. *Journal of Cellular and Comparative Physiology*, 49(S1):7–26, 1957.

[54] Angelika E Neitzel, Guilhem X De Hoe, and Matthew V Tirrell. Expanding the structural diversity of polyelectrolyte complexes and polyzwitterions. *Current Opinion in Solid State and Materials Science*, 25(2):100897, 2021.

[55] NP Shusharina, EB Zhulina, AV Dobrynin, and M Rubinstein. Scaling theory of diblock polyampholyte solutions. *Macromolecules*, 38(21):8870–8881, 2005.

[56] Artem M Rumyantsev, Ekaterina B Zhulina, and Oleg V Borisov. Complex coacervate of weakly charged polyelectrolytes: Diagram of states. *Macromolecules*, 51(10):3788–3801, 2018.

[57] M Rubinstein, Q Liao, and S Panyukov. Structure of liquid coacervates formed by oppositely charged polyelectrolytes. *Macromolecules*, 51(10):9572–9588, 2018.

[58] Scott PO Danielsen, Sergey Panyukov, and Michael Rubinstein. Ion pairing and the structure of gel coacervates. *Macromolecules*, 53(21):9420–9442, 2020.

[59] Jun Huang, Frances J Morin, and Jennifer E Laaser. Charge-density-dominated phase behavior and viscoelasticity of polyelectrolyte complex coacervates. *Macromolecules*, 52(13):4957–4967, 2019.

[60] Kurt Kremer and Gary S Grest. Dynamics of entangled linear polymer melts: A molecular-dynamics simulation. *J. Chem. Phys.*, 92(8):5057–5086, 1990.

[61] Steve Plimpton and Bruce Hendrickson. Parallel molecular dynamics algorithms for simulation of molecular systems. In *ACS Symposium Series*, volume 592, pages 114–114. Citeseer, 1995.

[62] William W Graessley, Ryan C Hayward, and Gary S Grest. Excluded-volume effects in polymer solutions. 2. comparison of experimental results with numerical simulation data. *Macromolecules*, 32(10):3510–3517, 1999.

[63] Douglas J Grzetic, Kris T Delaney, and Glenn H Fredrickson. The effective χ parameter in polarizable polymeric systems: One-loop perturbation theory and field-theoretic simulations. *The Journal of Chemical Physics*, 148(20):204903, 2018.

[64] Xian Kong, Kevin Jia-Yu Hou, and Jian Qin. Weakening of solvation-induced ordering by composition fluctuation in salt-doped block polymers. *ACS Macro Letters*, 10(5):545–550, 2021.

[65] Kuan-Hsuan Shen, Mengdi Fan, and Lisa M Hall. Molecular dynamics simulations of ion-containing polymers using generic coarse-grained models. *Macromolecules*, 54(5):2031–2052, 2021.

[66] Alexey A Gavrilov. Dissipative particle dynamics for systems with polar species: Interactions in dielectric media. *The Journal of Chemical Physics*, 152(16):164101, 2020.

[67] Dimitris G Mintis and Vlasis G Mavrantzas. Phase boundary and salt partitioning in coacervate complexes formed between poly (acrylic acid) and poly (n, n-dimethylaminoethyl methacrylate) from detailed atomistic simulations combined with free energy perturbation and thermodynamic integration calculations. *Macromolecules*, 53(18):7618–7634, 2020.

[68] Glenn H Fredrickson, Scott T Milner, and Ludwik Leibler. Multicritical phenomena and microphase ordering in random block copolymers melts. *Macromolecules*, 25(23):6341–6354, 1992.

[69] Anton AA Smith, Aaron Hall, Vincent Wu, and Ting Xu. Practical prediction of heteropolymer composition and drift. *ACS Macro Letters*, 8(1):36–40, 2018.

[70] Vince-Wu. Vince-wu/compositionaldrift: Simulates polymer chain growth based on the mayo lewis equation and the monte carlo method.

[71] Thomas E Gartner III, Thomas H Epps III, and Arthi Jayaraman. Leveraging gibbs ensemble molecular dynamics and hybrid monte carlo/molecular dynamics for efficient study of phase equilibria. *J. Chem. Theory Comput.*, 12(11):5501–5510, 2016.

[72] Mithun Radhakrishna, Kush Basu, Yalin Liu, Rasmia Shamsi, Sarah L Perry, and Charles E Sing. Molecular connectivity and correlation effects on polymer coacervation. *Macromolecules*, 50(7):3030–3037, 2017.

[73] Athanassios Z Panagiotopoulos, N Quirke, M Stapleton, and DJ Tildesley. Phase equilibria by simulation in the gibbs ensemble: alternative derivation, generalization and application to mixture and membrane equilibria. *Mol. Phys.*, 63(4):527–545, 1988.

[74] Steve Plimpton. Fast parallel algorithms for short-range molecular dynamics. *Journal of computational physics*, 117(1):1–19, 1995.

[75] Angelika E Neitzel, Yan N Fang, Boyuan Yu, Artem M Rumyantsev, Juan J de Pablo, and Matthew V Tirrell. Polyelectrolyte complex coacervation across a broad range of charge densities. *Macromolecules*, 54(14):6878–6890, 2021.

[76] Sarah L Perry and Charles E Sing. PRISM-based theory of complex coacervation: Excluded volume versus chain correlation. *Macromolecules*, 48(14):5040–5053, 2015.

[77] Pengfei Zhang, Kevin Shen, Nayef M Alsaifi, and Zhen-Gang Wang. Salt partitioning in complex coacervation of symmetric polyelectrolytes. *Macromolecules*, 51(15):5586–5593, 2018.

[78] Zuowei Wang and Michael Rubinstein. Regimes of conformational transitions of a diblock polyampholyte. *Macromolecules*, 39(17):5897–5912, 2006.

[79] Joseph B Schlenoff, Mo Yang, Zachary A Digby, and Qifeng Wang. Ion content of polyelectrolyte complex coacervates and the donnan equilibrium. *Macromolecules*, 52(23):9149–9159, 2019.

[80] Mohsen Ghasemi, Sean Friedowitz, and Ronald G Larson. Analysis of partitioning of salt through doping of polyelectrolyte complex coacervates. *Macromolecules*, 53(16):6928–6945, 2020.

[81] Jean-Francois Lutz, Jean-Marie Lehn, EW Meijer, and Krzysztof Matyjaszewski. From precision polymers to complex materials and systems. *Nature Rev. Mater.*, 1(5):1–14, 2016.

[82] Anastasia L Patterson, Scott PO Danielsen, Beihang Yu, Emily C Davidson, Glenn H Fredrickson, and Rachel A Segalman. Sequence effects on block copolymer self-assembly through tuning chain conformation and segregation strength utilizing sequence-defined polypeptoids. *Macromolecules*, 52(3):1277–1286, 2019.

[83] Rahul K Das and Rohit V Pappu. Conformations of intrinsically disordered proteins are influenced by linear sequence distributions of oppositely charged residues. *Proc. Natl. Acad. Sci. USA*, 110(33):13392–13397, 2013.

[84] Joseph R Simon, Nick J Carroll, Michael Rubinstein, Ashutosh Chilkoti, and Gabriel P López. Programming molecular self-assembly of intrinsically disordered proteins containing sequences of low complexity. *Nature Chem.*, 9(6):509, 2017.

[85] T. J. Nott, E. Petsalaki, P. Farber, D. Jervis, E. Fussner, A. Plochowietz, T. D. Craggs, D. P. Bazett-Jones, T. Pawson, J. D. Forman-Kay, and A. J. Baldwin. Phase transition of a disordered nuage protein generates environmentally responsive membraneless organelles. *Mol. Cell*, 57(5):936–947, 2015.

[86] Sarah L Perry and Charles E Sing. 100th anniversary of macromolecular science viewpoint: Opportunities in the physics of sequence-defined polymers. *ACS Macro Lett.*, 9(2):216–225, 2020.

[87] Li-Wei Chang, Tyler K Lytle, Mithun Radhakrishna, Jason J Madinya, Jon Vélez, Charles E Sing, and Sarah L Perry. Sequence and entropy-based control of complex coacervates. *Nature Commun.*, 8(1):1–8, 2017.

[88] William G Levine, Youngmi Seo, Jonathan R Brown, and Lisa M Hall. Effect of sequence dispersity on morphology of tapered diblock copolymers from molecular dynamics simulations. *The Journal of chemical physics*, 145(23):234907, 2016.

[89] Shifan Mao, Quinn MacPherson, Jian Qin, and Andrew J Spakowitz. Field-theoretic simulations of random copolymers with structural rigidity. *Soft Matter*, 13(15):2760–2772, 2017.

[90] Scott PO Danielsen, James McCarty, Joan-Emma Shea, Kris T Delaney, and Glenn H Fredrickson. Molecular design of self-coacervation phenomena in block polyampholytes. *Proc. Natl. Acad. Sci. USA*, 116(17):8224–8232, 2019.

[91] Brian Panganiban, Baofu Qiao, Tao Jiang, Christopher DelRe, Mona M Obadia, Trung Dac Nguyen, Anton AA Smith, Aaron Hall, Izaac Sit, Marquise G Crosby, et al. Random heteropolymers preserve protein function in foreign environments. *Science*, 359(6381):1239–1243, 2018.

[92] Tyler K Lytle, Li-Wei Chang, Natalia Markiewicz, Sarah L Perry, and Charles E Sing. Designing electrostatic interactions via polyelectrolyte monomer sequence. *ACS Central Sci.*, 5(4):709–718, 2019.

[93] Yi-Hsuan Lin, Julie D Forman-Kay, and Hue Sun Chan. Sequence-specific polyampholyte phase separation in membraneless organelles. *Phys. Rev. Lett.*, 117(17):178101, 2016.

[94] Yi-Hsuan Lin, Jianhui Song, Julie D Forman-Kay, and Hue Sun Chan. Random-phase-approximation theory for sequence-dependent, biologically functional liquid-liquid phase separation of intrinsically disordered proteins. *J. Mol. Liq.*, 228:176–193, 2017.

[95] James McCarty, Kris T Delaney, Scott PO Danielsen, Glenn H Fredrickson, and Joan-Emma Shea. Complete phase diagram for liquid-liquid phase separation of intrinsically disordered proteins. *J. Phys. Chem. Lett.*, 10(8):1644–1652, 2019.

[96] Artem M Rumyantsev, Nicholas E Jackson, Albert Johner, and Juan J de Pablo. Scaling theory of neutral sequence-specific polyampholytes. *Macromolecules*, 54:3232–3246, 2021.

[97] Angelika E. Neitzel, G. X. De Hoe, and Matthew V Tirrell. Expanding the structural diversity of polyelectrolyte complexes and polyzwitterions. *Curr. Opin. Solid State Mater. Sci.*, 25:100897, 2021.

[98] J. Dinic, A. B. Marciel, and M. V. Tirrell. Polyampholyte physics: Liquid-liquid phase separation and biological condensates. *Curr. Opin. Colloid Interface Sci.*, 54:101457, 2021.

[99] Artem M Rumyantsev, Nicholas E Jackson, Boyuan Yu, Jeffrey M Ting, Wei Chen, Matthew V Tirrell, and Juan J de Pablo. Controlling complex coacervation via random polyelectrolyte sequences. *ACS Macro Lett.*, 8(10):1296–1302, 2019.

[100] S. Brusseau, J. Belleney, S. Magnet, L. Couvreur, and B. Charleux. Methacrylic acid with sodium 4-styrene sulfonate: Towards new water-soluble macroalkoxyamines for the synthesis of amphiphilic block copolymers and nanoparticles. *Polym. Chem.*, 1:720–729, 2010.

[101] J. Wang, C. Waltmann, H. Umana-Kossio, M. Olvera de la Cruz, and J. M. Torkelson. Heterogeneous charged complexes of random copolymers for the segregation of organic molecules. *ACS Cent. Sci.*, 7:882–891, 2021.

[102] I. Dimitrov, K. Jankova, and S. Hvilsted. Synthesis of polystyrene-based random copolymers with balanced number of basic or acidic functional groups: Polystyrene-based random copolymers. *J. Polym. Sci. A Polym. Chem.*, 48:2044–2052, 2010.

[103] Jeffrey M Ting, Tushar S Navale, Frank S Bates, and Theresa M Reineke. Precise compositional control and systematic preparation of multimonomeric statistical copolymers. *ACS Macro Lett.*, 2(9):770–774, 2013.

[104] Glenn H Fredrickson and Scott T Milner. Thermodynamics of random copolymer melts. *Phys. Rev. Lett.*, 67(7):835, 1991.

[105] Glenn H Fredrickson, Scott T Milner, and Ludwik Leibler. Multicritical phenomena and microphase ordering in random block copolymers melts. *Macromolecules*, 25(23):6341–6354, 1992.

[106] A Johner and JF Joanny. Translocation of polyampholytes and intrinsically disordered proteins*. *Eur. Phys. J. E*, 41:78, 2018.

[107] J Houdayer and M Müller. Deviations from the mean-field predictions for the phase behaviour of random copolymers melts. *EPL*, 58(5):660, 2002.

[108] J Houdayer and M Müller. Phase diagram of random copolymer melts: a computer simulation study. *Macromolecules*, 37(11):4283–4295, 2004.

[109] M. Lemmers, E. Spruijt, L. Beun, R. Fokkink, F. Leermakers, G. Portale, and M. A. C. Stuart. The influence of charge ratio on transient networks of polyelectrolyte complex micelles. *Soft Matter*, 8:104–117, 2012.

[110] D. V. Krogstad, N. A. Lynd, S.-H. Choi, J. M. Spruell, C. J. Hawker, E. J. Kramer, and M. V Tirrell. Effects of polymer and salt concentration on the structure and properties of triblock copolymer coacervate hydrogels. *Macromolecules*, 46:1512–1518, 2013.

[111] D. J. Audus, J. D. Gopez, D. V. Krogstad, N. A. Lynd, E. J. Kramer, C. J. Hawker, and G. H. Fredrickson. Phase behavior of electrostatically complexed polyelectrolyte gels using an embedded fluctuation model. *Soft Matter*, 11(6):1214–1225, 2015.

[112] S. Srivastava, M. Andreev, A. E. Levi, D. J. Goldfeld, J. Mao, W. T. Heller, V. M. Prabhu, J. J. de Pablo, and M. V. Tirrell. Gel phase formation in dilute triblock copolyelectrolyte complexes. *Nature Commun.*, 8:14131, 2017.

[113] C. M. Papadakis and C. Tsitsilianis. Responsive hydrogels from associative block copolymers: Physical gelling through polyion complexation. *Gels*, 3:3, 2017.

[114] A. Rahalkar, G. Wei, R. Nieuwendaal, V. M.; Prabhu, S. Srivastava, A. E. Levi, J. J. de Pablo, and M. V. Tirrell. Effect of temperature on the structure and dynamics of triblock polyelectrolyte gels. *J. Chem. Phys.*, 149:163310, 2018.

[115] S. Srivastava, A. E. Levi, D. J. Goldfeld, and M. V. Tirrell. Structure, morphology, and rheology of polyelectrolyte complex hydrogels formed by self-assembly of oppositely charged triblock polyelectrolytes. *Macromolecules*, 53:5763-5774, 2020.

[116] Charles E Sing. Micro- to macro-phase separation transition in sequence-defined coacervates. *J. Chem. Phys.*, 152(2):024902, 2020.

[117] V. Yu. Borue and I. Ya. Erukhimovich. A statistical theory of globular polyelectrolyte complexes. *Macromolecules*, 23(15):3625–3632, 1990.

[118] Martin Castelnovo and Jean-François Joanny. Formation of polyelectrolyte multilayers. *Langmuir*, 16(19):7524–7532, 2000.

[119] Alexander Kudlay and Monica Olvera de la Cruz. Precipitation of oppositely charged polyelectrolytes in salt solutions. *J. Chem. Phys.*, 120(1):404–412, 2004.

[120] Jian Qin and Juan J de Pablo. Criticality and connectivity in macromolecular charge complexation. *Macromolecules*, 49(22):8789–8800, 2016.

[121] J Wittmer, A Johner, and JF Joanny. Random and alternating polyampholytes. *EPL*, 24(4):263, 1993.

[122] Artem M Rumyantsev and Igor I Potemkin. Explicit description of complexation between oppositely charged polyelectrolytes as an advantage of the random phase approximation over the scaling approach. *Phys. Chem. Chem. Phys.*, 19(40):27580–27592, 2017.

[123] Kevin Shen and Zhen-Gang Wang. Electrostatic correlations and the polyelectrolyte self energy. *J. Chem. Phys.*, 146(8):084901, 2017.

[124] Michael Rubinstein, Qi Liao, and Sergey Panyukov. Structure of liquid coacervates formed by oppositely charged polyelectrolytes. *Macromolecules*, 51(23):9572–9588, 2018.

[125] A. M. Rumyantsev, E. Yu. Kramarenko, and O. V. Borisov. Microphase separation in complex coacervate due to incompatibility between polyanion and polycation. *Macromolecules*, 51(17):6587–6601, 2018.

[126] L Li, A M Rumyantsev, S Srivastava, S Meng, J J de Pablo, and M V Tirrell. Effect of solvent quality on the phase behavior of polyelectrolyte complexes. *Macromolecules*, 54(1):105–114, 2021.

[127] V. Y. Boryu and I. Y. Erukhimovich. A statistical theory of weakly charged polyelectrolytes: Fluctuations, equation of state and microphase separation. *Macromolecules*, 21(11):3240–3249, 1988.

[128] A. M. Rumyantsev, E. B. Zhulina, and O. V. Borisov. Complex coacervate of weakly charged polyelectrolytes: Diagram of states. *Macromolecules*, 51(10):3788—3801, 2018.

[129] W. M. Brown, A. Kohlmeyer, S. J. Plimpton, and A. N. Tharrington. Implementing molecular dynamics on hybrid high performance computers - particle-particle particle-mesh. *Comp. Phys. Comm.*, 183:449–459, 2012.

[130] F. M. Lewis, C. Walling, W. Cummings, E. R. Briggs, and F. R. Mayo. Copolymerization. iv. effects of temperature and solvents on monomer reactivity ratios. *J. Am. Chem. Soc.*, 70:1519–1523, 1948.

[131] G. Bonta, B. M. Gallo, and S. Russo. Some kinetic aspects of radical copolymerization: Influence of the reaction medium on the reactivity ratios. *Polymer*, 16(6):429–432, 1975.

[132] S. Meng, Y. Liu, J. Yeo, J. M. Ting, and M. V. Tirrell. Effect of mixed solvents on polyelectrolyte complexes with salt. *Colloid Polym. Sci.*, 298:887–894, 2020.

[133] L. Li, S. Srivastava, M. Andreev, A. B. Marciel, J. J. de Pablo, and M. V. Tirrell. Phase behavior and salt partitioning in polyelectrolyte complex coacervates. *Macromolecules*, 51(8):2988–2995, 2018.

[134] K. Shen and Z.-G. Wang. Polyelectrolyte chain structure and solution phase behavior. *Macromolecules*, 51(5):1706–1717, 2018.

[135] J. Huang, F. J. Morin, and J. E. Laaser. Charge-density-dominated phase behavior and viscoelasticity of polyelectrolyte complex coacervates. *Macromolecules*, 52:4957–4967, 2019.

[136] A. M. Rumyantsev, A. A. Gavrilov, and E. Yu. Kramarenko. Electrostatically stabilized microphase separation in blends of oppositely charged polyelectrolytes. *Macromolecules*, 52(19):7167–7174, 2019.

[137] A. M. Rumyantsev and J. J. de Pablo. Microphase separation in polyelectrolyte blends: Weak segregation theory and relation to nuclear "pasta". *Macromolecules*, 53(4):1281–1292, 2020.

[138] A. V. Subbotin and A. N. Semenov. The structure of polyelectrolyte complex coacervates and multilayers. *Macromolecules*, 54(3):1314–1328, 2021.

[139] D. J. Grzetic, K. T. Delaney, and G. H. Fredrickson. Electrostatic manipulation of phase behavior in immiscible charged polymer blends. *Macromolecules*, 54(6):2604–2616, 2021.

[140] H. Angerman, G. ten Brinke, and I. Erukhimovich. Microphase separation in correlated random copolymers. *Macromolecules*, 29:3255–3262, 1996.

[141] P.-G. de Gennes. Theory of long-range correlations in polymer melts. *Faraday Discuss. Chem. Soc.*, 68:96–103, 1979.

[142] A. A. Gavrilov, Y. V. Kudryavtsev, P. G. Khalatur, and A. V. Chertovich. Microphase separation in regular and random copolymer melts by dpd simulations. *Chem. Phys. Lett.*, 503(4-6):277–282, 2011.

[143] H. M. Fares, Y. E.; Ghoussoub, J. D. Delgado, J. Fu, V. S. Urban, and J. B. Schlenoff. Scattering neutrons along the polyelectrolyte complex/coacervate continuum. *Macromolecules*, 51(13):4945—-4955, 2018.

[144] Amanda B Marciel, Samanvaya Srivastava, and Matthew V Tirrell. Structure and rheology of polyelectrolyte complex coacervates. *Soft Matter*, 14(13):2454–2464, 2018.

[145] JP Cotton, M Nierlich, F Boue, M Daoud, B Farnoux, G Jannink, R Duplessix, and C Picot. Experimental determination of the temperature–concentration diagram of flexible polymer solutions by neutron scattering. *J. Chem. Phys.*, 65(3):1101–1108, 1976.

[146] P.-G. de Gennes. *Scaling Concepts in Polymer Physics*. Cornell University, Ithaca, NY, 1979.

[147] A. Yu. Grosberg and A. R. Khokhlov. *Statistical Physics of Macromolecules*. AIP Press, NY, 1994.

[148] A. J. Ryan, C. W. Macosko, and W. Bras. Order-disorder transition in a block copolyurethane. *Macromolecules*, 25(23):6277–6283, 1992.

[149] M Teubner and R Strey. Origin of the scattering peak in microemulsions. *J. Chem. Phys.*, 87(5):3195–3200, 1987.

[150] B. W. Swift and M. Olvera de la Cruz. Random copolymers in concentrated solutions. *Eup. Phys. Lett.*, 35(7):487–492, 1996.

[151] Frank S Bates, Wayne W Maurer, Timothy P Lodge, M. F. Schulz, M. W. Matsen, Kristoffer Almdal, and Kell Mortensen. Isotropic lifshitz behavior in block copolymer-homopolymer blends. *Phys. Rev. Lett.*, 75(24):4429–4432, 1995.

[152] Frank S Bates, Wayne W Maurer, Paul M Lipic, Marc A Hillmyer, Kristoffer Almdal, Kell Mortensen, Glenn H Fredrickson, and Timothy P Lodge. Polymeric bicontinuous microemulsions. *Phys. Rev. Lett.*, 79(5):849–852, 1997.

[153] F. S. Bates, M. A. Hillmyer, T. P. Lodge, C. M. Bates, K. T. Delaney, and G. H. Fredrickson. Multiblock polymers: Panacea or pandora's box? *Science*, 336(6080):434–440, 2012.

[154] T. M. Birshtein and E. B. Zhulina. Scaling theory of supermolecular structures in block copolymer-solvent systems: 2. supercrystalline structures. *Polymer*, 31:1312–1320, 1990.

[155] M. Banaszak and M. D. Whitmore. Self-consistent theory of block copolymer blends: Selective solvent. *Macromolecules*, 25:3406–3412, 1992.

[156] C.-I. Huang and T. P. Lodge. Self-consistent calculations of block copolymer solution phase behavior. *Macromolecules*, 31:3556–3565, 1998.

[157] Anthony A Hyman, Christoph A Weber, and Frank Jülicher. Liquid-liquid phase separation in biology. *Annu. Rev. Cell Dev. Biol.*, 30(1):39–58, 2014.

[158] Simon Alberti, Amy Gladfelter, and Tanja Mittag. Considerations and challenges in studying liquid-liquid phase separation and biomolecular condensates. *Cell*, 176(3):419–434, 2019.

[159] Anisha Shakya, Seonyoung Park, Neha Rana, and John T King. Liquid-liquid phase separation of histone proteins in cells: Role in chromatin organization. *Biophys. J.*, 118(3):753–764, 2020.

[160] Erica A Frankel, Philip C Bevilacqua, and Christine D Keating. Polyamine/nucleotide coacervates provide strong compartmentalization of mg^{2+}, nucleotides, and RNA. *Langmuir*, 32(8):2041–2049, 2016.

[161] William M Aumiller, Jr, Bradley W Davis, and Christine D Keating. Phase separation as a possible means of nuclear compartmentalization. *Int. Rev. Cell Mol. Biol.*, 307:109–149, 2014.

[162] Björn Drobot, Juan M Iglesias-Artola, Kristian Le Vay, Viktoria Mayr, Mrityunjoy Kar, Moritz Kreysing, Hannes Mutschler, and T-Y Dora Tang. Compartmentalised RNA catalysis in membrane-free coacervate protocells. *Nat. Commun.*, 9(1):3643, 2018.

[163] William M Aumiller, Jr, Fatma Pir Cakmak, Bradley W Davis, and Christine D Keating. RNA-based coacervates as a model for membraneless organelles: Formation, properties, and interfacial liposome assembly. *Langmuir*, 32(39):10042–10053, 2016.

[164] N Amy Yewdall, Alain A M André, Tiemei Lu, and Evan Spruijt. Coacervates as models of membraneless organelles. *Curr. Opin. Colloid Interface Sci.*, 52(101416):101416, 2021.

[165] Carsten Donau, Fabian Späth, Marilyne Sosson, Brigitte A K Kriebisch, Fabian Schnitter, Marta Tena-Solsona, Hyun-Seo Kang, Elia Salibi, Michael Sattler, Hannes Mutschler, and Job Boekhoven. Active coacervate droplets as a model for membraneless organelles and protocells. *Nat. Commun.*, 11(1):5167, 2020.

[166] Vladimir N Uversky. Protein intrinsic disorder-based liquid-liquid phase transitions in biological systems: Complex coacervates and membrane-less organelles. *Adv. Colloid Interface Sci.*, 239:97–114, 2017.

[167] Tony Z Jia and Tommaso P Fraccia. Liquid crystal peptide/DNA coacervates in the context of prebiotic molecular evolution. *Crystals (Basel)*, 10(11):964, 2020.

[168] Alexander F Mason, Bastiaan C Buddingh', David S Williams, and Jan C M van Hest. Hierarchical self-assembly of a copolymer-stabilized coacervate protocell. *J. Am. Chem. Soc.*, 139(48):17309–17312, 2017.

[169] Shogo Koga, David S Williams, Adam W Perriman, and Stephen Mann. Peptide-nucleotide microdroplets as a step towards a membrane-free protocell model. *Nat. Chem.*, 3(9):720–724, 2011.

[170] Amanda B Marciel, Samanvaya Srivastava, and Matthew V Tirrell. Structure and rheology of polyelectrolyte complex coacervates. *Soft Matter*, 14(13):2454–2464, 2018.

[171] Alexander Kudlay, Alexander V Ermoshkin, and Monica Olvera de la Cruz. Complexation of oppositely charged polyelectrolytes: Effect of ion pair formation. *Macromolecules*, 37(24):9231–9241, 2004.

[172] Zhaoyang Ou and M Muthukumar. Entropy and enthalpy of polyelectrolyte complexation: Langevin dynamics simulations. *J. Chem. Phys.*, 124(15):154902, 2006.

[173] Jonghoon Lee, Yuri O Popov, and Glenn H Fredrickson. Complex coacervation: a field theoretic simulation study of polyelectrolyte complexation. *J. Chem. Phys.*, 128(22):224908, 2008.

[174] Ali Salehi and Ronald G Larson. A molecular thermodynamic model of complexation in mixtures of oppositely charged polyelectrolytes with explicit account of charge association/dissociation. *Macromolecules*, 49(24):9706–9719, 2016.

[175] Kevin Shen and Zhen-Gang Wang. Polyelectrolyte chain structure and solution phase behavior. *Macromolecules*, 51(5):1706–1717, 2018.

[176] Sabin Adhikari, Michael A Leaf, and Murugappan Muthukumar. Polyelectrolyte complex coacervation by electrostatic dipolar interactions. *J. Chem. Phys.*, 149(16):163308, 2018.

[177] Yalin Liu, Cristiam F Santa Chalarca, R Nicholas Carmean, Rebecca A Olson, Jason Madinya, Brent S Sumerlin, Charles E Sing, Todd Emrick, and Sarah L Perry. Effect

of polymer chemistry on the linear viscoelasticity of complex coacervates. *Macromolecules*, 53(18):7851–7864, 2020.

[178] Christian Aponte-Rivera and Michael Rubinstein. Dynamic coupling in unentangled liquid coacervates formed by oppositely charged polyelectrolytes. *Macromolecules*, 54(4):1783–1800, 2021.

[179] Artem M Rumyantsev, Elena Yu Kramarenko, and Oleg V Borisov. Microphase separation in complex coacervate due to incompatibility between polyanion and polycation. *Macromolecules*, 51(17):6587–6601, 2018.

[180] Artem M Rumyantsev, Alexey A Gavrilov, and Elena Yu Kramarenko. Electrostatically stabilized microphase separation in blends of oppositely charged polyelectrolytes. *Macromolecules*, 52(19):7167–7174, 2019.

[181] A N Semenov and Alexei R Khokhlov. Statistical physics of liquid-crystalline polymers. *Sov. phys. Uspekhi*, 31(11):988–1014, 1988.

[182] Zheng Yu Chen. Nematic ordering in semiflexible polymer chains. *Macromolecules*, 26(13):3419–3423, 1993.

[183] M Dijkstra and D Frenkel. Simulation study of the isotropic-to-nematic transitions of semiflexible polymers. *Phys. Rev. E Stat. Phys. Plasmas Fluids Relat. Interdiscip. Topics*, 51(6):5891–5898, 1995.

[184] Fernando A Escobedo and Juan J de Pablo. Monte carlo simulation of athermal mesogenic chains: Pure systems, mixtures, and constrained environments. *J. Chem. Phys.*, 106(23):9858–9868, 1997.

[185] H Weber, W Paul, and K Binder. Monte carlo simulation of a lyotropic first-order isotropic-nematic phase transition in a lattice polymer model. *Phys. Rev. E Stat. Phys. Plasmas Fluids Relat. Interdiscip. Topics*, 59(2):2168–2174, 1999.

[186] Sergei A Egorov, Andrey Milchev, Peter Virnau, and Kurt Binder. A new insight into the isotropic–nematic phase transition in lyotropic solutions of semiflexible polymers: density-functional theory tested by molecular dynamics. *Soft Matter*, 12(22):4944–4959, 2016.

[187] Andrey Milchev, Arash Nikoubashman, and Kurt Binder. The smectic phase in semiflexible polymer materials: A large scale molecular dynamics study. *Comput. Mater. Sci.*, 166:230–239, 2019.

[188] Anisha Shakya and John T King. DNA local-flexibility-dependent assembly of phase-separated liquid droplets. *Biophys. J.*, 115(10):1840–1847, 2018.

[189] Michael Lueckheide, Jeffrey R Vieregg, Alex J Bologna, Lorraine Leon, and Matthew V Tirrell. Structure-property relationships of oligonucleotide polyelectrolyte complex micelles. *Nano Lett.*, 18(11):7111–7117, 2018.

[190] Tommaso P Fraccia, Gregory P Smith, Giuliano Zanchetta, Elvezia Paraboschi, Youngwoo Yi, David M Walba, Giorgio Dieci, Noel A Clark, and Tommaso Bellini. Abiotic ligation of DNA oligomers templated by their liquid crystal ordering. *Nat. Commun.*, 6(1):6424, 2015.

[191] Tommaso P Fraccia, Giuliano Zanchetta, Valeria Rimoldi, Noel A Clark, and Tommaso Bellini. Evidence of liquid crystal-assisted abiotic ligation of nucleic acids. *Orig. Life Evol. Biosph.*, 45(1-2):51–68, 2015.

[192] Marco Todisco, Tommaso P Fraccia, Greg P Smith, Andrea Corno, Lucas Bethge, Sven Klussmann, Elvezia M Paraboschi, Rosanna Asselta, Diego Colombo, Giuliano Zanchetta, Noel A Clark, and Tommaso Bellini. Nonenzymatic polymerization into long linear RNA templated by liquid crystal self-assembly. *ACS Nano*, 12(10):9750–9762, 2018.

[193] Rajeev Kumar, Debra Audus, and Glenn H Fredrickson. Phase separation in symmetric mixtures of oppositely charged rodlike polyelectrolytes. *J. Phys. Chem. B*, 114(31):9956–9976, 2010.

[194] Artem M Rumyantsev and Juan J de Pablo. Liquid crystalline and isotropic coacervates of semiflexible polyanions and flexible polycations. *Macromolecules*, 52(14):5140–5156, 2019.

[195] Anisha Shakya, Martin Girard, John T King, and Monica Olvera de la Cruz. Role of chain flexibility in asymmetric polyelectrolyte complexation in salt solutions. *Macromolecules*, 53(4):1258–1269, 2020.

[196] Leszek A Utracki. Compatibilization of polymer blends. *Can. J. Chem. Eng.*, 80(6):1008–1016, 2002.

[197] Narayan P Adhikari and Ekkehard Straube. Interfacial properties of asymmetric polymer mixtures. *Macromol. Theory Simul.*, 12(7):499–507, 2003.

[198] Jian Qin, Dimitrios Priftis, Robert Farina, Sarah L Perry, Lorraine Leon, Jonathan Whitmer, Kyle Hoffmann, Matthew Tirrell, and Juan J de Pablo. Interfacial tension of polyelectrolyte complex coacervate phases. *ACS Macro Lett.*, 3(6):565–568, 2014.

[199] Tyler K Lytle, Anthony J Salazar, and Charles E Sing. Interfacial properties of polymeric complex coacervates from simulation and theory. *J. Chem. Phys.*, 149(16):163315, 2018.

[200] Debra J Audus, Samim Ali, Artem M Rumyantsev, Yuanchi Ma, Juan J de Pablo, and Vivek M Prabhu. Molecular mass dependence of interfacial tension in complex coacervation. *Phys. Rev. Lett.*, 126(23):237801, 2021.

[201] Vivek M Prabhu. Interfacial tension in polyelectrolyte systems exhibiting associative liquid–liquid phase separation. *Curr. Opin. Colloid Interface Sci.*, 53(101422):101422, 2021.

[202] Jean-Pierre Hansen and Ian R McDonald. Applications to soft matter. In *Theory of Simple Liquids*, pages 511–584. Elsevier, 2013.

[203] Ralf Everaers, Sathish K Sukumaran, Gary S Grest, Carsten Svaneborg, Arvind Sivasubramanian, and Kurt Kremer. Rheology and microscopic topology of entangled polymeric liquids. *Science*, 303(5659):823–826, 2004.

[204] Jan-Michael Y Carrillo, Fred C MacKintosh, and Andrey V Dobrynin. Nonlinear elasticity: From single chain to networks and gels. *Macromolecules*, 46(9):3679–3692, 2013.

[205] V A Ivanov, M R Stukan, M Müller, W Paul, and K Binder. Phase diagram of solutions of stiff-chain macromolecules: A monte carlo simulation. *J. Chem. Phys.*, 118(22):10333–10342, 2003.

[206] Sergei A Egorov, Andrey Milchev, and Kurt Binder. Anomalous fluctuations of nematic order in solutions of semiflexible polymers. *Phys. Rev. Lett.*, 116(18), 2016.

[207] A R Khokhlov and A N Semenov. Liquid-crystalline ordering in the solution of long persistent chains. *Physica A*, 108(2-3):546–556, 1981.

[208] A R Khokhlov and A N Semenov. Liquid-crystalline ordering in the solution of partially flexible macromolecules. *Physica A*, 112(3):605–614, 1982.

[209] A R Khokhlov and A N Semenov. On the theory of liquid-crystalline ordering of polymer chains with limited flexibility. *J. Stat. Phys.*, 38(1-2):161–182, 1985.

[210] A R Khokhlov and A N Semenov. Theory of nematic ordering in the melts of macromolecules with different flexibility mechanisms. *Macromolecules*, 19(2):373–378, 1986.

[211] Arun Yethiraj and Herb Fynewever. Isotropic to nematic transition in semiflexible polymer melts. *Mol. Phys.*, 93(5):693–701, 1998.

[212] Russell K W Spencer and Mark W Matsen. Surface segregation in athermal polymer blends due to conformational asymmetry. *Macromolecules*, 54(21):10100–10109, 2021.

[213] Lars Onsager. The effects of shape on the interaction of colloidal particles. *Ann. N. Y. Acad. Sci.*, 51(4):627–659, 1949.

[214] For simplicity, we provide the values of $\phi l/d$ and $\phi l/d$ corresponding to the spinodal positions. the positions of the binodals are known to be sufficiently close. for instance, the boundaries of the 2-phase region in onsager model are $\phi_i l/d = 3.34$ and $\phi_a l/d = 4.49$.

[215] J D Parsons. Nematic ordering in a system of rods. *Phys. Rev. A Gen. Phys.*, 19(3):1225–1230, 1979.

[216] Jian Qin and Juan J de Pablo. Criticality and connectivity in macromolecular charge complexation. *Macromolecules*, 49(22):8789–8800, 2016.

[217] Zheng Yu Chen. Nematic ordering in semiflexible polymer chains. *Macromolecules*, 26(13):3419–3423, 1993.

[218] M Dijkstra and D Frenkel. Simulation study of the isotropic-to-nematic transitions of semiflexible polymers. *Phys. Rev. E Stat. Phys. Plasmas Fluids Relat. Interdiscip. Topics*, 51(6):5891–5898, 1995.

[219] Igor I Potemkin, Roman E Limberger, Alexander N Kudlay, and Alexei R Khokhlov. Rodlike polyelectrolyte solutions: effect of the many-body coulomb attraction of similarly charged molecules favoring weak nematic ordering at very small polymer concentration. *Phys. Rev. E Stat. Nonlin. Soft Matter Phys.*, 66(1 Pt 1):011802, 2002.

[220] Dian Yang, Sergey V Venev, Vladimir V Palyulin, and Igor I Potemkin. Nematic ordering of rigid rod polyelectrolytes induced by electrostatic interactions: effect of discrete charge distribution along the chain. *J. Chem. Phys.*, 134(7):074901, 2011.

[221] Theo Odijk. Polyelectrolytes near the rod limit. *J. Polym. Sci. Polym. Phys. Ed.*, 15(3):477–483, 1977.

[222] Jeffrey Skolnick and Marshall Fixman. Electrostatic persistence length of a wormlike polyelectrolyte. *Macromolecules*, 10(5):944–948, 1977.

[223] J-L Barrat and J-F Joanny. Persistence length of polyelectrolyte chains. *EPL*, 24(5):333–338, 1993.

[224] B-Y Ha and D Thirumalai. Electrostatic persistence length of a polyelectrolyte chain. *Macromolecules*, 28(2):577–581, 1995.

[225] Andrey V Dobrynin. Electrostatic persistence length of semiflexible and flexible polyelectrolytes. *Macromolecules*, 38(22):9304–9314, 2005.

[226] A. M. Rumyantsev, A. Johner, M. V. Tirrell, and J. J. de Pablo. Unifying weak and strong charge correlations within the random phase approximation: Polyampholytes of various sequences. *Macromolecules*, 55(14):6260–6274, 2022.

[227] N V Brilliantov. Accurate first-principle equation of state for the one-component plasma. *Contrib. plasma phys.*, 38(4):489–499, 1998.

[228] Mikhail K Glagolev, Valentina V Vasilevskaya, and Alexei R Khokhlov. Induced liquid-crystalline ordering in solutions of stiff and flexible amphiphilic macromolecules: Effect of mixture composition. *J. Chem. Phys.*, 145(4):044904, 2016.

[229] Andrea J Liu and Glenn H Fredrickson. Free energy functionals for semiflexible polymer solutions and blends. *Macromolecules*, 26(11):2817–2824, 1993.

[230] Jeffrey D Weinhold, Sanat K Kumar, Chandralekha Singh, and Kenneth S Schweizer. Athermal stiffness blends: A comparison of monte carlo simulations and integral equation theory. *J. Chem. Phys.*, 103(21):9460–9474, 1995.

[231] Andreas Gauger and Tadeusz Pakula. Phase equilibrium in mixtures of flexible and stiff polymers studied by monte carlo simulation. *J. Chem. Phys.*, 98(4):3548–3553, 1993.

[232] M Mueller. Effects of structural disparities in polymer blends: A Monte-Carlo investigation. *Macromolecules*, 28(19):6556–6564, 1995.

[233] Narayan P Adhikari and Ekkehard Straube. Phase separation in mixtures of flexible and semiflexible polymers. *Polym. J.*, 43(9):751–756, 2011.

[234] Abelardo Ramírez-Hernández, Su-Mi Hur, Julio C Armas-Pérez, Monica Olvera de la Cruz, and Juan J De Pablo. Demixing by a nematic mean field: Coarse-grained simulations of liquid crystalline polymers. *Polymers (Basel)*, 9(3):88, 2017.

[235] Andrey Milchev, Sergei A Egorov, Jiarul Midya, Kurt Binder, and Arash Nikoubashman. Entropic unmixing in nematic blends of semiflexible polymers. *ACS Macro Lett.*, 9(12):1779–1784, 2020.

[236] Sergei A Egorov, Andrey Milchev, Arash Nikoubashman, and Kurt Binder. Phase separation and nematic order in lyotropic solutions: Two types of polymers with different stiffnesses in a common solvent. *J. Phys. Chem. B*, 125(3):956–969, 2021.

[237] Douglas J Grzetic, Kris T Delaney, and Glenn H Fredrickson. Electrostatic manipulation of phase behavior in immiscible charged polymer blends. *Macromolecules*, 54(6):2604–2616, 2021.

[238] Andrey V Subbotin and Alexander N Semenov. The structure of polyelectrolyte complex coacervates and multilayers. *Macromolecules*, 54(3):1314–1328, 2021.

[239] J Fukuda. Free energy of semiflexible polymers and structure of interfaces. *Eur. Phys. J. B*, 7(4):573–583, 1999.

[240] P Bolhuis and D Frenkel. Tracing the phase boundaries of hard spherocylinders. *J. Che. Phys.*, 106(2):666–687, 1997.

[241] Kris T Delaney and Glenn H Fredrickson. Theory of polyelectrolyte complexation—complex coacervates are self-coacervates. *The Journal of chemical physics*, 146(22):224902, 2017.

[242] Pengfei Zhang and Zhen-Gang Wang. Interfacial structure and tension of polyelectrolyte complex coacervates. *Macromolecules*, 54(23):10994–11007, 2021.

[243] Yisheng Xu, Miaomiao Liu, Mostufa Faisal, Yi Si, and Yanchuan Guo. Selective protein complexation and coacervation by polyelectrolytes. *Advances in Colloid and Interface Science*, 239:158–167, 2017.

[244] Yisheng Xu, Malek Mazzawi, Kaimin Chen, Lianhong Sun, and Paul L Dubin. Protein purification by polyelectrolyte coacervation: influence of protein charge anisotropy on selectivity. *Biomacromolecules*, 12(5):1512–1522, 2011.

[245] Whitney C Blocher McTigue and Sarah L Perry. Design rules for encapsulating proteins into complex coacervates. *Soft Matter*, 15(15):3089–3103, 2019.

[246] Mintai P Hwang, Ronald J Fecek, Tianyue Qin, Walter J Storkus, and Yadong Wang. Single injection of il-12 coacervate as an effective therapy against b16-f10 melanoma in mice. *Journal of Controlled Release*, 318:270–278, 2020.

[247] Eun Young Jeon, Da-som Choi, Seunghyun Choi, Ju-young Won, Yunju Jo, Hye-bin Kim, Youngmee Jung, Sang Chul Shin, Hophil Min, Hae Woong Choi, et al. Enhancing adoptive t-cell therapy with fucoidan-based il-2 delivery microcapsules. *Bioengineering & Translational Medicine*, page e10362, 2022.

[248] Sylvie L Turgeon and Sandra I Laneuville. Protein+ polysaccharide coacervates and complexes: from scientific background to their application as functional ingredients in food products. In *Modern biopolymer science*, pages 327–363. Elsevier, 2009.

[249] Xiao Jun-xia, Yu Hai-yan, and Yang Jian. Microencapsulation of sweet orange oil by complex coacervation with soybean protein isolate/gum arabic. *Food chemistry*, 125(4):1267–1272, 2011.

[250] Nirmala Devi, Mandip Sarmah, Bably Khatun, and Tarun K Maji. Encapsulation of active ingredients in polysaccharide–protein complex coacervates. *Advances in colloid and interface science*, 239:136–145, 2017.

[251] Whitney C Blocher McTigue and Sarah L Perry. Protein encapsulation using complex coacervates: what nature has to teach us. *Small*, 16(27):1907671, 2020.

[252] Fatih Comert, Alexander J Malanowski, Fatemeh Azarikia, and Paul L Dubin. Coacervation and precipitation in polysaccharide–protein systems. *Soft Matter*, 12(18):4154–4161, 2016.

[253] Fatih Comert and Paul L Dubin. Liquid-liquid and liquid-solid phase separation in protein-polyelectrolyte systems. *Advances in Colloid and Interface Science*, 239:213–217, 2017.

[254] Yunfeng Yan, Ebru Kizilay, Daniel Seeman, Sean Flanagan, Paul L Dubin, Lionel Bovetto, Laurence Donato, and Christophe Schmitt. Heteroprotein complex coacervation: Bovine β-lactoglobulin and lactoferrin. *Langmuir*, 29(50):15614–15623, 2013.

[255] AB Kayitmazer, AF Koksal, and E Kilic Iyilik. Complex coacervation of hyaluronic acid and chitosan: effects of ph, ionic strength, charge density, chain length and the charge ratio. *Soft Matter*, 11(44):8605–8612, 2015.

[256] Shang Gao, Advait Holkar, and Samanvaya Srivastava. Protein–polyelectrolyte complexes and micellar assemblies. *Polymers*, 11(7):1097, 2019.

[257] Sieun Kim, Hursh V Sureka, A Basak Kayitmazer, Gang Wang, James W Swan, and Bradley D Olsen. Effect of protein surface charge distribution on protein–polyelectrolyte complexation. *Biomacromolecules*, 21(8):3026–3037, 2020.

[258] Ebru Kizilay, A Basak Kayitmazer, and Paul L Dubin. Complexation and coacervation of polyelectrolytes with oppositely charged colloids. *Advances in colloid and interface science*, 167(1-2):24–37, 2011.

[259] Justin M Horn, Rachel A Kapelner, and Allie C Obermeyer. Macro-and microphase separated protein-polyelectrolyte complexes: Design parameters and current progress. *Polymers*, 11(4):578, 2019.

[260] Rachel A Kapelner, Vivian Yeong, and Allie C Obermeyer. Molecular determinants of protein-based coacervates. *Current Opinion in Colloid & Interface Science*, 52:101407, 2021.

[261] Chad S Cummings and Allie C Obermeyer. Phase separation behavior of supercharged proteins and polyelectrolytes. *Biochemistry*, 57(3):314–323, 2018.

[262] Vivian Yeong, Emily G Werth, Lewis M Brown, and Allie C Obermeyer. Formation of biomolecular condensates in bacteria by tuning protein electrostatics. *ACS central science*, 6(12):2301–2310, 2020.

[263] Jie Xiao, Yunqi Li, and Qingrong Huang. Application of monte carlo simulation in addressing key issues of complex coacervation formed by polyelectrolytes and oppositely charged colloids. *Advances in colloid and interface science*, 239:31–45, 2017.

[264] Rituparna Samanta and Venkat Ganesan. Influence of protein charge patches on the structure of protein–polyelectrolyte complexes. *Soft Matter*, 14(46):9475–9488, 2018.

[265] Rituparna Samanta, Avni Halabe, and Venkat Ganesan. Influence of charge regulation and charge heterogeneity on complexation between polyelectrolytes and proteins. *The Journal of Physical Chemistry B*, 124(22):4421–4435, 2020.

[266] Rituparna Samanta and Venkat Ganesan. Direct simulations of phase behavior of mixtures of oppositely charged proteins/nanoparticles and polyelectrolytes. *The Journal of Physical Chemistry B*, 124(48):10943–10951, 2020.

[267] Jason J Madinya and Charles E Sing. Hybrid field theory and particle simulation model of polyelectrolyte–surfactant coacervation. *Macromolecules*, 55(6):2358–2373, 2022.

[268] Marat Andreev, Vivek M Prabhu, Jack F Douglas, Matthew Tirrell, and Juan J de Pablo. Complex coacervation in polyelectrolytes from a coarse-grained model. *ACS Macro Lett.*, 51(17):6717–6723, 2018.

[269] Sai Vineeth Bobbili and Scott T Milner. A simple simulation model for complex coacervates. *Soft Matter*, 17(40):9181–9188, 2021.

[270] Heyi Liang and Juan J de Pablo. A coarse-grained molecular dynamics study of strongly charged polyelectrolyte coacervates: Interfacial, structural, and dynamical properties. *Macromolecules*, 2022.

[271] Chaofu Wu. Bulk modulus of poly (ethylene oxide) simulated using the systematically coarse-grained model. *Computational Materials Science*, 156:89–95, 2019.

[272] Michael Rubinstein, Ralph H Colby, et al. *Polymer physics*, volume 23. Oxford university press New York, 2003.

[273] Li-Heng Cai, Sergey Panyukov, and Michael Rubinstein. Mobility of nonsticky nanoparticles in polymer liquids. *Macromolecules*, 44(19):7853–7863, 2011.

[274] Umi Yamamoto, Jan-Michael Y Carrillo, Vera Bocharova, Alexei P Sokolov, Bobby G Sumpter, and Kenneth S Schweizer. Theory and simulation of attractive nanoparticle transport in polymer melts. *Macromolecules*, 51(6):2258–2267, 2018.

[275] Vagner Seibert. Distributing points on a sphere, Jun 2020.

[276] Michael A Webb, Nicholas E Jackson, Phwey S Gil, and Juan J de Pablo. Targeted sequence design within the coarse-grained polymer genome. *Science advances*, 6(43):eabc6216, 2020.

[277] Debjyoti Bhattacharya, Devon C Kleeblatt, Antonia Statt, and Wesley F Reinhart. Predicting aggregate morphology of sequence-defined macromolecules with recurrent neural networks. *Soft matter*, 18(27):5037–5051, 2022.

[278] Robert J Hickey, Timothy M Gillard, Matthew T Irwin, Timothy P Lodge, and Frank S Bates. Structure, viscoelasticity, and interfacial dynamics of a model polymeric bicontinuous microemulsion. *Soft Matter*, 12(1):53–66, 2016.

[279] Jean-François Lutz, Makoto Ouchi, David R Liu, and Mitsuo Sawamoto. Sequence-controlled polymers. *Science*, 341(6146), 2013.

[280] E. I. Shakhnovich and A. M. Gutin. Formation of microdomains in a quenched disordered heteropolymer. *J. Phys. (Paris)*, 50(14):1843–1850, 1989.

[281] For ab random copolymer melts, the mean-field theory of ref. 105 predicts the existence of a narrow χ_{AB} window between homogeneous melt and disordered microphase where the formation of two coexisting macroscopic phases takes place if $\lambda > \lambda_L = -0.286$. however, this two-phase region usually does not survive because of the strong fluctuations, as shown using ginzburg criterion [107] and simulations [107, 108].

[282] Artem M Rumyantsev, Nicholas E Jackson, and Juan J de Pablo. Polyelectrolyte complex coacervates: Recent developments and new frontiers. *Annu. Rev. Condens. Matter Phys.*, 12(1):155–176, 2021.

[283] Yelena R Sliozberg and Jan W Andzelm. Fast protocol for equilibration of entangled and branched polymer chains. *Chem. Phys. Lett.*, 523:139–143, 2012.

[284] J-L Barrat and J-F Joanny. Persistence length of polyelectrolyte chains. *EPL*, 24(5):333–338, 1993.

[285] J Fukuda. Free energy of semiflexible polymers and structure of interfaces. *Eur. Phys. J. B*, 7(4):573–583, 1999.

[286] Jiarul Midya, Sergei A Egorov, Kurt Binder, and Arash Nikoubashman. Phase behavior of flexible and semiflexible polymers in solvents of varying quality. *J. Chem. Phys.*, 151(3):034902, 2019.

[287] Boris Y Drovetsky, Andrea J Liu, and C H Mak. Nematic-isotropic interfaces in semiflexible polymer blends. *J. Chem. Phys.*, 111(9):4334–4342, 1999.

[288] Diddo Diddens, Jörg Baschnagel, and Albert Johner. Microscopic structure of compacted polyelectrolyte complexes: Insights from molecular dynamics simulations. *ACS Macro Lett.*, 8(2):123–127, 2019.